UAB

Universitat Autònoma de Barcelona

High-density cortical implant for brain-machine interfaces based on two-dimensional materials

Nathan Schaefer

submitted this thesis in
partial fulfillment for a degree as

Doctor of Philosophy in Electrical and Telecommunication Engineering

of the

Universitat Autònoma de Barcelona

Supervisor: Prof. José A. Garrido Ariza
Co-Supervisor: Dr. Anton Guimerà-Brunet
Thesis Tutor: Prof. David Jiménez Jiménez

Catalan Institute of Nanoscience and Nanotechnology
Barcelona, Spain, December 2020

Acknowledgements

Abstract

The experimental discovery of graphene in 2004 marked the advent of a new research field based on two-dimensional materials, investigating their properties for applications in electronics, photonics and optoelectronics and, recently, also biomedical technology. Neurotechnology in particular is a subject which could strongly benefit from these new materials, as their mechanical and chemical nature allow them to form a stable, conformable interface with the brain. The graphene solution-gated field-effect transistor (gSGFET) is one of several emerging sensing devices utilizing thin materials, and has shown great potential for brain-machine interfaces (BMIs), as it is able to record neural activity with high accuracy. Historically, electrodes have been favored for such application, as they are easy to fabricate and the recorded signals can be acquired using simple read-out techniques. In recent years, however, the use of sensors with a transistor design was found to be beneficial for specific applications as they also unveil slow oscillatory activity, which is yet mostly unexplored. Moreover, transistors allow to construct sensor arrays with a large number of recording sites since, contrary to electrodes, they do not need to be combined with additional electronic components to enable sophisticated addressing schemes, thus strongly easing the technological complexity of fabricating these arrays. This PhD thesis explores strategies to further improve the gSGFET's sensing capabilities and to integrating many sensors into high density neural probes, capable to provide a detailed mapping of the brain.

After giving a brief outlook on the structure and content of the thesis in chapter 1, chapter 2 offers a general introduction to BMIs and to the two-dimensional materials used to develop the technology presented here. High intrinsic sensor noise remains a critical issue in electrophysiology due to the small amplitude of neural signals on the surface of the cortex. The two-dimensional nature of graphene and other 2D materials exposes them to degrading influences from their surroundings and makes it challenging to create high-quality interfaces with such materials. This leads to, for example, augmented low-frequency noise in the gSGFET which contaminates the frequency band of interest for neural recordings. Thus, as a first step towards the development of a high quality neural sensor array, technological improvements which allow to lower such intrinsic device noise are explored in chapter 3. Next, the fabrication and characterization of high-density neural sensor arrays of above 1000 gSGFET sensors on flexible substrate is described. The rapidly increasing size of the connector footprint with the number of sensors poses restrictions on the count and the density of recording sites achievable on the array; thus, the compatibility of the gSGFET technology with multiplexed readout schemes is of critical importance.

Multiplexing strategies allow the combination of multiples streams of information into a single signal and would thereby help to overcome bandwidth limitations of the state-of-the-art BMIs. More concretely, the compatibility of the gSGFET technology with the two most common schemes of multiplexed data readout, namely frequency-division and time-division multiplexing, is presented in chapter 4. Ultimately, a monolithic integration of addressing circuitry into the flexible sensor array is explored in chapter 5, as this would prevent inter-site crosstalk which can severely degrade the fidelity of the recorded signal in large multiplexed sensor arrays. Two-dimension transition-metal-dichalcogenides (e.g. MoS_2) are suggested for this purpose, as they combine mechanical flexibility with the bandgap necessary for designing field-effect transistors with high on/off-ratios.

Chapter 6 summarizes the results of this thesis, which shows that two-dimensional materials are compelling candidates to build neural interfaces due to the combination of electrical and mechanical properties. A hybrid gSGFET/MoS_2-FET sensor array with multiplexed readout functionality is showcased as a first prototype towards a new generation of BMIs and a roadmap for the technology's scale-up is presented. The technology developed in the frame of this PhD offers a promising alternative to state-of-the-art BMIs, paring high sensitivity to broadband neural activity with mechanical flexibility as well as high scalability and proves suitable to provide novel insights into how the brain works.

Contents

Contents

List of Figures

List of Figures

Chapter 1

Motivation and thesis outline

1.1 Motivation

In recent years, two-dimensional materials have seen a surge in research interest due to their rich varity of mechanical, chemical, electrical and optical properties [1, 2, 3, 4]. This combination of characteristics make them suited for many different potential applications, such as flexible electronics in a post-silicon era [5, 6], highly efficient photodetectors [7] and wearable devices [8]. A relatively young yet very promising research field that is increasingly drawing attention is the use of two-dimensional materials for bioelectronic applications [9, 10, 11]. The challenge here lies in creating interfaces between electronic devices, which are naturally rigid in structure and communicate through electrical signals, and soft corrugated biologic tissue relying on ions, molecules and biomolecules to transport information. Bioelectronic applications range from electrocardiography to glucose and pH sensors. However, arguably the most complex and exciting one would be to create an interface between electronic devices and the brain. Understanding of the human brain is commonly considered one of the biggest remaining scientific challenges of our time; as a consequence we are witnessing an intensified research into the development of flexible brain-machine-interfaces (BMIs), which would allow us to both read and stimulate brain activity. The graphene solution-gated field effect transistor (gSGFET) is one of many emerging new neural technologies. It has shown great potential for conformable BMIs as it is able to record brain activity with high accuracy due to graphene's crucial properties which provide mechanical flexibility, biocompatibility and high sensitivity. Yet, so far the gSGFET technology has only been employed in relatively small sensor arrays, which limit the size of the neuron populations the array can interface with. As ultimately efficient BMIs will be required to simultaenously interface with much larger populations across various brain regions, while ideally maintaining local resolution down to a single neuron level, the upscaling of the graphene technology towards large-scale, high-density arrays will become paramount for its success in the field. The current state-of-the-art of flexible BMIs still struggles to provide such high sensor density and sensor numbers, due to the challenge of the connector footprint rapidly increasing with array size, which makes an employment of multiplexed readout circuitry mandatory [12]. Another

issue is a relative scarcity of materials which match strict requirements of flexibility, biocompatibility and durability. In this thesis, we explore the suitability of two-dimensional materials to overcome those challenges. To this end, high-density gSGFET sensor arrays are fabricated and their compatibility with multiplexed readout methodologies is assessed. Multiplexing typically requires an addressing strategy to sequentially record from different columns or rows on the array. Usually, semiconductors with large on/off-ratios are used to either open or close the respective lines on the array. While graphene presents great properties to transduce brain activity, it lacks a band-gap and thus cannot provide this functionality. Here, a monolithic combination with field-effect transistors based on two-dimensional transition metal dichalcogenides (TMDCs) such as MoS_2, which have a wide direct band-gap and thus provide high on/off-ratios [13], would enable addressable yet flexible sensor arrays. The main objective of the technology developed throughout this thesis and within the overarching European research project 'BrainCom' is to gain a better understanding of the neural mechanisms which give rise to the comprehension and expression of speech and to apply this knowledge to develop novel neuroprosthetics to treat patients with aphasia.

1.2   Publications and patents

This thesis is based on the following **primary publications**:

- **N. Schaefer**, R. Garcia-Cortadella, A. Bonaccini Calia, N. Mavredakis, X. Illa, E. Masvidal-Codina, J. de la Cruz, E. del Corro, L. Rodríguez, E. Prats-Alfonso, J. Bousquet, J. Martínez-Aguilar, A. P. Pérez-Marín, C. Hébert, R. Villa, D. Jiménez, A. Guimerà-Brunet and J. A. Garrido, 'Improved metal-graphene contacts for low-noise, high-density microtransistor arrays for neural sensing', *Carbon*, 2020, 161, 647–655.
  https://doi.org/10.1016/j.carbon.2020.01.066

- **N. Schaefer**, R. Garcia-Cortadella, J. Martínez-Aguilar, G. Schwesig, X. Illa, A. Moya Lara, S. Santiago, C. Hébert, G. Guirado, R. Villa, A. Sirota, A. Guimerà-Brunet and J. A. Garrido, 'Multiplexed Neural Sensor Array of Graphene Solution-Gated Field-Effect Transistors', *2D Materials*, 2020, 7(2).
  https://doi.org/10.1088/2053-1583/ab7976

Additionally, the obtained results have contributed to these **complementary publications**:

- R. Garcia-Cortadella, **N. Schäfer**, J. Cisneros, L. Ré, X. Illa, G. Schwesig, A. Moya, S. Santiago, G. Guirado, R. Villa, A. Sirota, F. Serra-Graells, J. A.

Garrido and A. Guimerà-Brunet, 'Switchless Multiplexing of Graphene Active Sensor Arrays for Brain Mapping', *Nano Letters*, 2020, 20(5), 3528–3537. https://doi.org/10.1021/acs.nanolett.0c00467

- A. G. Polyravas, **N. Schaefer**, V. F. Curto, A. Bonaccini Calia , A. Guimera-Brunet, J. A. Garrido, G. G. Malliaras, 'Effect of channel thickness on noise in organic electrochemical transistors', *Applied Physics Letters*, 2020. https://doi.org/10.1063/5.0019693

- A. G. Polyravas, V. F. Curto, **N. Schaefer**, A. Bonaccini Calia, A. Guimera-Brunet, J. A Garrido and G G Malliaras, 'Impact of contact overlap on transconductance and noise in organic electrochemical transistors', *Flexible and Printed Electronics*, 2019, 4(4). https://doi.org/10.1088/2058-8585/ab4dc4

- R. Garcia-Cortadella, E. Masvidal-Codina, J. de la Cruz, **N. Schäfer**, G. Schwesig, C. Jeschke, J. Martinez-Aguilar, M. V. Sanchez-Vives, R. Villa, X. Illa, A. Sirota, A. Guimerà and J. A. Garrido1, 'Distortion-Free Sensing of Neural Activity Using Graphene Transistors', *Small*, 2020, 16(16). https://doi.org/10.1002/smll.201906640

- A. Bonaccini Calia, E. Masvidal-Codina, M. Smith, **N. Schäfer**, D. Rathore, E. Rodriguez, X. Illa, J. M. De la Cruz, E. Del Corro, E. Prats-Alfonso, J. Bousquet, C. Hébert, M. Drummond, A. Halder, S. Savage, J. Fornell Beringues, J. Sort, R. Villa, R. Wykes, A. Guimerà-Brunet, K. Kostarelos and J. A. Garrido, 'Graphene microtransistors on a flexible depth neural probe: A reliable tool for full-bandwidth recording in electrophysiology', *submitted*, 2020

- N. Mavredakis, R. Garcia Cortadella, X. Illa, **N. Schaefer**, A. Bonaccini Calia, A. Guimerà-Brunet, J. A. Garrido and David Jiménez, 'Bias Dependent Variability of Low-Frequency Noise in Single-Layer Graphene FETs', *Nanoscale Advances*, 2020, 2, 5450-5460, https://doi.org/10.1039/D0NA00632G

- N. Mavredakis , W. Wei, E. Pallecchi, D. Vignaud, H. Happy, R. Garcia Cortadella, **N. Schaefer**, A. Bonaccini Calia, J. A. Garrido, and D. Jimenez, 'Low-frequency noise parameter extraction method for single layer graphene FETs', *IEEE Transactions on Electron Devices*, 2020, vol. 67, no. 5, pp. 2093-2099, 2020, doi: 10.1109/TED.2020.2978215.

- A. Guimerà-Brunet, E. Masvidal-Codina, X. Illa, M. Dasilva, A. Bonaccini-Calia, E. Prats-Alfonso, J. Martínez-Aguilar, J. M. De la Cruz, R. Garcia-Cortadella, **N. Schaefer**, A. Barbero, P. Godignon, G. Rius, E. Del Corro, J. Bousquet, C. Hébert, R. Wykes, M. V. Sanchez-Vives, R. Villa and J. A. Garrido, 'Neural interfaces based on flexible graphene transistors: A new tool for electrophysiology', *IEEE International Electron Devices Meeting (IEDM)*, 2020, pp. 18.3.1-18.3.4, doi: 10.1109/IEDM19573.2019.8993433.

The following **patents** have been filed, partially based on the technology developed within this thesis:

- 'Electronic equipment for the clinical use of graphene transistors in neural interfaces', *No. EP20382819.9* [co-inventor]

- 'Circuit for the multiplexing and read-out of variable-resistance sensor arrays', *No. EP18382593*

1.3   Thesis structure

This thesis has been submitted as a compendium of articles based on the two primary publications *'Improved metal-graphene contacts for low-noise, high-density microtransistor arrays for neural sensing'* [14] and *'Multiplexed Neural Sensor Array of Graphene Solution-Gated Field-Effect Transistors'* [15] by N. Schaefer et al.. The main text summarizes the articles' outcomes and for more detailed information the appendices A.1 and A.2 can be referred to. Also, additional results are being presented which contributed to complementary publications or have not yet been published.

The structure of the thesis is the following:

In **Chapter 1**, a general introduction to the field of BMIs is provided, shortly summarizing their historic evolution and giving an overview of the state-of-the-art technologies. Remaining limitations and shortcomings are outlined, motivating the efforts made in this thesis to employ the gSGFET technology to overcome them. Basic properties of two-dimensional materials are introduced, focussing on graphene and molybdenum disulfide, as highly promising materials for BMIs.

In **Chapter 2** the graphene solution-gated field-effect transistor (gSGFET) is discussed as an efficient transducer of neural activity, due to its linear transfer function, high transconductance and graphene's biocompatibility. To achieve an accurate representation of highly localized neural activity across a vast number of recording sites, large signal-to-noise ratio and high sensor uniformity are of paramount importance. Hence, current limitations of the gSGFET technology which constrain its sensing performance and the technology's implementation into high-density sensor-arrays are explored. Large metal-graphene contact resistance is found to cause non-linearity of signal transduction, reduce homogeneity and augment low-frequency noise in small devices, which is detrimental to the gSGFET's sensing capabilities in high-density arrays. Exposing the graphene contact region to ultra-violet ozone prior to metal deposition is discussed as an efficient way to provide high quality contacts with low contact resistance and thus strongly improve device performance. Low-frequency noise is the sum of contributions from both contact and channel region of the transistor, hence ways to also reduce the latter are investigated to ultimately equip the

gSGFET with optimal sensitivity. Here encapsulation strategies with complementary thin film dielectrics and self-assembled monolayers are proposed to decouple the graphene film from traps and scattering centres in its surroundings; preliminary results of channel noise reduction are presented. The main outcomes of this chapter have been published in *'Improved metal-graphene contacts for low-noise, high-density microtransistor arrays for neural sensing'* [14] by N. Schaefer et al..

In **Chapter 3**, the gSGFET's compatibility with different multiplexing methodologies, namely time-division and frequency-divison multiplexing, is assessed. The quality of multiplexed recordings is compared to the ones obtained in steady, non-multiplexed operation to ensure signal fidelity; the influence of intersite crosstalk is studied and in-vivo experiments with rodents are used to validate the technology's ability to record brain signals. The results of this chapter have been published in *'Multiplexed Neural Sensor Array of Graphene Solution-Gated Field-Effect Transistors'* [15] by N. Schaefer et al. and in *'Switchless Multiplexing of Graphene Active Sensor Arrays for Brain Mapping'* [16] by R. Garcia-Cortadella et al..

In **Chapter 4**, molybdenum disulfide field-effect transistors MoS_2-FETs are proposed as the switching elements of the sensor matrix, since the direct band-gap of MoS_2 and the resulting large on/off-ratio in MoS_2-FETs make them very suitable for switching applications. As inter-site crosstalk poses restrictions on the scalability of multiplexed sensor arrays, a monolithic integration of such addressing circuitry into the flexible sensor array becomes necessary.

Ultimately, the **Chapter 5** summarizes the results and draws conclusions based on the progress made in this work for the potential of the developed technology as part of a novel class of BMIs. Also, future steps are outlined towards a further upscaling of the fabricated electrocorticography (ECoG) implants to allow simultaneous interfacing with large neural populations across vast brain regions.

Chapter 2

Introduction

In this chapter, we recapitulate the historic evolution of brain-machine-interfaces and explore current state-of-the-art technologies and their limitations. Moreover, we describe the synthesis of the two dimensional materials graphene and molybdenum disulfide, which form the basis for the technology presented throughout this thesis, and briefly discuss their electrical and optical properties.

2.1 Brain-machine interfaces

The term brain-machine interface is typically defined as an uni- or bidirectional communication pathway between the brain and an external device, which can allow both recording and stimulation of neural activity.

2.1.1 Historical evolution and overview

Arguably the advent of brain-machine-interfaces (BMIs) started with Hans Berger's discovery of oscillatory electric activity in the brain in 1924 using electroencephalography (EEG), which is nowadays known as the alpha wave rythmn. In 1977 Jacques Vidal utilized recorded brain activity to control a computer by using EEG recordings from the visual cortex to move a cursor through a maze [17] and in this context first defined the term 'brain-computer interfaces'. In 1988, Stevo Bozinovski and coworkers reported the first use of non-invasive EEG recordings to control the movement of a robot, thus inaugurating the age of neuroprostetics [18]. Since then, many more neuroprostetic devices have emerged, aiming at restoration of impaired sensory, articulatory, motor and cognitive functions such as robotic arms, cochlear and retinal implants. More recently, John Donoghue and coworkers have developed a BMI called BrainGate [19], which is based on a Utah array of rigid silicon needles and has been sucessfully implanted in several paralyzed patients allowing them control over computer cursor movements and robotic arms [20]. Improved micro- and nano-fabrication techniques, combined with novel analytic tools (e.g. machine learning) and augmented computational resources, have led to many further breakthroughs in the past years [21]. Advances in motor control rehabilitation [22, 23], the understanding of the mechanisms of learning and formation of memory [24, 25], the

treatment of neuropsychiatric disorders (e.g. depression) [26, 27, 28] and the synthesis of audible speech using machine learning algorithms [29], attest for the immense potential of BMIs [30]. The ultimate goal is to combine high precision recordings of brain activity with methods of brain stimulation, which would give rise to a new spectrum of possibilities. As the ideal pattern and amplitude of electric stimulation to the brain is highly dependent on the actual state of neural activity at the exact moment of stimulation, differing results and side-effects can result from using the same stimulation protocol [31, 32, 33]. Precise recordings of the brain activity prior to stimulation, combined with its real-time processing would allow adjustment of the stimulation protocol to reduce side effects and improve the efficiency of brain stimulation. This procedure is known as 'closed-loop neuromodulation'. [34]

BMIs are often classified by different levels of invasiveness, ranging from non-invasive electroencephalography (EEG) recording from the surface of the skull, through partially-invasive electrocorticography (ECoG), where sensors are placed directly on the cortex, to highly-invasive intracortical probes. For studies in humans, EEG is often the preferred technique, due to its non-invasive character. However, it has clear limitations in spatial resolution, since the skull creates a relatively large separation between the recording sites and the brain tissue. As this separation leads to reduced sensitivity, only activity of high amplitude resulting from summation over a large neural population (several cm^2 of brain area) is detectable. In addition, non-invasive EEG techniques also have a limit in the range of spectral detection, as averaging over large neural populations may lead to destructive overlapping of fast, highly localized patterns. Moreover, recordings from the scalp are more prone to pick up noise from muscle movements and the environment. Thus, in neuroprostetics, EEG can only be used to detect rather simple functions. By contrast, intracortical recordings are able to provide very high spatial resolution and are therefore often used for scientific purposes in animal models as they allow to selectively target very small neural populations, even down to a single unit level [35]. Due to the high invasiveness of placing rigid shanks into the brain tissue, prolonged implantation causes an immune response called gliosis which eventually degrades the recording quality due to scar formation [36]. While efforts are under way to reduce gliosis by using smaller shanks in combination with novel materials and coatings [37, 38], intracortical probes are currently only considered for application in humans in cases of severe impairment. Also, the number of insertable shanks is strictly limited to prevent excessive tissue damage, which makes it difficult to simultaneously interface with vast brain regions. Here, ECoG offers a well-balanced compromise, providing high signal quality and surface coverage as well as sufficient spatial and spectral resolution with reduced inflammatory and gliotic response. ECoG has gained recognition due to its ability to provide high-resolution mappings to track pathological excitation patterns in epilepsy [39]. More recently, it has also proven its value for exploring fundamental questions in neuroscience, such as the specificity of brain regions to the processing of different visual stimuli [40], the importance of high-frequency activity (70-200 Hz) in decision making [41] and the decoding of imagined speech [42].

The primary target application of the technology developed during this thesis with the context of the BrainCom project is to gain a better understanding of the neural

mechanisms which give rise to the comprehension and expression of speech, which could eventually lead to the development of a new class of neuroprosthetic devices for patients suffering from speech impairment. Language processing is one of the most elaborate cognitive processes and requires a complex interplay of several brain regions, which makes this endeavour highly challenging. Some of the areas contributing to this task are the visual and auditory cortex, the angular gyrus, Broca's area, Wernicke's area and ultimately the motor cortex [43, 44]. Thus a detailed understanding of the underlying mechanisms would require a real-time, high-density mapping of all contributing brain regions. Moreover, it is understood that natural language processing relies on complex cross-coupling of phase and amplitude across the neural spectrum of δ (0.5–4 Hz), θ (4–8 Hz), α (8–12 Hz), β (12–30 Hz) and γ oscillations (30–150 Hz) [45, 46], which demands the employment of sensors able to provide high sensitivity over a broad range of frequencies. This set of requirements combined with the reduced invasiveness and risk of inflammatory response in clinical studies makes ECoG the technology of choice for such endeavour.

2.1.2 Remaining challenges and state-of-the-art BMIs

While the scientific achievements and neuroprostetic capabilities presented in the previous section are already significant, they mostly rely on relatively simple interfaces based on rigid materials with a low number of recording sites and large inter-site spacing, and are unsuitable for long chronic implantation. The lack of available sensor technology of high sophistication has inspired research groups and industrial partners across the globe to investigate alternative materials, fabrication procedures and readout concepts to further push the boundaries of neuroscience and biomedical applications [12, 47, 48, 49, 50]. In the following, some of the most critical remaining shortcomings of current neurotechnologies and recent progress aimed at overcoming them are presented.

Biocompatibility of materials:
One of the major constraints in this field is the biocompatibility of the materials used to fabricate neural interfaces. It equally demands high flexibility to avoid mechanical damage to the corrugated soft tissue of the brain, which pulses at every heartbeat, and a low level of toxicity to prevent gliosis and inflammation. Typical electrode materials used to record neural activity are gold, titanium nitride, platinum, stainless steel, aluminum or iridium-oxide [51, 50]. To decrease the impedance of μ-scale electrodes, which leads to improved recording quality, coatings of porous materials are often added onto the electrode surface. Some examples for such coatings are platinum-black [52], carbon nanotubes and conductive polymers such as PEDOT:PSS (poly(3,4-ethylenedioxythiophene) polystyrene sulfonate) [53, 50]. Yet, concerns regarding their cytotoxicity (e.g. carbon nanotubes and platinum-black) [54] and their long-term stability (e.g. PEDOT:PSS) render many of those materials unsuitable for chronic implantation in humans. Recently, also boron-doped diamond [55] and graphene [56, 9, 11] have been considered for long lasting neural interfaces. Current research seeks to further improve biocompatibility and long-term durability

of neural interfaces to bridge the gap from clinical trials to reliable daily use [57].

Full bandwidth recording capabilities:
Brain activity is commonly classified into slow/infraslow oscillations (frequencies below 1 Hz), local field potentials (LFPs) which are considered to originate from spatio-temporal summation of transmembrane currents (frequencies between 1-300 Hz) and extracellular action potentials of single neurons (frequencies between 300-3000 Hz). Available sensing platforms, however, do not show equally high sensitivity for neural signals in all the different frequency bands. Electrodes for instance show a $1/f^2$ noise shape for low frequencies and become dominated by low thermal noise for higher ones, which makes them a popular tool for the detection of spikes and LFPs. More recently, slow oscillations are gaining more attention in the neuroscience community, as they play an important role in the study of e.g. migraines, brain trauma and epilepsy [58, 59]. In electrodes the gain of the recorded signal depends on the ratio between the input impedance of the recording equipment's pre-amplifier $Z_a(f)$ and the electrode's impedance $Z_e(f)$ (Eq. 2.1) [60].

$$V_{in}(f) = I(f)Z_a(f) = \frac{V_{sig}Z_a(f)}{Z_a(f) + Z_e(f)} \tag{2.1}$$

Simplifying the electrode surface as an ideal capacitor, its impedance is a function of frequency f and capacitance C, the latter one scales with the electrode's active area (Eq. 2.2).

$$Z_e(f) = \frac{1}{2\pi f C} \tag{2.2}$$

Hence, recording slow oscillations with electrodes is challenging due to signal attenuation and only possible for electrodes with large active area. In micro-electrode arrays (MEAs), this results in a trade-off between achieving high sensor density and sensitivity to slow oscillations. In addition to gain attenuation, electrodes are also sensitive to baseline drifts causing artefacts and requiring high-pass filtering to avoid amplifier saturation; both potentially compromising recording quality of slow neural activity patterns [60]. Here, sensing platforms utilizing transistors as sensors offer clear advantages, as they act as intrinsic amplifiers when translating neural activity into current signals. Recording signals in currents makes them much more robust to pick-up noise and they can be easily fed into external current-to-voltage converters which provide additional signal amplification. In the case of a graphene-electrolyte interface, the gSGFET shows a frequency-independent gain for signal transduction [11], enabling high-fidelity full bandwidth neural recordings [9, 11, 60]. Also, since the device's bias point is fixed by a reference electrode it is much less susceptible to artefacts from reference drifts.

Connector footprint and sensor density:
As previously mentioned, higher cognitive functions typically arise from a complex interplay of simultaneous activity in several brain regions. Therefore, their detailed analysis equally demands high local resolution and large brain surface coverage. Commercial solutions still fail to match these requirements, mostly due to the technological challenge of excessive wiring with increasing array size. As each sensor has

to be individually connected to a macroscopic acquisition system, providing both signal amplification and transmission, an equal amount of wires and sensors is required, which due to space limitations typically results in a trade-off between achievable sensor density and covered area. A common approach to overcome this bottleneck is the employment of multiplexed read-out circuitry which allows shared wires between several sensor columns and rows. Multiplexed sensor arrays in neuroscience have been predominately used for depth probes, which do not necessitate flexible substrates and thereby allow a monolithic integration of silicon-based readout circuitry on the probe shank. Some of the most notable examples of this approach are the NeuroSeeker [61], NeuroPixels [48] and SiNAPS [62] platforms. However, rigid probe shanks cause augmented scar formation and gliosis in the surrounding brain tissue, due to their difference in Young's modulus, which in turn leads to a gradual loss of signal sensitivity during long-term chronic implantation. A combination of flexible depth probes with an externally placed ASIC (Intan technologies) has been proposed [49] as a solution to overcome this mechanical mismatch. However, such an approach is likely to show higher pick-up noise due to the large electrode-to-amplifier distance. In ECoG probes, a monolithic implementation with silicon-based integrated circuitry is challenging, as its placement on the cortical surface demands high conformity with the corrugated brain tissue, making the use of all-flexible technology mandatory. Unfortunately, flexible electronic materials of high mobility and wide band-gap which would allow rapid multiplexing without loss of signal quality are scarce. Only a few notable examples of ECoG-arrays with monolithically integrated multiplexed readout have been reported so far. The most prominent is the work of Rogers and co-workers, which uses ultra-thin silicon technology to address an array of platinum electrodes and transduce their recorded signals [63, 12, 64]. However, this implementation requires highly complex fabrication procedures restricting its widespread application and does not offer sensitivity to infra-slow brain activity. Also, multiplexed ECoG arrays based on organic polymers for both sensing platform and flexible switches have been explored, yet the relatively low carrier mobilities in semiconducting polymers do limit the achievable switching speed [65]. Further, it has been shown, that in the case of low track resistance such a concept could be strongly simplified by placing the addressing switches externally without deteriorating the recording quality [66, 22].

2.2 Two-dimensional materials for flexible sensor-arrays

2.2.1 Graphene

Upon discovery, graphene has been hailed the wonder material of the 21th century, due to its properties such as its mechanical strength [1] and flexibility, optical transparency [2], chemical stability, biocompatibility [3], high carrier mobility [4] and linear energy dispersion. This potential has lead to extensive investigations for application of graphene in numerous fields such as electronics [5], photonics and
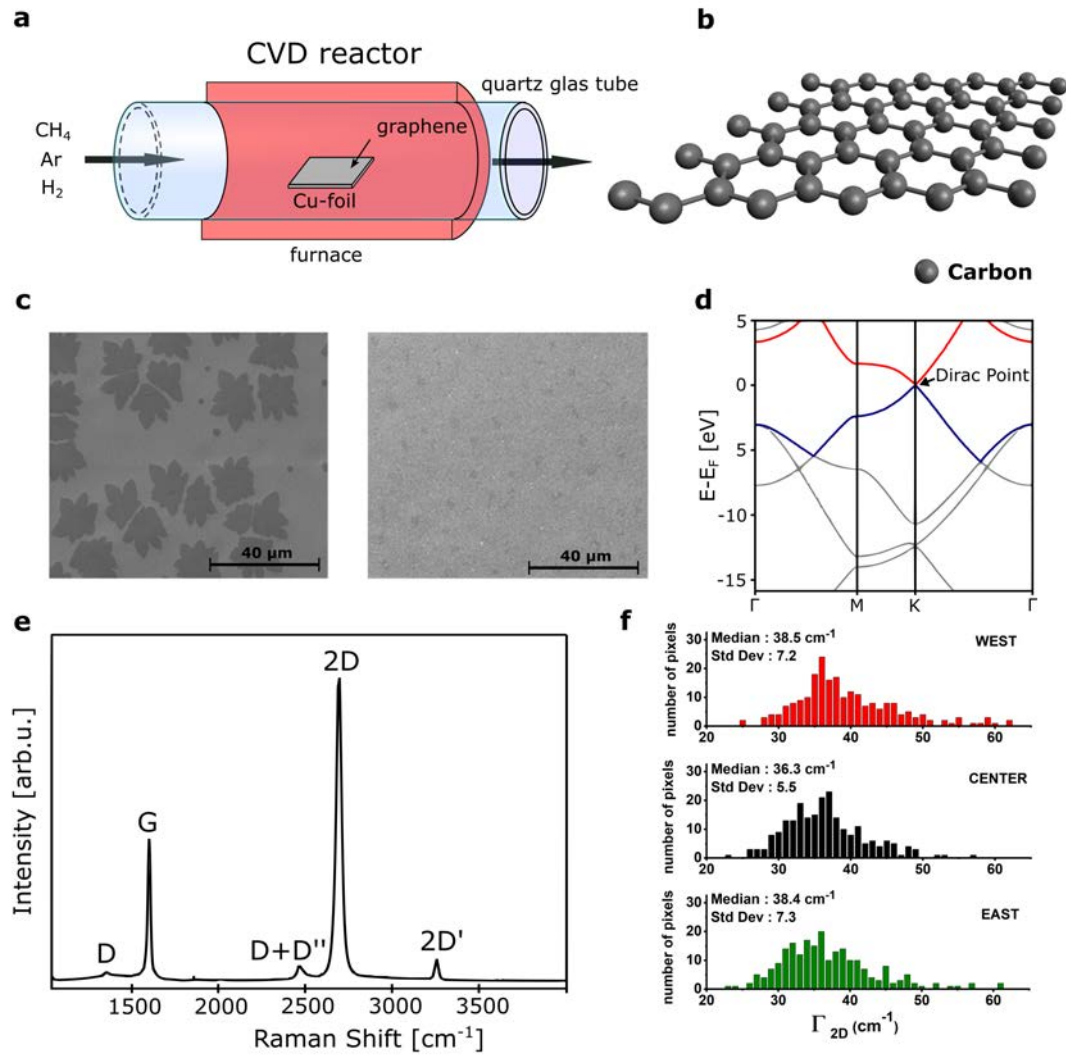
Figure 2.1: Graphene synthesis and properties: a. Schematic of a hot-wall CVD reactor design using methane as a carbon precursor. **b.** Schematic showing a graphene monolayer with its characteristic hexagonal arrangement of carbon atoms. **c.** SEM images of a partially closed (left) and a fully closed graphene layer (right) grown on a copper foil, revealing grain sizes around 20 μm. **d.** Band structure of monolayer graphene showing the valence (blue) and conduction band (red) which meet at the Dirac point. **e.** Raman spectrum of monolayer graphene and its characteristic peaks. **f.** Histograms of the full-width at half-maximum (FWHM) of the 2D-peak across three positions on a CVD-grown graphene sample.

optoelectronics [67], and more recently biomedical engineering [68, 69, 9]. In the following, I briefly discuss the synthesis and the optical and electronic properties of graphene.

Growth

Historically, graphite has been utilized as a lubricant, due to the weak Van-der-Waals interactions between its stacked layers. Weak inter-layer bonds are a critical property for the synthesis of two-dimensional materials, as this allows the use of me-

chanical exfoliation techniques to separate monolayers from the bulk material. While mechanical exfoliation is still setting the benchmark in terms of crystal-quality and film homogeneity in graphene sheets, it does not present a scalable technique when moving towards large-scale fabrication of graphene-based technologies, due to the relatively small obtainable flake size [70]. The most promising alternative so far is chemical vapor deposition (CVD), which presents a cheap and highly-scalable technique, using a gaseous mixture of argon, hydrogen and the precursor methane [71]. The latter is being decomposed under high temperature, with its carbon atoms subsequently re-nucleating on a catalytic metal substrate (typically Cu foils), reassembling to high-quality single-layer graphene films. Figure 2.1a illustrates a typical hot wall reactor set-up for CVD growth, and figure 2.1b show the hexagonal atomic structure of carbon atoms in graphene. The quality and uniformity of the graphene film can be inspected by scanning electron microscopy (SEM). Figure 2.1c shows SEM images of an open graphene layer (left) with domain sizes between 10 μm and 20 μm and a closed layer (right) with low amount of second nucleation and presents the typical material quality achieved with the used reactor. After growth, the underlying Cu foil can be removed through electrochemical etching, leaving a free standing film of single layer graphene, which can then be transferred onto a target substrate. A detailed description of the growth and transfer procedure can be found in the literature [14, 11, 60].

Optical properties

Integration of two-dimensional materials into devices requires the availability of non-destructive characterization techniques, necessary to monitor the film quality after growth and throughout the device fabrication process. Raman spectroscopy exploits inelastic scattering processes of monochromatic laser light (typically in the visible spectrum), which exhibit resonances with vibrational and rotational low-frequency modes in the sample's crystal structure [72]. In the case of Graphene, this information allows for instance to identify the number of layers, to estimate the density of defects, quantify the amount of surface contamination and detect the presence of mechanical strain [73]. There are several important Raman modes in Graphene. The **G-band** is a sharp peak at approximately 1587 cm^{-1} which stems from an in-plane vibrational mode of the sp^2-hybridized carbon atoms. The band's position and intensity can be used as a measure for the number of layers. However, as its position also depends on other factors such as temperature, doping and strain, the peak intensity often offers more reliable results [74]. The **D-band** is typically observed at around 1350 cm^{-1}. However, since it consists of a superposition of several individual resonance modes, its exact position and shape depend on the used excitation energy and thus laser wavelength. This band results from a ring breathing mode of sp^2 carbon rings, which due to symmetry is not visible in the case of a perfect graphene structure. Yet, it becomes visible if it is placed next to a graphene edge or structural defects which make it a reliable indicator to quantify disorder and defects in graphene [75]. The second order harmonic of the D-band is the **2D-band** which is a two phonon lattice vibrational mode and is always visible

in graphene, even in the absence of structural defects. The position and shape of the 2D-band can also be used to determine layer thickness in graphene [74]. The full-width at half-maximum (FWHM) of the 2D-peak is around 30 cm^{-1} for a single layer graphene and increases with the number of layers. As an additional criterion to quantify the layer number, the peak intensity ratio I_{2D}/I_G can also be used and lies typically around 2 for single-layer graphene, however can vary for different substrates and impurity densities. Finally the **D'-band** and **D"-band** correspond to other defect-activated modes which originate in an intra-valley and inter-valley scattering process, respectively [73]. However, due to their proximity to the G-band, they are not directly visible for samples with low density of defects. Next to the mentioned principle peaks, we can observe further second order and combination peaks such as the 2D'-band and the D+D"-band. As a general rule of thumb the most important parameters to assess monolayer graphene quality are the I_{2D}/I_G ratio, the absence of the D-band and a sharp 2D-peak. Figure 2.1 e shows a typical Raman spectrum of a 30 μm x 30 μm map of the CVD-grown graphene used in this thesis. The spectrum corresponds to a sample with low defect density and high uniformity across the entire sample and a I_{2D}/I_G ratio of close to 2, indicating a low percentage of second nucleation. Figure 2.1 f shows histograms of the variation of the full-width-half-maximum (FWHM) of a graphene film across three different locations on the sample roughly 2.5 cm apart, indicating a fairly high uniformity of the grown film.

Electronic properties

The carbon honeycomb structure of graphene creates in-plane σ orbitals, which form strong covalent bonds between neighbouring atoms and give rise to the mechanical strength of graphene and its high Young's modulus of 0.5 TPa [76]. The electronic properties, however, are determined by the out-of-plane p_z atomic orbitals, which create the valence and conduction bands π and π^*. What makes graphene different from standard semiconducting materials is that both bands touch at the K points forming a zero-bandgap semiconductor. The energy dispersion relation of graphene can be approximated using a nearest-neighbour tight-binding Hamiltonian, resulting in Eq.2.3 (first described by [77]), and is illustrated in Figure 2.1d. γ denoting the nearest-neighbour hopping energy, a the lattice constant and k_x, k_y the respective components of the wave vector.

$$E_\pm(\mathbf{k}) = \pm\gamma \sqrt{\left(1 + a\,cos^2\left(\frac{\sqrt{3}k_y a}{2}\right) + 4\,cos\left(\frac{\sqrt{3}k_y a}{2}\right) cos\left(\frac{3k_x a}{2}\right) \right)} \qquad (2.3)$$

Close to the Dirac points (K and K'), the charge carriers behave like massless relativistic particles, called Dirac fermions, and their energy dispersion can be described by Eq.2.4, with υ_F being the Fermi velocity and $\hbar$ the Planck constant.

$$E_\pm(\mathbf{k}) = \pm\hbar\upsilon_F \sqrt{\mathbf{k_x}^2 + \mathbf{k_y}^2} \qquad (2.4)$$

This linear dispersion relation distinguishes graphene from regular semiconductors, which typically exhibit a quadratic relation and have a band-gap between the valence and conduction band. The extremely high carrier mobility of graphene originates from its near-ballistic transport at room-temperature and is theoretically predicted to reach up to 200 000 $cm^2V^{-1}s^{-1}$ (more than 100 times higher than that of silicon) until it is limited by acoustic phonon scattering [78]. However, on SiO_2 substrate, the room-temperature mobility does not exceed 40 000 $cm^2V^{-1}s^{-1}$ due to extrinsic scattering with surface phonons [79], which makes the choice of substrate highly important for high-performance devices. Experimental values for carrier mobility in CVD-grown graphene are reported up to 350 000 $cm^2V^{-1}s^{-1}$ [4] for low temperatures, which is comparable to those found in exfoliated flakes. Ultimately, charged impurity scattering becomes an important limiting factor in many applications , as surface contamination from organic residues during device fabrication (e.g. photoresists) is difficult to avoid [80]. A proper control of the electronic properties of graphene and related two-dimensional materials plays an important role for the technology developed during this thesis, as it critically affects the sensitivity and noise of the developed sensors as well as the addressability of such in arrays of large sensor counts.

2.2.2 Molybdenum disulfide - MoS$_2$

Despite its range of impressive properties, graphene is not a suitable material for digital electronics as it cannot provide a large band-gap, necessary for the design of transistors with high on/off-ratios which are essential to build logic circuits for digital electronics. Hence, great efforts have been devoted to investigating complementary two-dimensional materials which could fill this gap. Transition metal dichalcogenides (TMDCs) are being intensively explored as a substitute, due to their semiconducting properties combined with their optical transparency and their mechanical flexibility [81]. Similar to graphene, TMDCs also show a layered structure with strong intra-layer (covalent) and weak inter-layer bonds (Van der Waals), which allows easy mechanical exfoliation of single layer films. TMDCs are classified by the chemical formula MX_2, with M being a transition metal (e.g. Mo, W, Hf, Ti, etc.) and X being a chalcogen atom (i.e. S, Se, Te). Interestingly, TMDCs exhibit a layer-dependent transition from an indirect band-gap in its bulk and multilayer form to a direct band-gap for monolayer thickness [81]. Direct band-gap semiconductors are favourable for photodetectors, photovoltaics and light-emitting diodes (LEDs), as they provide augmented photoabsorption and photoemission [82]; this is the reason why TMDCs have received so much attention for optoelectronic applications. Moreover, semiconducting TMDCs such as MoX_2 and WX_2 also show great promise for applications in digital electronics due to their large band-gaps, ranging from 1.1 eV to 1.9 eV, similar to the one of silicon. Digital elements in logic circuits are required to have large On/Off-ratio of at least 10^4 to reduce noise, cross-talk and power dissipation as well as to provide fast switching speeds for high-frequency applications. This equally requires materials with large band-gap, high carrier mobility and charge carrier density [82]. Another interesting feature of TMDCs in
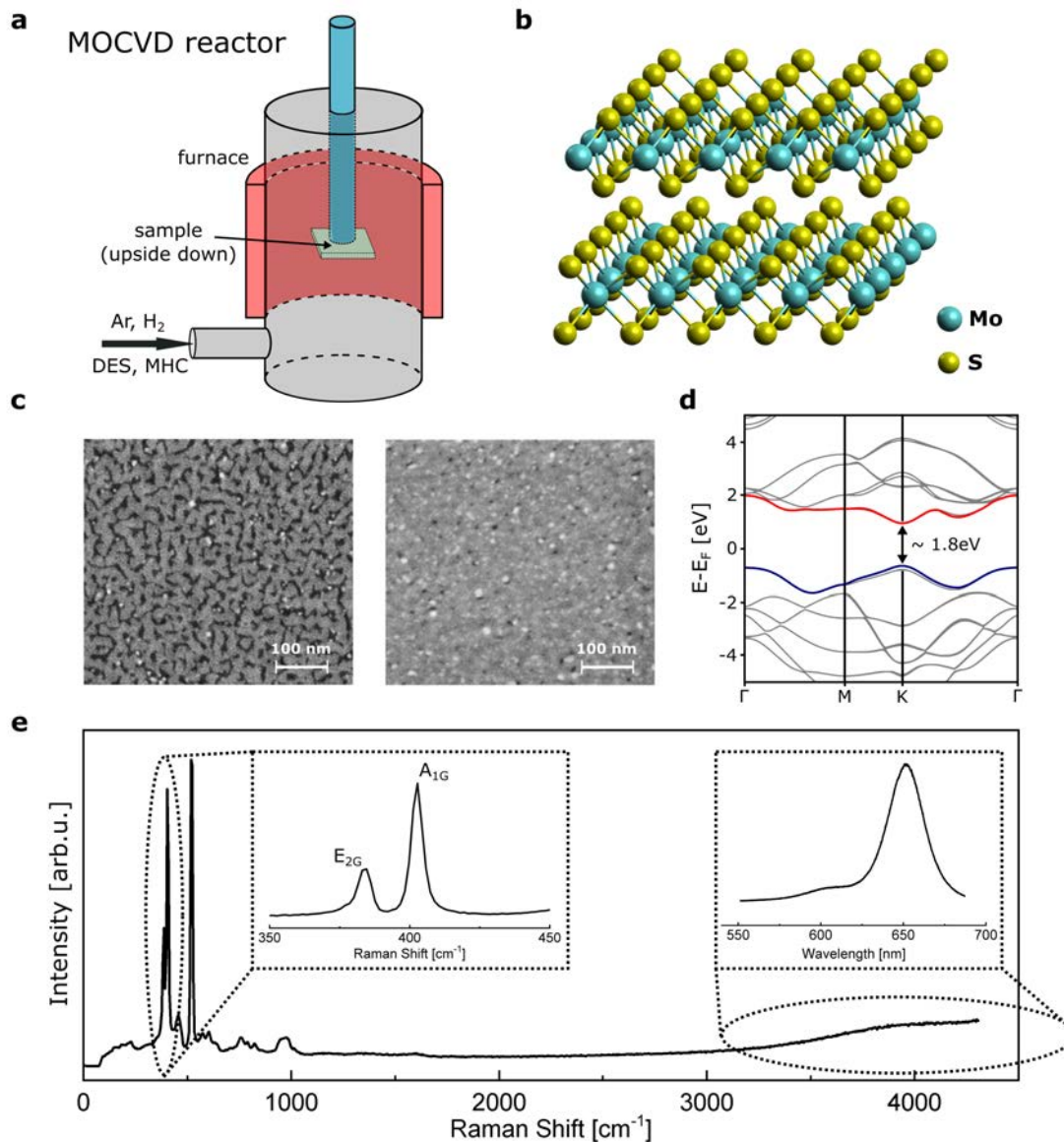
Figure 2.2: Molybdenum disulfide: a. Schematic of a hot-wall MOCVD reactor design for the growth of MoS_2 using molybdenum hexacarbonyl (MHC) and dimethyl sulfide (DES) precursors. **b.** Atomic structure of molybdenum disulfide, showing a vertical stack of single layer films. **c.** SEM images of a partially closed (left) and a fully closed MoS_2 layer (right), as grown in the home-built reactor of the AEMD group, indicating grain sizes around 25 nm. **d.** Band structure of monolayer MoS_2 showing the valence (blue) and conduction band (red), separated by a direct band-gap of 1.8 eV. **e.** Raman spectrum showing the dominant vibrational modes and the photoluminescence peak of monolayer MoS_2 on Si/SiO_2 substrate. Credits for the SEM and Raman images belong to Christian Schäfer from the Catalan Institute of Nanoscience and Nanotechnology (ICN2).

electronic components (e.g. transistors) is their lack of short-channel effects and low power dissipation [82, 5], that would otherwise hinder device performance and set current size limitations in regular MOSFET technology. This might eventually allow an increased level of integrated circuit miniaturization beyond the current state of the art. Finally, the two-dimensional nature of TMDCs or other low-dimensional

materials and the resulting mechanical flexibility and optical transparency open up new fields of applications such as wearable electronics [82]. Within this thesis, we focus on one of the best explored TMDCs, molybdenum disulfide (MoS$_2$) with a direct band-gap of 1.8 eV in its monolayer form [82], a large on/off-ratio [83], a fast transient response and high mechanical flexibility, which makes it an ideal candidate to explore for the implementation of flexible on-site switches for multiplexed sensor arrays.

Growth

Similar to graphene, MoS$_2$ can also be produced by regular CVD growth, typically involving vaporization of molybdenum trioxide (MoO$_3$) and sulfur inside a heated chamber [84, 85, 86, 87, 88]. Yet, due to the fast evaporation rate of sulfur, nucleation density, deposition rate and surface coverage are difficult to control and reproducibility is limited. A promising alternative is the use of metal-organic precursors (MOCVD) with high vapor pressure, allowing to vaporize them externally of the deposition chamber and thus providing a more accurate control of the gaseous mixture for more stable growth conditions [89, 90, 91]. Figure 2.2a-c show a schematic of the home-built MOCVD reactor used in our group for the growth of MoS$_2$, the atomic structure of MoS$_2$ and SEM images (kindly provided by Christian Schäfer) showing an open (left) and closed (right) film of monolayer MoS$_2$ grown on a Si/SiO$_2$ substrate. Here the two gas-phase precursors molybdenum hexacarbonyl (MHC) and dimethyl sulfide (DMS) were used to grow the MoS$_2$ film. The MoS$_2$-FET technology which is presented in this thesis, is partly build from material grown with our custom-build reactor and partly from material provided by the group of Prof. Dr. Thomas Müller at the Technical University of Vienna [92].

Optical properties

Raman spectroscopy can be used to identify the number of layers of MoS$_2$ by measuring the distance between the two dominant phonon modes E$_{2G}^1$ and A$_{1G}$ (left inset in figure 2.2e) which are located at 386 cm^{-1} and 405 cm^{-1} for monolayer MoS$_2$ films [93]. The E$_{2G}^1$ peak corresponds to an in-plane vibrational mode and the A$_{1G}$ peak to an out-of-plane mode. With increasing number of layers the E$_{2G}^1$ peak red shifts and the A$_{1G}$ blue shifts, increasing the distance between both peaks [93]. The direct band-gap in single-layer MoS$_2$ makes the material photoluminescent; a broad PL peak (right inset in figure 2.2e) can be observed in the 600 nm to 700 nm wavelength range.

Electronic properties

As previously mentioned, MoS$_2$ transitions from an indirect band-gap of 1.2 eV in its bulk form, to a direct bandgap of 1.8 eV for monolayer MoS$_2$ (energy diagram in Figure 2.2d), which makes it interesting for applications in optoelectronics, photonics and digital electronics. MoS$_2$ is typically a n-type doped semiconductor, however its type can depend on the charge polarity of traps in its proximity and p-type

MoS_2 is also possible [94]. Typical charge carrier mobilities measured in CVD-grown MoS_2 monolayers range from 0.01 to 20 $cm^2V^{-1}s^{-1}$ and are much lower than the ones observed in the bulk form. This mobility reduction can be attributed to the high surface-to-volume ratio in thin films, which makes them particularly exposed to charged impurities in the channel proximity. When measured in ambient environment, MoS_2 is highly susceptible to surface adsorbates such as H_2O and O_2, that modify the doping level and carrier mobility and cause significant hysteresis [95]. This susceptibility to the environmental conditions makes encapsulation strategies imperative [96]. Common materials used for encapsulation and as gate dielectrics in MoS_2-FETs are oxides such as Al_2O_3 and HfO_2, with the latter yielding better results due to improved gate-coupling and charge-impurity screening as a consequence of the higher κ value [97].

Chapter 3

Performance-enhanced graphene sensors

In view of the vast potential of graphene in different application fields, it is unfortunate that graphene-based devices often fall short of demonstrating their full capabilities, mostly due to limitations such as large metal-graphene contact resistance [98], inhomogeneity among devices [99] and high flicker noise [100], which still hamper their performance. Much effort has been aimed at overcoming such limitations by modifying contact design for improved charge injection, increasing material and technology uniformity and implementing mitigation strategies to lower electronic noise. The graphene solution-gated field-effect transistor (gSGFET), being one of many very promising graphene-based technologies, has proven its value as a powerful tool for electrophysiology [11, 60] pairing high sensitivity to neural signals with mechanical conformability and biocompatibility. In the following, the effect of before-mentioned limitations on the device's sensing capability are investigated and strategies are explored which would allow to unlock the gSGFET's full potential.

3.1 Graphene solution-gated field-effect transistor

Field-effect-transistors (FETs) are three-terminal devices which allow modulation of the current flow through a semiconducting channel material by the application of an electric field. In most applications, this electric field is generated by an external gate electrode, which applies a bias across an oxide layer separating the gate electrode from the channel. This concept has laid the foundation for digital circuitry, where control of the gate bias allows to switch between a state of high (on-state) and low conductivity (off-state). The correlation between the current flow and the applied electric field, which is defined as the transconductance of the device, can also be used to build highly sensitive sensing devices to detect for instance neural activity. Neural activity on a microscopic scale arises from changes in ionic concentrations (e.g. sodium and potassium) across the cell membrane of neurons and results in fluctuations of the local electric field. The easiest way to detect such fluctuations with a
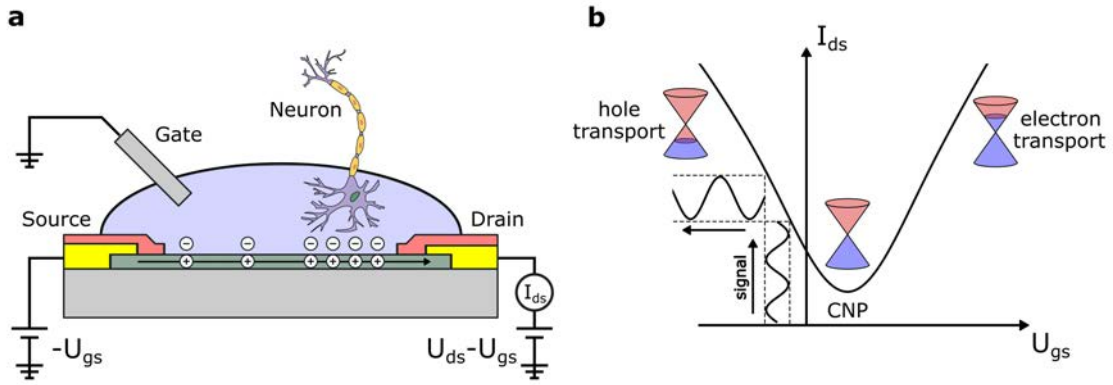
Figure 3.1: Graphene solution-gated field-effect transistor: **a.** Schematic of the graphene solution-gated field-effect transistor (gSGFET) with the drain, source and gate terminal. The applied gate voltage controls the bias point of the device and local electric fields from neural activity in the device's proximity cause measurable fluctuations of the charge carrier density. **b.** Transfer curve of the drain-source current I_{ds} versus the applied gate voltage U_{gs}, showing an electron and a hole transport regime depending on the applied gate voltage with respect to the charge-neutrality-point (CNP).

FET is to directly expose the semiconducting channel to the resulting electric field and measure the corresponding change in current flow. This idea has been employed in solution-gated field-effect transistors [101], which in contrast to their solid-state counterparts, are being modulated through the creation of a charge double layer at the interface between transistor channel and an electrolyte solution (Figure 3.1a). Potential fluctuations in the surroundings (e.g. neural activity) can then modulate this double layer and result in a shift of the Fermi level of the channel material, which changes the number of charge carriers and is thus detectable as a current fluctuation. Graphene's ability to create a stable interface with aqueous solutions, in combination with its high transconductance, resulting from its large interfacial capacitance and carrier mobility, makes it an ideal material to employ this concept [11, 9, 60, 101, 102, 103, 56]. Figure 3.1b shows a typical I_{ds}-U_{gs} transfer curve of the gSGFET, explaining how the number of free carriers changes with the applied bias at the gate electrode due to a shift in the Fermi level of the graphene sheet. The band structure of graphene allows operation of the transistor in either a hole or an electron transport regime, which are separated by the Dirac point where both the conduction and valence band meet. The gate voltage corresponding to the position of the charge-neutrality-point (CNP) depends on the electrochemical potential of the used reference electrode as well as on doping of the graphene sheet due to e.g. organic residues, underlying substrate or growth defects. Figure 3.1b also indicates how voltage fluctuations due to changes in electric field translate into corresponding current fluctuations in the measured signal. The slope of the transfer curve (drain-source current changes for a specific gate voltage change), also called transconductance g_m, plays an important role here, as it defines the amplification factor during this transduction and thereby influences the gSGFET's sensitivity. The gSGFET sensor arrays which form the basis of the technology developed in this thesis have been fabricated by standard microfabrication techniques as described

in C.1 and the literature [14, 15]. Having reviewed the electronic origin of the gS-GFET's sensitivity to neural activity, we want to next discuss on the origins and implications of low-frequency noise in the gSGFET.

3.2 Low-frequency noise

Low-frequency noise in transistors is of critical importance to many electronic applications, and has motivated intense research interest since the advent of the semiconductor industry [104]. Electronic noise plays a particularly important role in graphene-based technologies such as biologic sensors, photodetectors and high-frequency devices, as their functionality is often founded on the record high carrier mobilities in graphene and the accurate control of the number of charge carriers in the channel. In particular, due to the small signal amplitude of brain activity when measured from the cortical surface, low noise plays a paramount role when developing neural sensors for ECoGs. Thus, the sources of noise have to be well understood to minimize their impact on the device performance.

There are different sources of noise in graphene field-effect-transistors, namely thermal noise, flicker-noise, shot noise and generation-recombination (G-R) noise. Thermal and shot noise show a flat distribution over all frequencies and result from random motions of charge carriers [100]. Thermal noise is determined by the Nyquist formula $S_I(f) = 4k_BT/R$ with k_B being the Boltzmann constant, T the temperature and R the channel resistance. Shot noise is described by Schottky's theorem $S_I(f) = 2q\langle I \rangle$ where $\langle I \rangle$ is the average value of the electric current and q the elementary charge [100]. The most important contribution at low frequencies, however, arises from flicker-noise which for most semiconductors shows an inverse proportionality to the frequency. Therefore the frequency f_0 at which thermal or shot noise become more dominant than flicker noise is often used as a figure of merit for the noise performance of a device and for graphene FETs typically lies in the range of 1 Hz to 100 kHz [100]. The current normalized amplitude of flicker noise typically scales inversely with the channel volume, and, in the case of two-dimensional materials, the channel area [100]. While the origin of flicker noise is yet to be fully understood, it is commonly agreed upon that the statistical fluctuations of electrical current I (Equation 3.1) leading to this type of noise originate in either fluctuations in the mobility of charge carriers μ (the dominant source in metals) or fluctuations in their number N (the dominant source in semiconductors).

$$I \propto qN\mu \Rightarrow \delta I \propto q(\delta N)\mu + qN(\delta\mu) \tag{3.1}$$

In the case of noise dominated by mobility fluctuations, the empirical Hooge formula [105] is used to describe the noise distribution. When charge carrier fluctuations dominate, the 1/f-shape can be explained by the McWorther model. Here charge carriers get captured in charge traps in e.g. the surrounding oxide layer and re-emitted into the channel, causing current fluctuations which lead to noise. The duration of such a charge trapping process depends on the distance of the trapping centres to the channel and can have quite different time scales. The summation

31

of the G-R bulges corresponding to each of such trapping state, then results in a 1/f-shaped spectrum. Charge carrier noise is often also described as surface noise, as it becomes more pronounced for thin channel materials, due to increasing influence of charge traps in the proximity. Accordingly, mobility noise can be referred to as volume noise as it prevails in bulk materials [106].

In the case of graphene, however, this differentiation between the two distinct noise sources cannot be made so easily, as it features both metallic and semiconducting properties, which can lead to comparable contributions of either type of flicker noise. Yet, their geometry makes graphene-based devices more prone to be dominated by charge carrier noise, unless the channel material is decoupled from proximity traps by e.g. channel encapsulation, fabrication of free-standing films or stacking of multiple graphene layers [107, 108, 109]. The presence of two dominant noise sources, combined with additional noise contributions from the contacts, also leads to a complex gate bias dependence of flicker noise in graphene FETs, which neither follows the Hooge nor the McWorther's model [110]. In the case of solution-gated graphene transistors, it has been shown that an augmented charge-noise model can be used instead, differentiating between a low carrier density regime in which the noise is mostly caused by trapping-detrapping of carriers and a regime of high carrier density, where scattering processes within the channel become dominant [110]. In the first case there is a clear dependence of the level of current noise on the charge carrier density and therefore the bias point, in the second case it is nearly gate-independent. This complex bias dependence typically results in a M-shape behaviour of the current noise in monolayer graphene FETs for varying gate bias, with a minimum at the Dirac point [111]. In devices where the contact noise contributes significantly on the other hand, a V-shape behaviour is generally observed, with monotonic noise increase away from the CNP [14]. Considering these two distinct origins of flicker noise in graphene FETs, namely the channel and the contact region, achieving the objective of record-low noise performance requires addressing both components. In the following, we explore in more detail the underlying processes which are the primary sources for augmented current noise in either region and suggest strategies for their respective reduction.
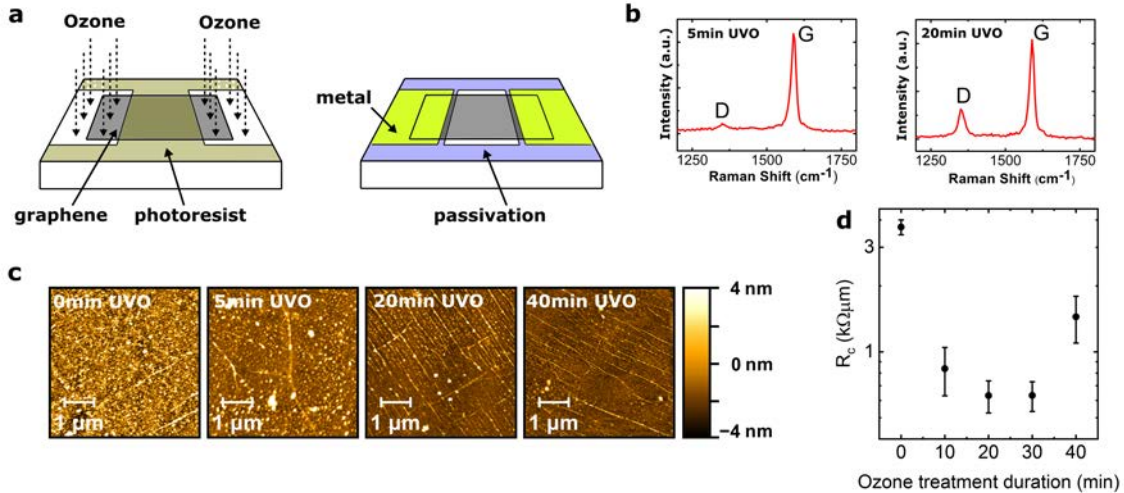
3.2.1 Contact noise

Figure 3.2: **Contact resistance reduction in gSGFETs: a.** Schematic of device fabrication with ultra-violet ozone (UVO) applied to the graphene contact region prior to the metal deposition. **b.** Raman spectra after 5 min and 20 min UVO treatment. **c.** Surface roughness of the graphene layers measured by AFM. The lowering of the root-mean-square values with longer UVO treatments (2.1 nm, 1.3 nm, 1.1 nm and 0.8 nm, for 0 min, 5 min, 20 min, and 40 min duration, respectively) indicates the continuous cleaning of surface residues. **d.** R_c at U_{gs}-CNP = -0.5 V as a function of UVO-treatment duration, showing optimal results for 20-30 min UVO exposure. Adapted from [14].

The origin of contact noise and its impact on device performance has been the subject of much debate [112, 100, 14, 107] and no consensus has yet been reached. Contact noise results in part from time-dependent resistance fluctuations at the metal-channel interface and thus becomes more pronounced with increasing contact resistance. High contact resistance is a common challenge in graphene devices, caused by the lack of dangling bonds, the work function mismatch between graphene and contacting metals and the low density of states in graphene, which results in a poor charge carrier injection [98, 113, 114]. Mitigation strategies to overcome this issue include the intentional creation of defects in the graphene sheet through its exposure to for example oxygen plasma [115] or ozone [116], and the use of contact metals which interact strongly with graphene (e.g. Nickel) [117, 118, 119].

To lower the metal-graphene contact resistance in gSGFET technology, several approaches have been tested. In this thesis, optimal results across many devices in wafer-scale fabrication were achieved by exposing the contact region of the graphene active areas to ultra-violet ozone (UVO) prior to metal deposition (Figure 3.2a). The main results of this work have been published in [14] and will be briefly discussed hereafter. This technique has previously been reported to significantly improve charge injection through both surface cleaning of fabrication residues and defect creation in the graphene sheet [116, 120]. Figure 3.2d shows contact resistance measured as a function of the UVO treatment duration, with the contact resistance being obtained by the application of the transmission line method (TLM) to measured channel resistance values for devices of different channel length and constant

channel width. The minimal measured value for the contact resistance lies around 600 $\Omega\mu$m and corresponds to a 20-30 min exposure of the contact region to UVO. Figure 3.2b-c show atomic force microscopy (AFM) images and Raman spectra for untreated and UVO-treated contact regions. The surface roughness decreases from 2.1 nm to 1.1 nm with the treatment, indicating a significant cleaning of the graphene surface. The Raman spectra show a clear increase of the D-peak amplitude, which can be attributed to the generation of defects in the carbon lattice.
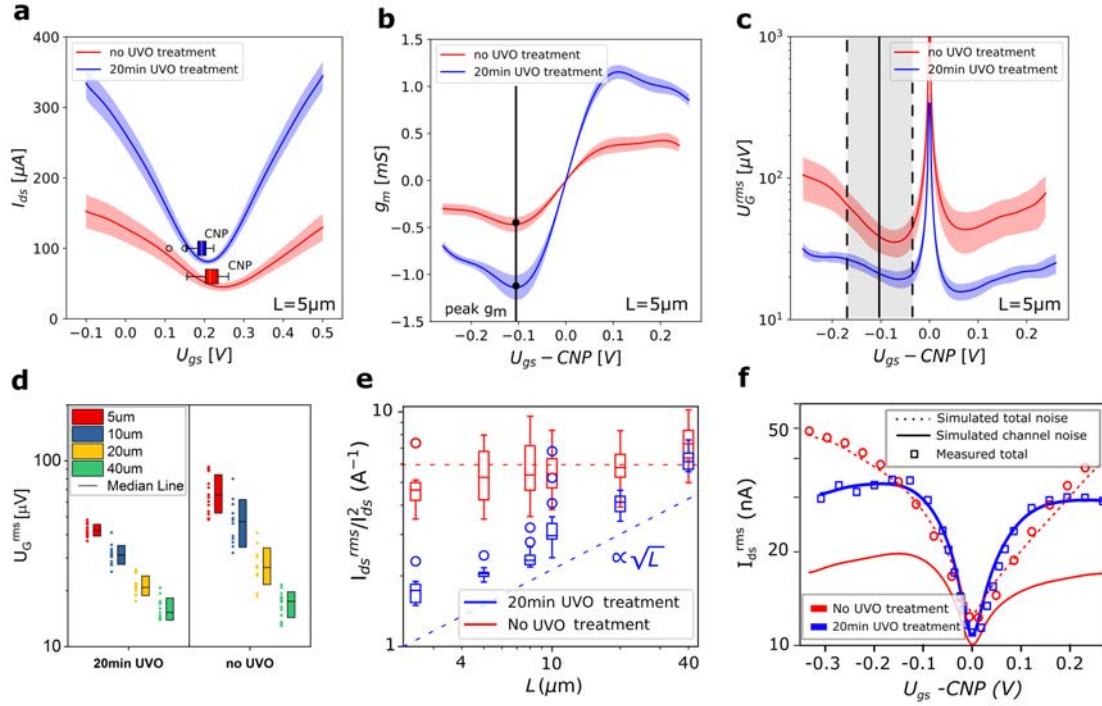
Figure 3.3: Reduction of contact noise in gSGFETs: Average value and standard deviation of transfer curves for **a.** drain-source current I_{ds}, **b.** transconductance g_m and **c.** effective gate noise U_G^{rms} for devices of 5 μm channel length and 40 μm channel width. **d.** Statistical variation of U_G^{rms} values at peak transconductance (U_{gs} = CNP - 0.1 V) for devices of different channel length and 40 μm width. **e.** Dependence of the normalized current noise I_{ds}^{rms}/I_{ds}^2 (U_{gs} = CNP - 0.1 V) versus the channel length (L) for devices with non-treated and treated contacts. **f.** Experimentally measured integrated current noise I_{ds}^{rms} versus U_{gs}, plotted for non-treated and treated contacts in devices of 5 μm channel length. The lines correspond to the fitting of the experimental data with a model that considers the contributions of the channel noise only (solid line) and of both, channel and contact noise (dashed line). Adapted from [14].

Figure 3.3a illustrates the effect and importance of improved contact resistance on the operation of the gSGFET as sensor of neural activity. Device fabrication and device design of the used gSGFETs are described in more detail in A.1. The I_{ds}-U_{gs} curve shows a flattening of the Dirac cone away from the CNP due to the additional serial resistances at the contact. This has significant ramifications for the sensitivity of the gSGFET sensor, as it limits the linear regime of the device's transfer curve and can result in distortions of the transduced signal affecting signal fidelity. Also, does it lower the device's transconductance g_m and thereby the gSGFET's sensitivity for neural fluctuations. Typically, the bias point of peak transconductance (Figure

3.3b) is chosen to operate the gSGFET, as it provides the best signal amplification. A two-fold increase of peak-g_m due to contact improvement can be observed. More important than the transconductance, which only measures the sensitivity, however, is the effective gate noise U_G^{rms}. This parameter which is derived by dividing the intrinsic current noise I_{ds}^{rms} of the device by g_m, represents a reliable way to measure the signal-to-noise ratio (SNR). Figure 3.3c shows that the reduced contact resistance also results in a notable reduction of U_G^{rms}. Furthermore, U_G^{rms} remains relatively constant with changing U_{gs} which results in a wide bias windows of large SNR and thereby optimal sensing ability. Interestingly, this improvement strongly depends on the device's geometry (Figure 3.3d), being most pronounced for short channel lengths. In addition to noise reduction, the noise dispersion across several devices strongly improves. Device homogeneity is important in sensor arrays since it allows uniform recording quality of all sites on the array. The observed reduction of U_G^{rms} as a consequence of low contact resistance poses the question about the weight of the individual contributions of the contact and channel noise to the total noise. The geometric dependence of each noise source can be theoretically derived; it exhibits a $\sqrt{L}$ proportionality when channel noise dominates but remains constant with L if contacts are the dominant source [14]. Plotting the experimentally measured normalized current noise for devices of varying channel length, noise in devices with untreated contacts remain fairly constant (Figure 3.3e). However, devices with UVO-treated contacts (20 min treatment duration) show a transition from this approximately L-independent regime to a $\sqrt{L}$-proportional regime (Figure 3.3e). For gSGFETs with channel length of around 60 μm, both noise sources contribute equally to the total normalized noise, yet for shorter devices with shorter channels, the normalized current noise is significantly lower in the case of UVO-treated contacts (Figure 3.3e). Here it should be noted, that the observed U_G^{rms} improvement is not solely a consequence of the increase in g_m, but also of a decrease of the intrinsic contact noise. To further explore the transition from a contact noise to a channel noise dominated regime, the gate-bias dependence of the measured total noise can be modelled using a channel noise model for gSGFETs [111] and adding the contact noise contribution to it [14]. It can be seen in Figure 3.3f how the channel noise model strongly underestimated the measured current noise for untreated devices, meaning that for most of the U_{gs}-range contact noise is dominant. Conversely, for UVO-treated devices the contact noise model fully describes the experimental data as contact noise does not play a significant role. It should be noted that the I_{ds}^{rms} curve displays a V-shape when contact contributions prevail and changes towards the M-shape characteristic for channel noise as previously described. To explain the improvement of both the metal-graphene contact resistance and the resulting contact noise, a transition line model equivalent circuit has been proposed [14]. Augmented z-plane charge injection due to the removal of fabrication residues and defect creation during the UVO treatment would lead to current crowding at the contact edges, shortening the length of the graphene sheet under the contacts which the current passes through. Since contact noise is often associated with resistance fluctuations in channel material below the metal contacts [107], caused for example by traps in the underlying substrate, this would result in a decrease of total
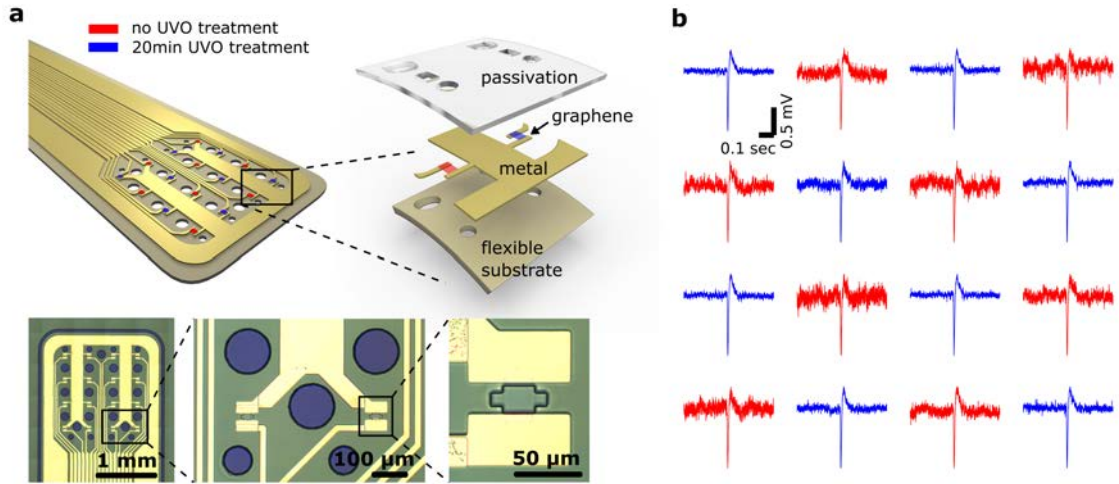
Figure 3.4: Performance-improved μECoG-array: a. Schematic and optical images of a flexible epicortical probe with 16 gSGFET sensors (20 μm x 20 μm channel area), with UVO-treated and non-treated sensors arranged in a chessboard layout. **b.** Map of a generated population spike event recorded by each transistor of the array. Adapted from [14].

noise. To assess the augmented performance resulting from the contact improvements in the final application, flexible probes with an equal number of UVO-treated and untreated gSGFETs in a chessboard arrangement have been studied (Figure 3.4a). Figure 3.4b shows the g_m-normalized recordings of an artificially generated hippocampal population spike. A clear increase of SNR can be seen across most UVO-treated sensors, which results from an over two-fold reduction of the rms noise level [14].

3.2.2 Channel noise

The previous section, discussed the impact of both contact and channel noise to the total flicker noise in gSGFETs. UV-ozone contact treatment has been presented as a reliable tool to lower the metal-graphene contact resistance and thus to reduce its noise contribution. In this way, it is possible to enter a regime where channel noise becomes dominant and sets the limit of the gSGFET's sensitivity. Naturally, as a further step towards ultra-low noise devices, efforts have to be undertaken to also lower the channel contribution to the flicker noise. The data discussed in this section is unpublished work and presents an intermediate state of technology improvements towards gSGFETs with reduced channel noise. As previously mentioned, channel noise in gSGFETs was found to be dominated by charge carrier fluctuations caused by trap states in the underlying substrate or surface contaminants [111]. Common strategies to protect the outstanding electrical properties of graphene from such negative influence include the engineering of free-standing channels [121] and the use of buffer materials in contact with the channel which allow for a decrease in the density of trap states in the channel vicinity. Popular materials for such an endeavour are high-quality dielectrics such as hexagonal boron nitride (hBN) [107, 122]. Self-assembled monolayers which turn the substrate sur-
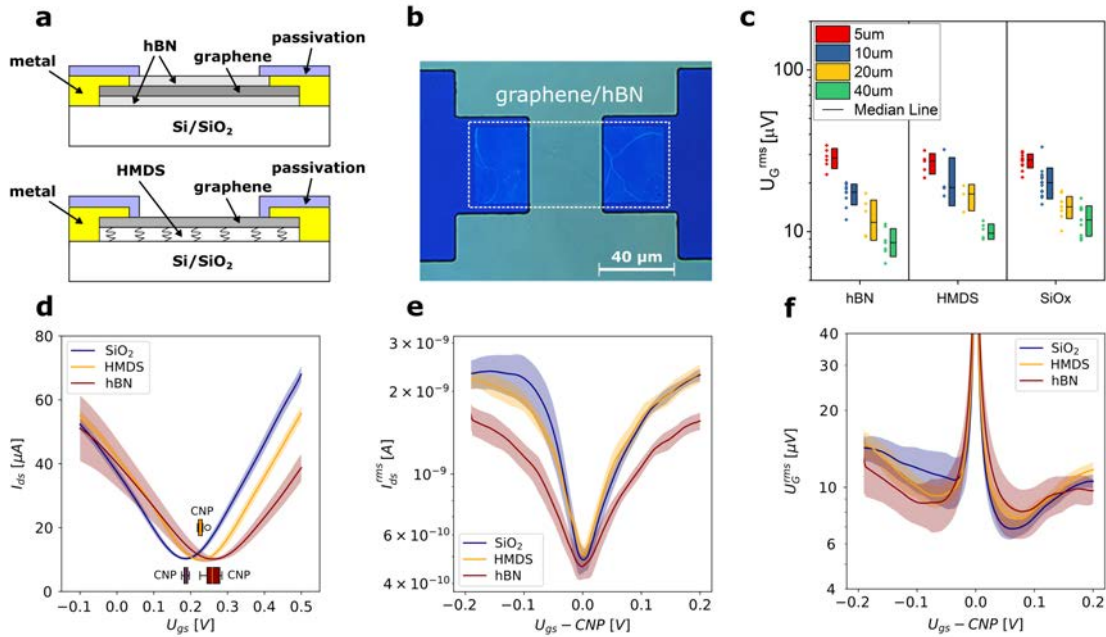
Figure 3.5: Reduction of channel noise in gSGFETs: a. Schematic of gSGFET cross-section for a graphene channel with hBN encapsulation and on top of a HMDS buffer layer. **b.** Optical image of graphene channel with underlying hBN layer. **c.** Effective gate noise for several channel lengths (5 μm, 10 μm, 20 μm and 40 μm) and constant channel width of 40 μm for a graphene channel either directly placed on the SiO_2 wafer, with an HMDS buffer layer or an hBN encapsulation. Average value and standard deviation of transfer curves for **d.** drain-source current I_{ds}, **e.** integrated current noise I_{ds}^{rms} and **f.** effective gate noise U_G^{rms} for an applied drain-source bias U_{ds} of 40 mV and device 40 μm x 40 μm channel size. All noise values are calculated for an integration range from 1 Hz to 100 Hz.

face hydrophobic, such as hexamethyldisilazane (HMDS), have also been suggested to allow screening of substrate deficiencies [123, 124, 125, 126]. hBN is an insulating two-dimensional material which can be obtained by either mechanical exfoliation or CVD growth. Due to its atomically flat surface and its minimal lattice mismatch with graphene it is a popular choice for encapsulation purposes and gate dielectrics in graphene FETs [127]. It is reported to improve the device's carrier mobility due to screening from dominant scattering sources such as charge impurities and surface phonons [122, 127, 107] and to reduce its flicker noise due to the lower density of impurities and trap sites in the hBN layer compared to thermal oxides [128].

Furthermore, surface adsorbates such as hydroxyl groups, which attach to either the silicon substrate or defects in the graphene surface, facilitate absorption of e.g. dipo-lar molecules, which in turn have been identified as a primary cause for non-uniform doping and hysteresis in graphene FETs [128]. Therefore, it has been suggested that a hydrophobic coating (e.g. HMDS) of the substrate before graphene transfer can prevent the attachment of such adsorbates, thus inhibiting degradation of the electric properties of the graphene FET. A threefold increase in carrier mobility has been linked to the successful screening of the graphene film as a result of such hydrophobic treatment [123]. Figure 3.5a shows the architecture of two alternative interface configurations explored in this thesis. For the case of hBN encapsulation,

CVD-grown multilayer hBN has been transferred pre and post graphene transfer to form a top and bottom encapsulation, in order to protect the channel from substrate defects as well as from the attachment of dipolar water absorbates from the contacting electrolyte (Figure 3.5b). Thorough surface cleaning with organic solvents and thermal treatments have been applied to remove organic residues from the multiple transfers and surface patterning techniques. For the case of the hydrophobic coating, the silicon wafers (with 285 nm thermal oxide layer) have been pre-treated in oxygen plasma to clean the surface and subsequently placed on a hot-plate (100°C) in an HMDS saturated atmosphere for several minutes. After this treatment, the graphene layer has been directly transferred onto the coated wafer, in order to minimize the exposure of the coated surface to the environment, considering the high volatility of the surface functionalization. The UVO contact treatment described in the previous section has been applied to all devices measured for this study, to ensure that contact noise is not the predominant flicker noise contribution. Figure 3.5c shows the effective gate noise U_G^{rms} at peak g_m of devices with varying length and for different interface engineering. While the HMDS-treated surface apparently did not significantly improve the noise performance compared to graphene directly placed on the SiO_2 substrate, the bilateral hBN encapsulation shows a positive impact on U_G^{rms}. The improvement is most clear for devices with long channels, suggesting that for short channels contact noise might still strongly contribute. Studying the bias-dependence of the integrated current noise (Figure 3.5e), it is notable that the M-shaped noise on silicon substrate, which is characteristic for noise dominated by the channel region, transforms into a V-shape which indicates a significant reduction of channel noise. Channel encapsulation is further expected to augment the charge carrier mobility in graphene FETs which in turn should result in higher transconductance. However, from the I_{ds}-U_{gs} transfer curve in Figure 3.5d, a small reduction of g_m is observed. This can be explained by the transconductance not only being proportional to the charge-carrier mobility but also the double-layer capacitance at the graphene-electrolyte interface, which is likely to decrease due to the thickness of the top hBN layer separating the ions from the channel. Thus the channel encapsulation with multilayer hBN decreases both sensitivity and intrinsic noise of the device, yet an overall positive effect on the SNR (U_G^{rms}) remains, as can be seen in Figure 3.5f. In contrast to the results reported in the literature, hBN encapsulation increased the amount and dispersion of p-type doping of the devices, compared to a plain silicon substrate (Figure 3.5d), which might indicate that either a large amount of organic residues from the transfer process remained between the stacked layers or that the CVD-grown multilayer hBN has a high density of defects.

These preliminary results suggest that hBN encapsulation is a promising strategy for channel noise mitigation to obtain ultra-low noise gSGFETs. Remaining challenges towards optimal results are further improvement of the fabrication procedure to provide a contamination-free stack of layers, as well as the scarcity of high-quality and large-area hBN synthesized by CVD growth. Also, the thickness of the top encapsulation layer has to be fine-tuned, ideally providing sufficient protection from water adsorbates and surface contamination without decreasing the double-layer capacitance and thereby the sensitivity of the sensor.

In this chapter, the gSGFET was introduced as a powerful tool for electrophysiology due to its sensitivity to ionic fluctuations in its surroundings, which result in a shift of Fermi level and thus in a change of measured current. Due to the small amplitude of neural activity, when measured from the cortical surface, large intrinsic noise remains the primary limitation in most neural sensor technologies. In the case of the gSGFET, the noise spectrum is dominated by low frequency noise originating in either the graphene-metal contacts or the graphene channel region. Noise which originates in the contact region is found to scale proportionally with the metal-graphene contact resistance. A treatment of the contacted graphene sheet with ultraviolet ozone prior to the metal deposition, is found to provide low contact resistance and thus improved noise levels. Noise which originates in the channel region, on the other hand, can be reduced by decoupling the graphene sheet from charge traps and impurities in the underlying substrate or surface residues. To this end, thin hBN layers show promising results as a buffer material to encapsulate the graphene channel, yet further efforts to improve the film quality and the fabrication of such layered channel structures have to be made to obtain optimal results.

Chapter 4

Multiplexed readout of sensor array

In this chapter, we describe in more detail the importance of multiplexed data readout to operate sensor arrays with large sensor count and how this has been implemented for the gSGFET technology. The concept of multiplexing, originally developed for telegraphy in the 1870s, allows simultaneous transmission of multiple messages through a single wire. Since then it has found application in telephony, video processing, broadcasting and in image sensors in cameras. In the case of neural interfaces, it allows to overcome the challenge of connecting an equal number of wires to each of numerous sensors due to the size restrictions of the array and the necessity to minimize the invasiveness of the implant. In the following, the fabrication and characterization of multiplexable μ-ECoGs of up to 1024 recording sites on a flexible substrate is described. Two alternative multiplexing methodologies, namely time-division and frequency-division multiplexing and their ability to provide artefact-free data readout of the sensor-array are explored. Application-specific benefits and drawbacks of each concept are assessed and the technology's potential to map electrophysiological activity in-vivo is presented. This chapter is largely based on the articles presented in A.2 and B.1.

4.1 Fabrication of multiplexable sensor array
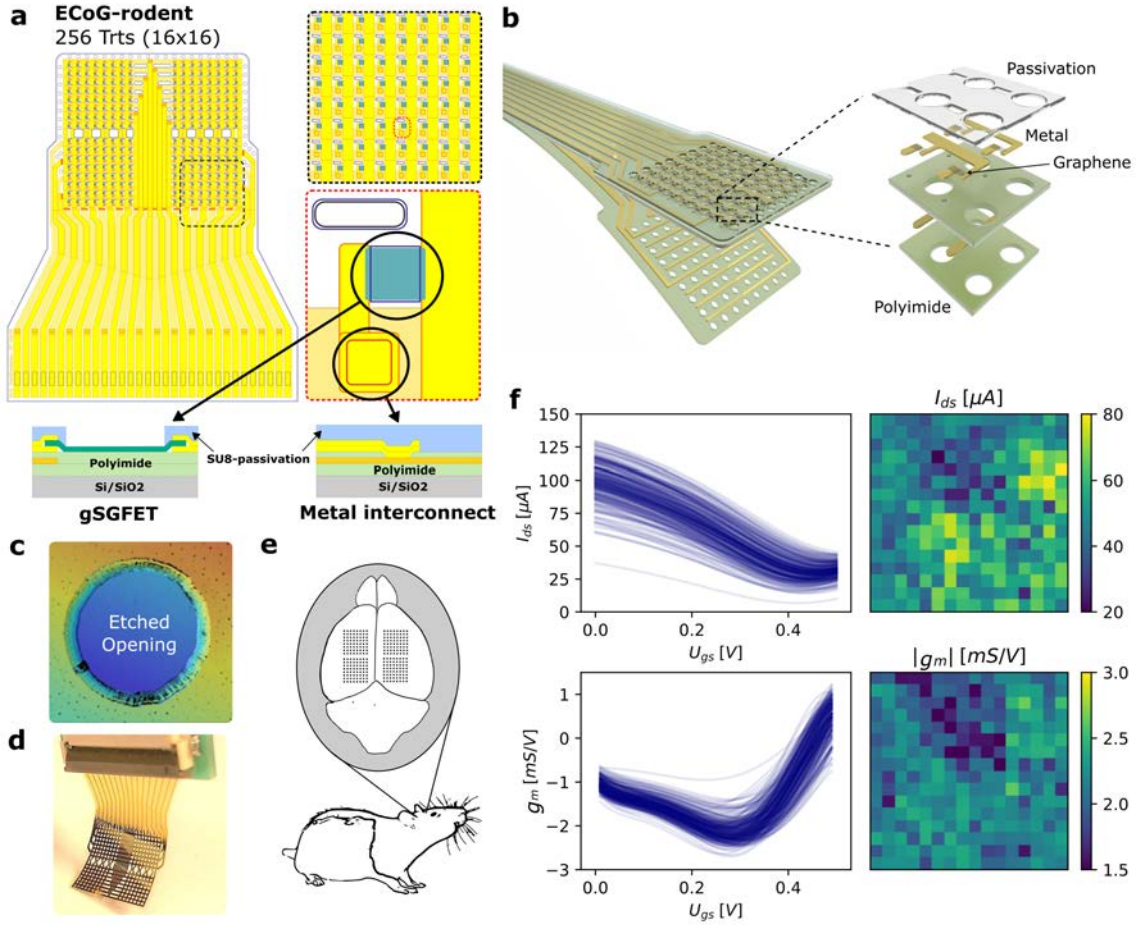
Figure 4.1: Design, fabrication and characterization of multiplexable μECoG-array: **a.** Schematics of the 16x16 ECoG array for rodents. **b.** Illustration of the 8x8 ECoG array for rodents (64 gSGFETs). **c.** Tapered profile of polyimide via-hole to interconnect the metal layers. **d.** Optical image of an ECoG probe for rodents with a 16x16 sensor array (256 gSGFETs). **e.** Illustration of Long Evans animal model with the outline of the implanted gSGFET 16x16 ECoG array covering both cortical hemispheres. **f.** Gate bias-dependence of I_{ds} and g_m as well as the respective distribution of each value at peak-g_m across all recording sites.

The multiplexable μ-ECoGs are fabricated by scalable thin-film technology on 7 μm-thick flexible polyimide (PI) using 4-inch silicon support wafers [11]. An illustration and the layout of a μ-ECoG array, as well as its placement on the animal's cortex can be seen in Figure 4.1a,b,e and consists of a stack of two metal layers constructing the perpendicular lines of the sensor grid with a separating PI layer in between. To bridge the PI layer where metal interconnections have to be made, via-holes with a smooth, tapered profile need to be etched into the PI-layer (Figure 4.1c). The gSGFET sensors have single-layer graphene channels of 100 μm x 100 μm dimension and inter-site separation of 500 μm. A more detailed description of the probe fabrication can be found in Appendix C.1. A picture of the final probe, after releasing it from the Si support wafer is shown in Figure 4.1d. Figure 4.1f

shows the characterization of an array of gSGFETs with regard to its performance and homogeneity. The transfer curve is presented as an averaged value and for all 256 individual devices. Also, the corresponding transconductance g_m is shown as a function of the applied gate bias. The distribution of each parameter (I_{ds}, g_m) across the array, calculated at the bias point of highest absolute transconductance (peak-g_m), is shown in the corresponding color maps (Figure 4.1f). The high yield on a 4-inch wafer and evenly distributed sensor performance across all recording sites show the high maturity and homogeneity of the gSGFET technology, and are key requirements to enable multiplexed addressing schemes.

In Figure 4.2 the next generations of such time-division multiplexed μECoG-arrays can be seen, incorporating a total of up to 1024 gSGFETs for a chronic implantation in either rodents or minipigs. These next generation probes are designed to be controlled by an application specific integrated circuit (ASIC), since operating such a large number of sensors with discrete electronics becomes increasingly challenging as they are for example more prone to pick up noise and show slower response times under switching.
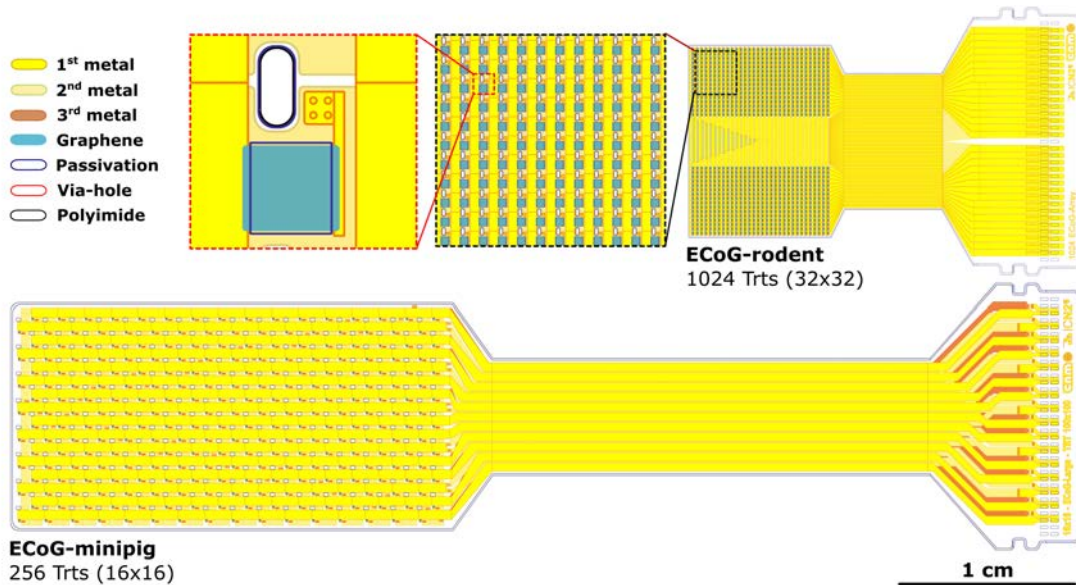
Figure 4.2: Next generation of μECoG-array with 1024 gSGFET: Schematics of the ASIC-compatible future generations of the 32x32 ECoG for rodents (1024 gSGFETs) and the 16x16 ECoG for implantation in minipigs.

4.2 Multiplexing methodologies

Generally, there are various ways to perform multiplexing and we have explored two of the most common implementations, namely time-division multiplexing (TDM) and frequency-division multiplexing (FDM). Figure 4.3 shows the different operating principles of both, which manifest in the way they divide signals from different
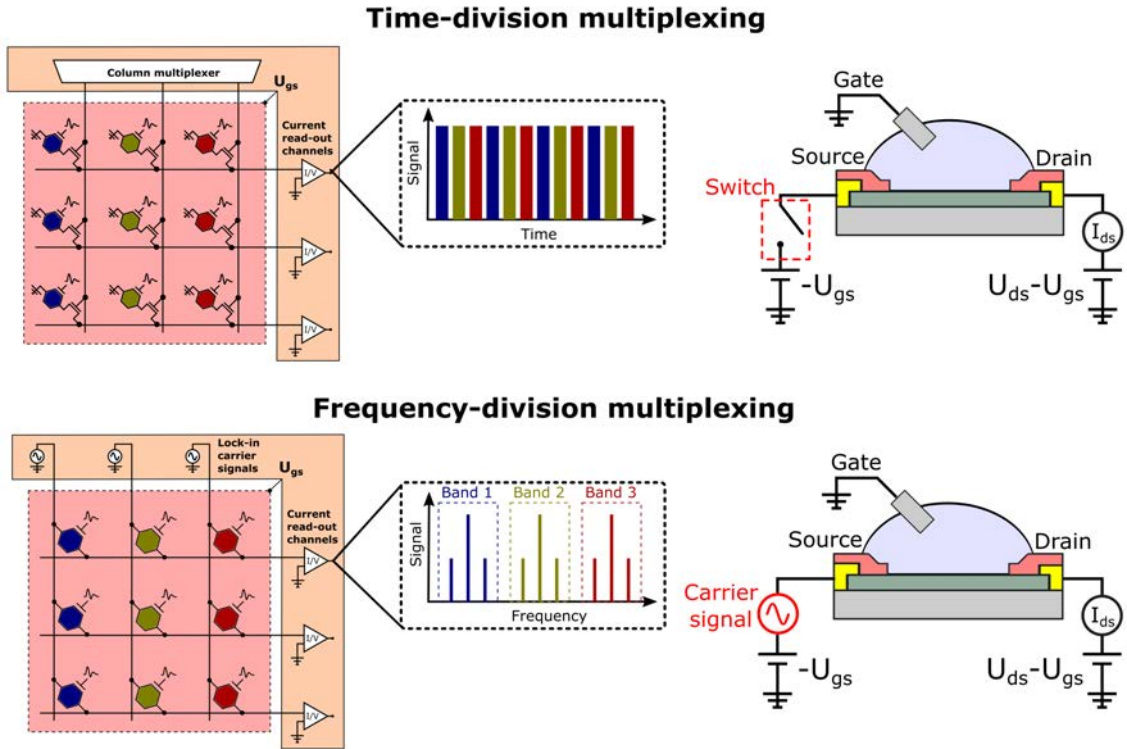
Figure 4.3: Multiplexing methodologies: Transport of information from different recording sites (blue, green, red) through a shared wire can, for example, be realized by dividing the signals into distinct time windows, namely time-division multiplexing (TDM), or into distinct frequency windows, namely frequency-division multiplexing (FDM).

sensors within one row of the array into either distinct time or frequency windows. The circuit diagrams illustrate each method implemented for the operation of an array of gSGFET sensors. In the case of TDM, the selective addressing of recording sites is achieved by switches which are placed directly at each sensor and controlled through a column multiplexer. The recorded signal at each row is then passed to a corresponding transimpedance amplifier, amplifying and converting the signal from current into voltage. FDM, by contrast, does not require the embedding of switches into the array, but utilizes carrier waves with frequencies varying between columns to project the sensor recordings into discrete, non-overlapping frequency bands through a process called amplitude modulation [129]. By subsequent filtering and demodulation, the original waveform can be recovered. Table 4.1 shows an overview of the characteristics of both multiplexing schemes when operating in large μ-ECoG arrays of gSGFET sensors. In the following paragraphs, these characteristics will be elaborated in more detail.

4.2.1 Time-division multiplexing

As previously mentioned, time-division multiplexing (TDM) refers to a technique of sequentially addressing the columns of a sensor array while continuously measuring from its rows, or vice versa. Typically, this functionality is achieved by placing

	TDM	FDM
scalability restriction	transient response	available bandwidth
limitation in signal amplification	gSGFET mismatch	carrier wave overlap
noise	amplifier noise scales with number of rows	insensitive to amplifier noise
power consumption	one column	all sensors
sampling rate	medium (1-3 kHz)	high (> 10 kHz)
cross-talk	scales with R_{track} (can be mitigated by integration of on-site switches)	scales with R_{track} (cannot be mitigated)
signal artefacts	inter-symbol interference	lock-in phase jitter
electrical coupling	DC	DC or AC

Table 4.1: Overview of multiplexing schemes: Characteristics of time-division multiplexing (TDM) and frequency-division multiplexing (FDM) regarding scalability, signal quality and bias supply.

switches directly on the array as shown in Figure 4.3. This bears the advantage that it allows to address one selected column or row while using high impedance elements to cut connections with all other sites on the array. Thus integrating the switching technology directly into the sensor array prevents inter-site cross-talk, which is a consequence of current passing through non-addressed paths within the array and thereby contaminating the recorded signal [130, 12, 65]. However, switching devices that can be integrated with flexible technologies are scarce and complex to fabricate [12]. Alternatively, externally placed switches can also yield good results, if certain circuit design rules are considered [66, 22]. Combining arrays of passive sensing elements (i.e. electrodes) with an external addressing configuration is challenging, since the electrode's recorded voltage signal is prone to pick up noise; if the pre-amplifier is placed far from the electrode, additional buffer transistors are required to convert the signal into current and feed it to the read-out circuitry [12]. The use of active sensing elements (i.e. transistors) offers a great benefit here, since they feature an intrinsic voltage-to-current conversion, making the recorded signal more robust to noise. In the following, the compatibility of the gSGFET with such an external addressing configuration is tested. This requires the development of read-out electronics and processing software to operate the gSGFET array, as well as to assess the quality of the recordings obtained in multiplexed operation compared to standard operation. In a further step, limiting factors are explored which set limitations to achievable array sizes operated by this concept and the

level of crosstalk is quantified.

Implementation of TDM scheme

A schematic representation of the addressing and acquisition methodology is shown in Figure 4.4c. For this purpose, a custom-build PCB board consisting of two main functional blocks has been developed using discrete electronics. One functional block performs the filtering and amplification of the simultaneously acquired AC and DC signals; the other block selects the row to which the bias difference is applied, using an external switching matrix for addressing. Figure 4.4a illustrates the acquired AC and DC raw input signals for a column of eight gSGFETs and how they can subsequently be used to reconstruct the original signal at each site (Figure 4.4b). Resistance mismatch between different transistors leads to current jumps when switching between devices, which results in the different DC levels in the acquired signal (each gSGFET corresponds to one color in Figure 4.4a). The vertical dashed grey line in Figure 4.4a indicates the point at which all eight rows were addressed and a new readout cycle begins. At each site a total of 10 points is taken at 100 kHz sampling speed; we discard the first 5 to avoid any switching artefacts and average the rest to a single data point resulting in 1.25 kHz effective sampling rate. It should be here emphasized that array homogeneity carries an additional importance in multiplexed operation owing to two reasons. First, the trade-off between applicable AC signal gain and transistor resistance mismatch; as previously mentioned, current jumps can exceed the dynamic range of the amplifier (indicated in Figure 4.4a) leading to saturation and signal loss. Second, the switching artefacts scale with the level of mismatch between devices, requiring longer stabilization times before reliable data points can be collected. Figure 4.4d shows the recording of a 16x16 μECoG-array operated in TDM mode using the previously described operating scheme. The gSGFET sensor transduces brain activity patterns into current signals, which subsequently have to be recalibrated by dividing by the device specific transconductance value in order to obtain the original signal amplitude in voltage. Compared to electrodes which directly record activity in voltage, this recalibration procedure is more prone to error. Bias point drifts during long recording periods and a non-constant frequency-dependence of the transconductance make it difficult to accurately recalibrate all spectral components of the signal. To quantify the signal variation resulting from this recalibration error, signals of different frequencies (0.3 Hz, 1.25 Hz and 12.5 Hz) have been applied to the sensor array in a PBS solution. Ideally, the recalibrated signal measured for each sensor of the array should have an identical amplitude. Yet, as can be seen in the histograms in Figure 4.4e there is a variation of measured amplitude across sensors which increases with the frequency of the signal and results from the assumption of a frequency-independent g_m. Typically, g_m is directly extracted from the I_{ds}-U_{gs} transfer curve, which is obtained by giving the device sufficient time to reach a steady state after each bias change. Naturally, this results in highest accuracy for slow oscillations and in an increasing calibration error for higher frequencies. Alternatively, the Bode plot, which measures the transconductance as a function of the signal frequency which is applied to
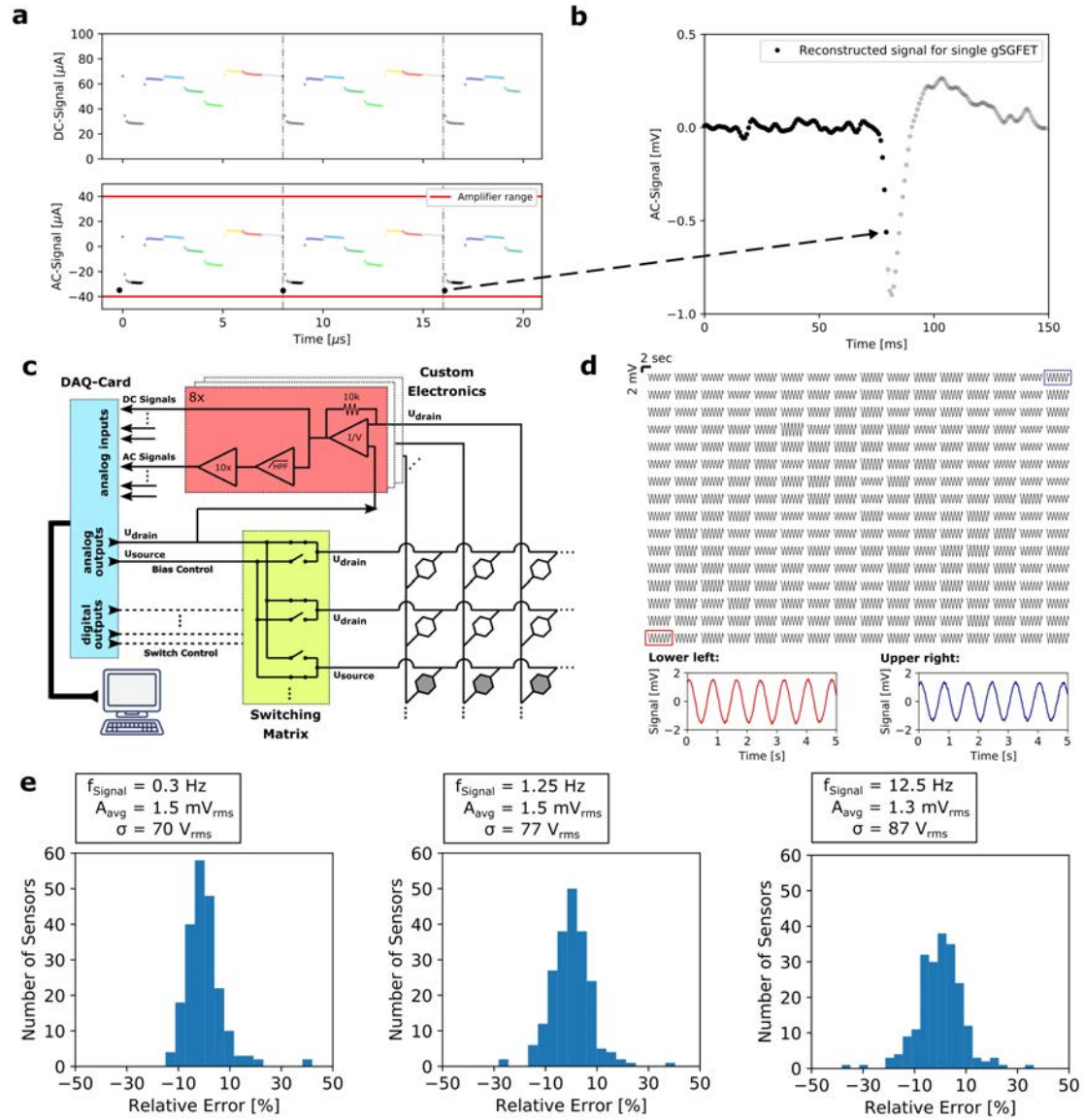
Figure 4.4: Implementation of TDM acquisition mode: a. Acquired DC and AC raw signal for one column showing eight distinct current levels corresponding to the transistors in each row, which repeat for every cycle (grey dashed line). Due to the high gain (100k) applied to the AC component of the signal, the dynamic amplifier range sets a limit to the allowable current mismatch between devices, before amplifier saturation occurs (solid red line). **b.** From the 10 data points taken for each transistor per cycle, an average value of the last 5 points is taken, to yield one sample in the final reconstructed signal for each sensor. **c.** Schematic of discrete multiplexing setup using a DAQ-card for bias control and read-out (blue) and a custom-build PCB board for switching (yellow), filtering and current-to-voltage conversion (red). **d.** g_m-normalized recording of a sinusoidal test signal at each sensor on a 16x16 μECoG-array with two enlarged recordings of the sensors on the lower left and upper right corners of the array. **e.** Statistical distributions of measured root-mean-square amplitudes across all sensors on the array shown in part a. The histogram, average value and standard deviation are shown for sinusoidal test signals of frequencies 0.3 Hz, 1.25 Hz and 12.5 Hz. Adapted from [15].

the gate, could be used to determine g_m for each frequency band. This would result in a more accurate calibration [131].

Scalability

With the goal of creating a high-density, large-scale sensor array, an important question is the scalability of the technology, meaning how easily it can be used to obtain a large number of recording sites. In the case of TDM, the most important aspects to consider are the transient response of the transistor, which limits the maximum switching speed, and the increase of inter-site cross-talk with array size and track resistance [130, 61, 66]. To obtain distortion-free, high-quality recordings in multiplexed operation, it is important to allow sufficient stabilization time after switching for the transistor to adjust to the changed drain-source bias conditions. This stabilization time is device-specific and generally scales with channel length and carrier mobility. With its record high charge carrier mobilities, which can potentially reach up to $350\,000$ $\text{cm}^2\text{V}^{-1}\text{s}^{-1}$ in ideal conditions [4] and for our devices are in the range of $1000\text{-}2000$ $\text{cm}^2\text{V}^{-1}\text{s}^{-1}$, graphene is especially suited to high-speed applications compared to other technologies based on silicon (carrier mobility of 1400 $\text{cm}^2\text{V}^{-1}\text{s}^{-1}$) or conducting polymers such as PEDOT:PSS (carrier mobility of 0.01 $\text{cm}^2\text{V}^{-1}\text{s}^{-1}$).

The transient response of the gSGFET under switching can be seen in Figure 4.5a. The on-state is reached below 1 μs, which is the time resolution of the used measurement equipment (NI DAQ-Card X-Series 6363). Such fast device stabilization could eventually allow switching speeds beyond 1 MHz, sufficient to operate even large sensor arrays while maintaining a sampling rate adequate to resolving even high frequency activity such as spikes. Yet, additional limitations from the read-out electronics (e.g. stabilization of transimpedance amplifier) may prevent reaching this fundamental limit of the gSGFET. To avoid that the acquisition interval corresponding to one sensor on the array interferes with subsequent acquisition intervals of neighbouring sensors, which is known as inter-symbol interference, it is mandatory to maintain a guard interval after switching and before collecting any data [132]. The required length of this interval, which depends on both the performance of the sensor and the electronics, ultimately limits the achievable sampling rate and presents a drawback of TDM compared to FDM operation. However, replacing the discrete circuitry with an application specific integrated circuit (ASIC) would allow improving the performance of the amplifiers and thereby increasing the sampling rate.

To confirm that rapid switching in the multiplexed operating mode does not affect the fidelity of the gSGFET recordings, the recording quality must be compared to the one obtained in steady, non-multiplexed operation. Figure 4.5f and g compare recordings of an artificially generated electrocardiogram signal (ME-W-SG, Multichannel Systems), containing components of different frequencies. The multiplexed and non-multiplexed representation of both test signals and their respective root-mean-square (rms) amplitude are nearly identical, suggesting that the rapid sequential addressing by the multiplexed mode does not generate any visible artefacts or introduce significantly augmented noise, neither in the low- nor in the mid-frequency
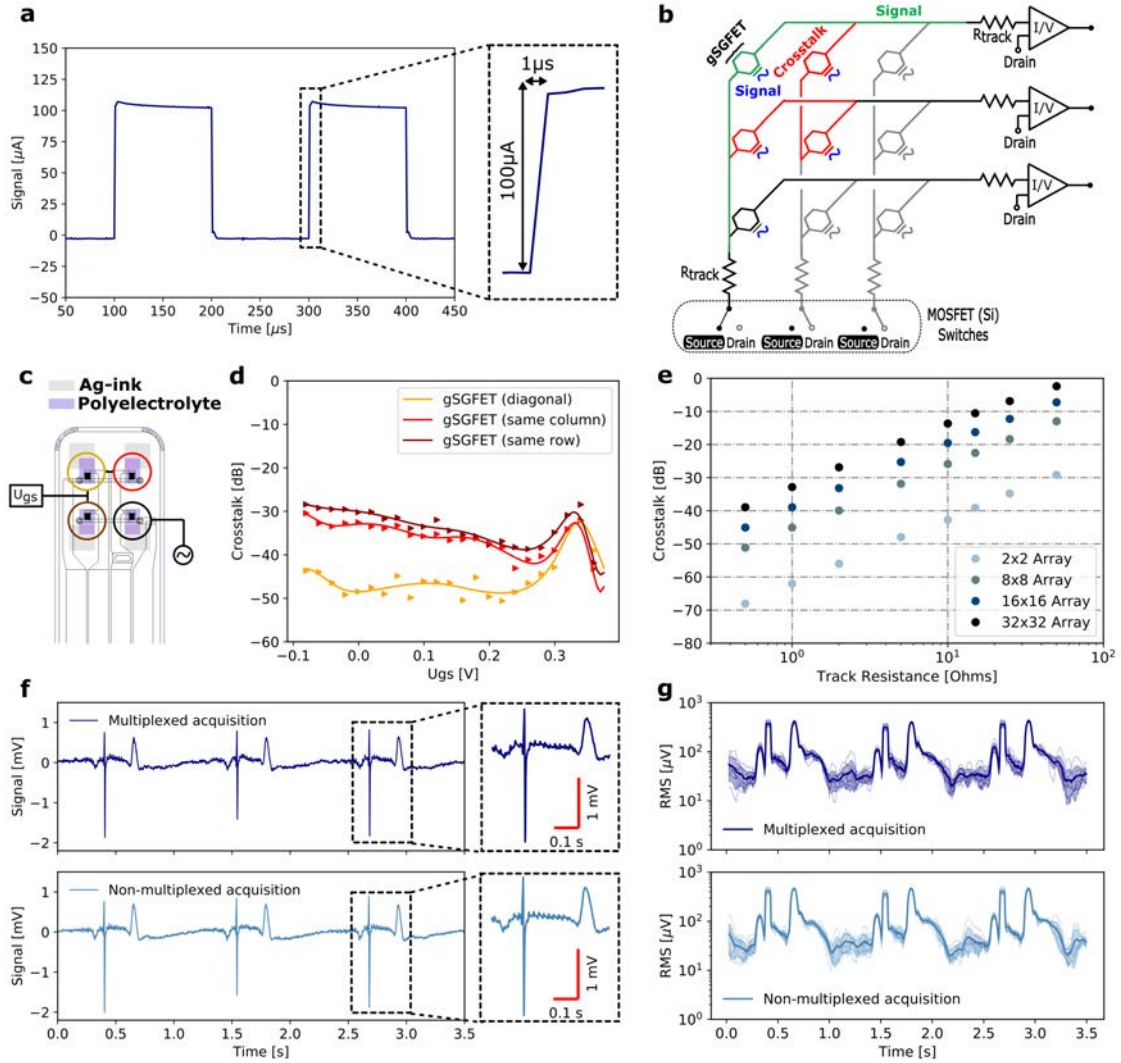
Figure 4.5: In-vitro validation and scalability of TDM: a. Transient response of gSGFET when switched between On and Off state, showing the short stabilization time of the device. **b.** Origin of cross-talk in an array without on-site switches and finite track resistance. Biasing to U_{drain} of non-addressed columns significantly decreases the amount of cross-talk. **c.** Location of measured gSGFETs on a 2x2 probe for crosstalk evaluation, utilizing inkjet printing to pattern confined gates consisting of Ag and polyelectrolyte pads. **d.** Crosstalk versus gate bias when applying a test signal (sinewave 30mV, 10Hz) to a single gSGFET and measuring the signal on each of the adjacent sensors. The devices in the same column and row as the one, to which the test signal is applied to, show a crosstalk of -40dB while the device on the diagonal shows crosstalk lower than -50dB (below floor noise of electronics). **e.** Simulated (PSpice) cross-talk for 2x2, 8x8, 16x16 and 32x32 arrays depending on the track resistance. The aggregated cross-talk value is presented assuming a superposition of identical signals on all but the probed sensor. **f.** Recordings of one gSGFET on the μECoG-array, acquired in either multiplexed or steady (non-multiplexed) acquisition. An artificial electrocardiogram signal was used to compare the fidelity of both acquisition modes. **g.** For each acquisition mode, the root-mean-square (RMS) value is calculated as the mean value of all 8 gSGFETs on one column, indicating the signal-to-noise ratio of the recorded signal. Adapted from [15].

49

band.

As previously stated, the use of external switches bears the disadvantage of not allowing to cut the connections to non-addressed sensors within the array, which leads to the so-called cross-talk. The lack of on-site switches opens alternative current pathways from adjacent sites which carry signals from the respective gates of those sites and are wrongly attributed to the addressed sensor (see Figure 4.5b). Such cross-talk can be strongly reduced, and in the ideal case of vanishing track resistance even fully suppressed, by setting the bias point of the non-addressed rows to the same voltage as the data lines (lines which connect each row of the array to the transimpedance amplifier). This biasing scheme prevents any current flow through non-addressed lines [66]. However, in real-world applications, the issue of finite track resistance cannot be completely avoided, as the requirements of high sensor density and probe flexibility limit the allowed width and thickness of the metal lines. The presence of these additional resistances creates local potential drops between nodes of the array, driving current through otherwise suppressed pathways whose amplitude depends on the ratio between track resistance (R_{track}) and transistor resistance (R_{gSGFET}); it also depends on the number n of columns and rows in the array.

To quantify crosstalk in the gSGFET array experimentally, lateral Ag-gates and confined pads of solid polyelectrolyte were placed at each gSGFET of a 2x2 array by means of inkjet printing (Figure 4.5c). This approach allows for selective gate control, which is not possible in a shared liquid electrolyte. Figure 4.5d shows the measured signal at each of the transistors, with a test signal (sine wave of 10Hz frequency and 30mV amplitude) only being applied to one of them (black circle in Figure 4.5c. Sensors on the same column (red curve in Figure 4.5d) or row (dark-red curve in Figure 4.5d as the applied signal are the ones with the largest impact of crosstalk, showing a crosstalk level of -40dB at peak transconductance compared to the signal amplitude. Diagonally placed sensors (orange curve in Figure 4.5d) are much less affected; however, in the latter case the exact level of crosstalk cannot be extracted with accuracy because the signal lies below the floor noise of the electronics.

To validate this estimation of the cross-talk, we have compared the experimental data with the results obtained from a PSpice simulation of a gSGFET array in which we have used a standard p-type MOSFET element tailored to fit the gSGFET's transfer curve [15]. Figure 4.5e shows the aggregated cross-talk on a single site depending on the track resistance and the array size, assuming the worst-case scenario of having identical signals on all remaining sites of the array which sum up to the total cross-talk value. The PSpice model validates the expected near-linear relation with both track resistance and array size. Extrapolating to an array of size 32x32 (1024 sensors), a cross-talk lower than -20 dB could be maintained by reducing the track resistance below 5 Ω or by increasing the resistance of the gSGFET. Such track resistance reduction could be achieved by increasing metal track thickness, using higher number of stacked metal layers and, most importantly, relaxing constraints on probe dimensions (e.g. neural probes for large animals or humans). As an alternative to a reduction of physical cross-talk, a correction scheme has been proposed, which would allow estimation of the level of crosstalk beforehand and later

subtraction from the actual recordings [16]. This scheme, however, would require accurate determination of the values of R_{track} and R_{gSGFET} for each specific sensor design.

Since such applications also require more elaborate and miniaturized readout circuitry which can be directly mounted on a head-stage, the readout electronics previously build from discrete components have been integrated (in the frame of the European project BrainCom) into an application specific integrated circuit (ASIC) (Figure 4.6), with the additional benefit of reducing circuit size, energy consumption and pick-up noise. In addition, the ASIC can digitize the recorded signals before transmitting them through wires to the external acquisition platform, avoiding contamination by pick-up noise and motion artefacts. The validation of the ASIC operation is not part of this thesis, although its design has been largely based on the knowledge developed around this work.
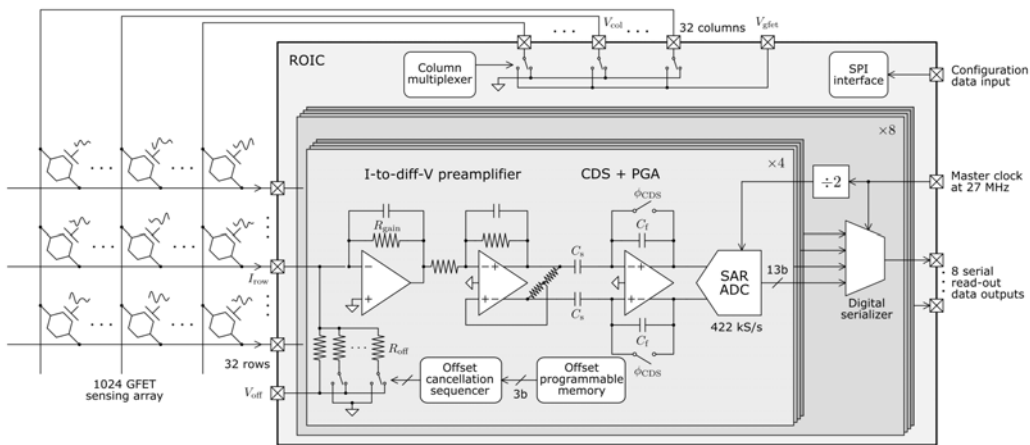
Figure 4.6: ASIC design: Implementation of the time-division multiplexing methodology into an application specific circuit (ASIC) design, capable of simultaneous reading out 1024 sensors. This design is part of the European project BrainCom. Credits for the figure and the ASIC development belongs to Jose A. Cisneros Fernandez and Francesc Serra Graells from the Institute of Microelectronics of Barcelona (IMB-CNM).

4.2.2 Frequency-division multiplexing

While TDM is certainly the more natural approach to address a sensor matrix, FDM offers an intriguing alternative due to several distinct advantages it has in regard to the gSGFET's operation in μECoG-arrays. As described in Section 3.1, the regular mode of the gSGFET requires a constant DC bias to be applied across its channel, driving a conductance-dependent current, which itself changes with the applied gate bias (i.e. the neural activity). Alternatively, a pure tone oscillation can be used to drive the drain-source current through the channel. A signal of frequency f_s applied to the gate electrode, would then undergo spectral folding with the carrier wave frequency f_c, yielding two new tones with frequencies $f_c - f_s$ and $f_c + f_s$. This concept is known as amplitude modulation (AM) and is graphically

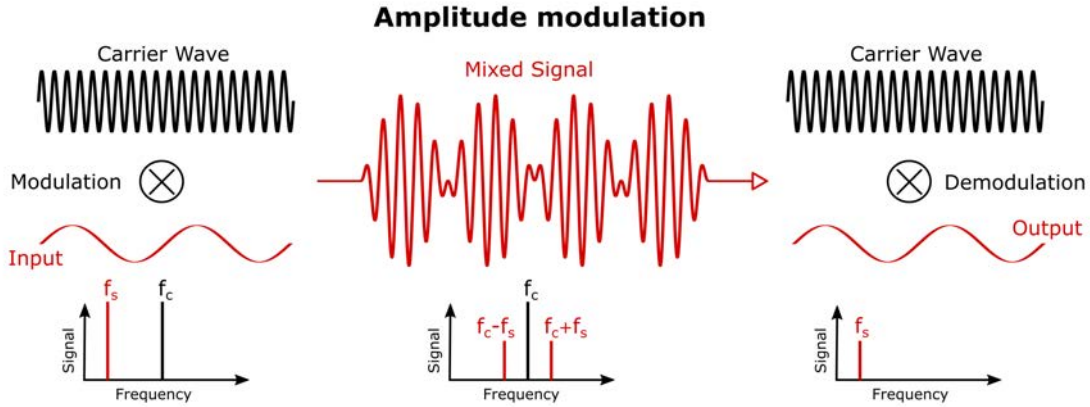**Figure 4.7: Amplitude modulation:** Amplitude modulation, which forms the basis of FDM, mixes a signal (frequency f_s) with the carrier wave (frequency f_c), resulting in the emergence of two new super-posed waveforms with frequency components f_c-f_s and f_c+f_s. The composite signal can subsequently be demodulated by re-mixing it with the original carrier wave.

explained in Figure 4.7. The theoretical equation can be expressed by a first order Taylor expansion (see Appendix C.2 for the derivation) in the applied bias by the carrier wave.

$$I_{ds}(t) \approx \frac{A_C}{R^0_{gSGFET}} \sin(2\pi f_c t) + \frac{g_m^{norm} A_C A_S}{2} \left(\sin(2\pi(f_c + f_s)t) + \sin(2\pi(f_c - f_s)t) \right)$$

A_C and A_S being the carrier and signal amplitude and R^0_{gSGFET}, g_m^{norm} the gSGFET's resistance and normalized transconductance at the respective bias point. To ensure, that this mode of operation does not alter the gSGFET's performance as a sensor, the device's transconductance and equivalent gate noise in AM mode can be compared to the DC mode (see Appendix B.1). Only minor changes in the gate dependence of U_G^{rms} were observed, which have been tentatively explained by a non-homogeneous effective gating along the channel in AM mode. [16]

Scalability

Regarding the scalability of FDM operation for increasingly large number of transistors, there are several factors to consider. The susceptibility to cross-talk of FDM is equivalent to the one described for TDM using external switches. However, while TDM allows for an eventual integration of the switches within the array, and thus reducing cross-talk, such a strategy is not feasible for FDM. Further limitations of FDM arise from the required bandwidth separation between different carrier waves, which is mandatory to prevent signal contamination from higher harmonics of neighbouring devices. In addition, there is an upper limit for the carrier wave frequency that the gSGFET can handle. At very high frequencies, the graphene-electrolyte capacitive interface becomes permeable to leakage current, causing a parallel parasitic current flow along the channel which eventually can reduce the transconductance and thus sensitivity of the device [133, 16]. The frequency at which this phenomenon becomes relevant depends on the length of the device, and has been observed at 600

kHz for a 50 μm channel length (see Appendix B.1). The AM scheme could be enhanced by the use of quadrature AM, which would allow fitting twice the number of carriers into the available frequency band [134].

Another constraint regarding scalability of FDM is the quantization error of the analog-to-digital converter, which describes the error made by translating an analog signal of continuous amplitude into a digital signal with a limited number of possible discrete values. This error can be minimized by increasing the bit resolution of the digitizer, however, this comes at the expense of limited bandwidth for the input signal and reduced sampling rate. Another factor to consider regarding the quantization error is the dynamic range of the analog-to-digital converter, which sets a limit to the largest detectable amplitude of the input signal. The step-size of the quantization levels can be derived by dividing the dynamic range by the number of quantization values (bit resolution). An increasing number of carriers in FDM operation results in a larger input amplitude due to constructive interference, which in turn requires a larger dynamic range and thus increases the quantization error. This effect can be reduced by choosing an optimal set of phase shifts between carrier waves, thereby minimizing the resulting maximal amplitude from their constructive interference (see Appendix B.1).

One important benefit of FDM is that the continuous acquisition of the modulated signal allows a much higher sampling rate than what is possible with TDM, where switching artefacts require extended stabilization periods. Also, the lock-in operation of AM shifts signals to a higher frequency band, permitting the removal of low-frequency circuit noise from electronic components. Oscillator phase noise is a potential source of artefacts in FDM-mode and can result in lock-in phase jitter [135]. Comparing both multiplexing schemes, there are two further important considerations to address regarding a future technology translation towards applications in humans. Here, regulatory aspects regarding heat dissipation, power consumption and risk of tissue damage caused by technology malfunction pose stringent constraints on circuit and device design. When using TDM combined with integrated flexible switching technology, current is passed solely through a single column, reducing both power consumption and heat dissipation during operation compared to FDM-mode. Yet, the latter permits to operate the sensor array by AC electric coupling using capacitive elements to transmit the pure-tone carrier waves. This concept could be enhanced by high impedance elements which would prevent high leakage currents, thus limiting any potential damage of the brain tissue in the case of device failure. TDM operates with continuous DC bias supply, which is not compatible with such a concept.

4.3 Electrophysiological application

4.3.1 High-resolution mapping of wide-bandwidth brain activity

Increasing the bandwidth of neural interfaces in terms of spatial resolution and sensitivity in a wide range of frequencies is a major and ongoing challenge in neural
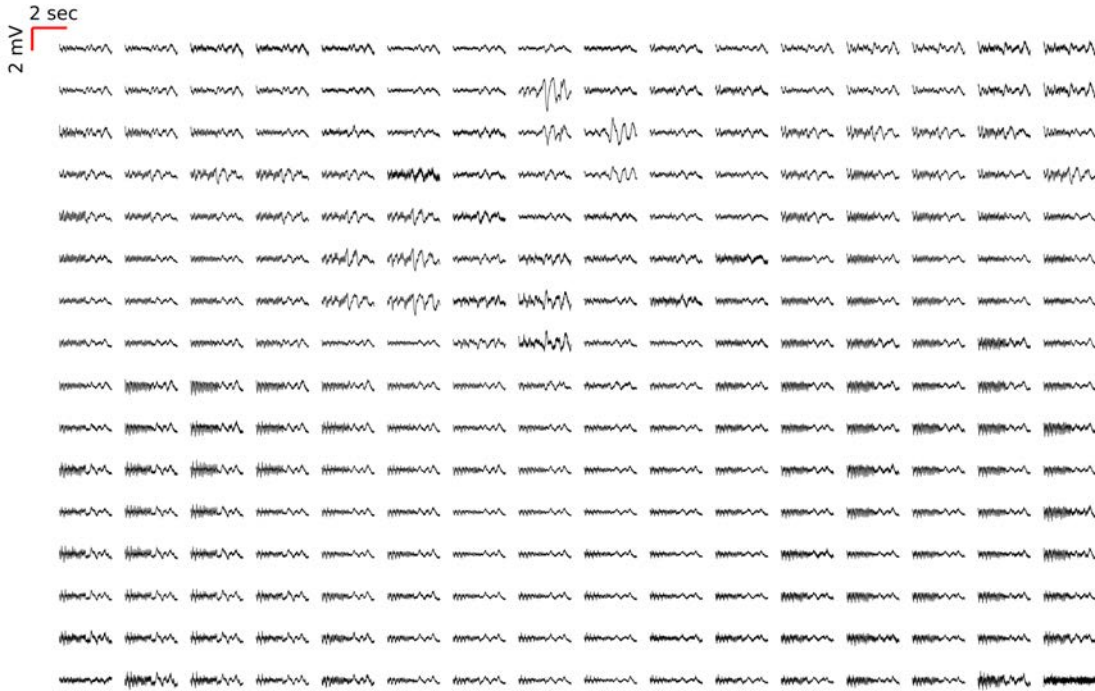
Figure 4.8: Cortical map of spontaneous activity with multiplexed gSGFET arrays: Topology of spontaneous local-field potentials recorded with 256 sensors across both cortical hemispheres.

engineering. Electrocortiography is primarily used to record local field potentials (LFPs) from the surface of the brain, which originate from spatio-temporal summation of transmembrane currents generated by synaptic and active conductances, excluding the action potentials [136, 137]. The characteristic spectral content of the LFP signal reflects the time scale of network synchronization and ranges from below one Hertz to few hundreds of Hertz. Figure 4.8 shows a time trace of spontaneous LFP activity in an awake Long Evans rat, recorded in a chronic in-vivo experiment using an 16x16 array of gSGFETs operated in the multiplexed mode. Visually evoked LFP activity exhibits a well-defined spatial topography; thus, in the frame of this thesis, it has been used for validating the mapping capabilities of the multiplexed gSGFET technology [138]. A topological dependence of the recorded signal shape can be observed, with a visible symmetry between left (sensors on the left) and right hemisphere (sensors on the right). Figure 4.9a shows the averaged response and respective standard deviation over 10 consecutive evoked events, recorded with a multiplexed array of gSGFETs in an anaesthetized Long Evans rat. Visually evoked activity typically exhibits a clear response with a delay of 40 ms after both the on- and off-switching of the stimulus. The recordings show a main peak (on response) lasting until 70 ms after the stimulation with a peak amplitude of 500 μV. Hence, signal shape and amplitude are in good agreement with previous results in non-multiplexed gSGFETs [11]. Further, the corresponding maps (Figure 4.9b) present the spatial distribution of both amplitude and time-delay of the on-peak. The earliest response is detected on the lower end of the array (boxed region
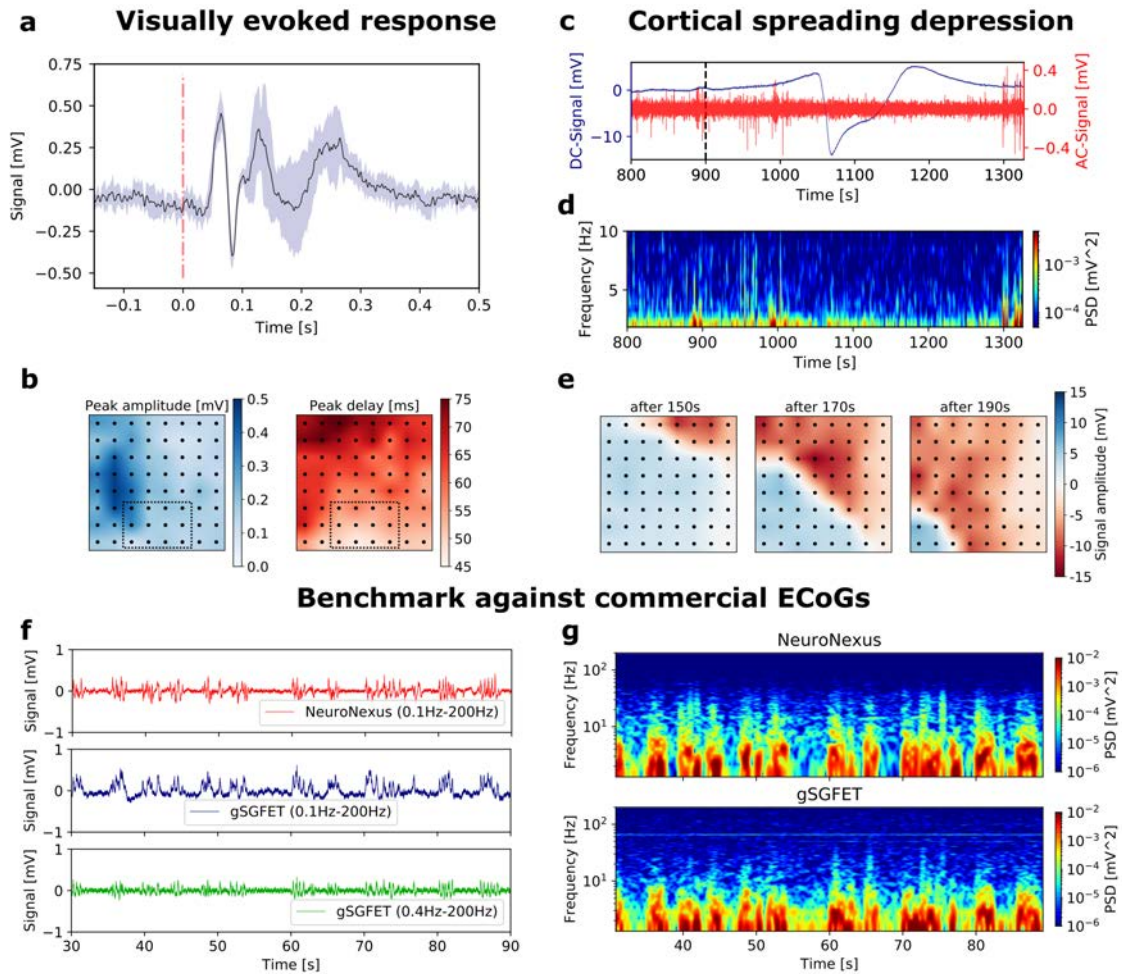
a **Visually evoked response**

c **Cortical spreading depression**

b

e

Benchmark against commercial ECoGs

f

g

Figure 4.9: Wide-bandwidth brain recordings with multiplexed gSGFET arrays: a.
Averaged visually evoked activity with an on- and off-response of 50 ms delay and 500 μV peak
amplitude. **b.** Array maps displaying the distribution of amplitude and time-delay of the on-peak
response across all sites. While the shortest delay is measured for the sensors placed directly
on the primary visual cortex, the highest peak-amplitude is seen in the secondary visual cortex.
c. DC-signal (blue, lowpass-filtered below 20 Hz) and AC signal (red, bandpass-filtered between
1-20 Hz) during an induced cortical spreading depression (CSD) event. A strong DC shift of -
15 mV occurs together with a silencing of high-frequency activity, which is characteristic for a
CSD. **d.** Corresponding spectrogram of CSD event to validate the silencing. **e.** Array map
showing the propagating front of the spreading depolarization wave across the array from the
right upper to the left lower corner. **f.** Recording trace derived from an AC-coupled passive
ECoG-array (NeuroNexus, platinum electrode) as well as DC and AC-filtered gSGFETs. Note
prominent infraslow oscillations (0.1- 0.4Hz), which are not visible in the AC electrode recordings.
g. Corresponding spectrograms of both, NeuroNexus and gSGFET recordings. This figure is
adapted from [15].

in Figure 4.9b) which represents sensors directly placed on the primary visual cor-
tex where the activity originates, and then spreads radially towards higher visual
cortical areas. However, the highest peak-amplitude is measured in the centre-left
region (secondary visual cortex) which likely reflects a different magnitude and prox-
imity current dipole, that gives rise to the surface LFP [139]. In addition, to their

capability to record LFPs, the gSGFETs exhibit a unique sensitivity for slow and infra-slow (below 0.1 Hz) signals, which in the case of passive electrode recordings are hidden by baseline drifts and the impedance-related loss of gain at low frequency [60]. In order to confirm that multiplexed acquisition preserves signal quality in this frequency band, we have investigated recordings of a cortical spreading depression (CSD). CSDs emerge due to a cellular depolarization of neurons and astrocytes which is clinically associated with brain injury and migraines among other causes [140]. Here, the CSD was artificially triggered by injecting KCl into the cortex, which caused a slowly propagating wave moving across the cortex [60]. Figure 4.9c depicts the recording of a gSGFET in the array during a CSD event. The DC component of the signal (blue curve) shows the characteristic large shift of 15 mV amplitude. The AC component (red curve) reveals a silencing of the high-frequency activity during the event, caused by the cellular depolarization, which is character-istic for CSDs [141]. The silencing of high-frequency activity can also be seen in the corresponding spectrogram (Figure 4.9d). The maps in Figure 4.9e show the cor-responding position of the depolarising wave at different times after KCl injection, moving from the top right to the bottom left at a speed of about 7 mm per minute. To benchmark the recording capabilities of the gSGFET array against other state-of-the-art technologies, a NeuroNexus ECoG array (with 32 circular platinum elec-trodes of 100 μm diameter) was simultaneously placed on the opposite hemisphere. Figure 4.9f shows recordings from an electrode and a gSGFET, displaying the ex-pected synchronicity in activity of both hemispheres. Filtering the signals from 0.1 Hz to 200 Hz (dark-blue and red curve in Figure 4.9f), a clear difference in signal shape can be noticed. This difference reflects the high-pass filter of the AC-coupled head-stage used for passive ECoG recordings, which is necessary to prevent amplifier saturation due to drifts; also the high impedance of passive ECoG electrodes at low frequency leads to reduced gain in such signals, which results in an attenuation of the infra-slow frequency content in the LFP signal [60]. Removing these low-frequency components from the gSGFET signal (green curve in Figure 4.9f), it is possible to validate that both technologies show very similar recordings of the LFP activity as can also be seen in the corresponding spectrograms (Figure 4.9g).

4.3.2   Brain-state classification in chronic recordings

Having confirmed the ability of the multiplexed gSGFET sensor to record brain signals during acute implantation in section 4.3.1, the next step is to validate the recording stability of a chronically implanted probe in an awake animal. In case this technology proves suitable to acquire stable recordings of high quality during extended implantation times, this would make the gSGFET an interesting platform to e.g. study neural activity during behavioural events or to classify brain states. Initially dismissed as noise or artefacts, spatio-temporal correlations of spontaneous infra-slow activity (ISA) have recently attracted increased attention in behavioural neuroscience [142], as ISA was found to play an important role in resting-state network dynamics [143, 144, 145, 146] and brain states [144, 147, 148]. Yet, its neu-rophysiological basis remains widely unknown [142, 149]. The use of a high-density
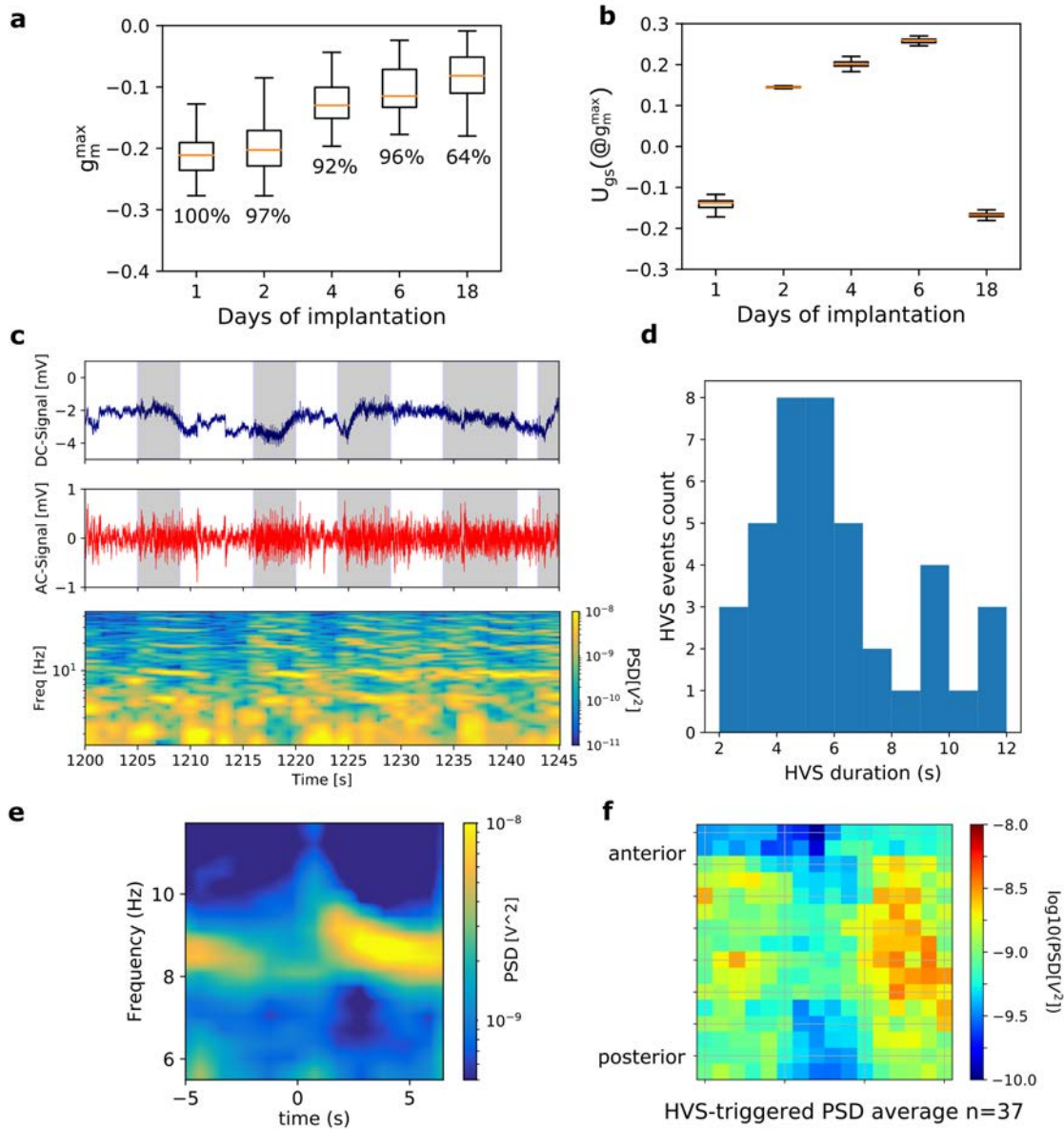
Figure 4.10: Chronic recordings with multiplexed gSGFET arrays: a. Mean value and standard distribution of the measured peak transconductance of a probe with 256 gSGFETs throughout the period of implantation. The percentage of working sensors on the probe is noted for each day of recording. **b.** Evolution of mean value and standard distribution of the bias point of peak transconductance over the course of the implantation. **c.** DC component (blue curve) and AC component (red curve, high-pass filtered above 1 Hz) of the chronic recording with the corresponding spectrogram. **d.** Distribution of event duration across the recorded HVS events. **e.** Averaged spectrogram triggered at the onset of 37 individual HVS events. **f.** Cortical mapping of the spectral power in the most expressed frequency band between 7 and 10 Hz.

μ-ECoG array offers here an interesting alternative to currently used techniques such as functional magnetic resonance imaging (f-MRI) as it offers high spatial resolution and sensitivity to neural oscillations across a wide frequency band. To assess the suitability of the gSGFET technology to map brain states during chronic recordings,

we have explored high-voltage spindles (HVS), which typically occur in rodents during the brain state of waking immobility [150] and show a relatively large amplitude. For this purpose, a multiplexed gSGFET μ-ECoG array with 256 recording sites, as shown in Figure 4.1a, was placed across both cortical hemispheres of a Long Evans rat. During the recordings, the animal was freely moving within a restricted arena, with the read-out system connected to the probe by coaxial wires, which shield the recordings from pick-up noise. Epicortical recordings of several hours were acquired over 18 days while the animal was moving freely. First, to assess the stability of operating conditions of the gSGFETs, the measured peak transconductance and the bias point at which it is obtained is displayed over the course of the implantation in Figure 4.10a and b. These parameters need to be monitored as shape and position of the I_{ds}-U_{gs} transfer curve might change during the implantation. A slow degradation of the absolute value of the peak transconductance over the duration of the recording is observed and is presumably a consequence of a combination of factors. Mainly, gradual absorption of surface residues present in the environment can affect the electronic properties of the graphene film by lowering the interfacial capacitance between graphene and the electrolyte or by limiting the carrier mobility in the graphene sheet, which both results in an overall decrease of transconductance. Charged species in such adsorbates can also affect the doping of the gSGFET which results in a shift of the transfer characteristics and thereby the bias point at which the device has its largest transconductance. A shift of transfer characteristics can also be caused by electrochemical reactions at the reference electrode. The percentage of working devices on the probe are also added to Figure 4.10a and remains very high (above 90%) during the first week of implantation. Due to the lack of sufficient statistics, however, and the fact that much less degradation has been previously observed for non-multiplexed gSGFET probes chronically implanted over a month and longer, this preliminary data does not allow any clear conclusions on the stability of the multiplexed technology and further experiments will be conducted in the near future.

Next, the capability of the gSGFET's to allow brain state classification by e.g. detecting HVS events during chronic recordings is explored. Figure 4.10c shows a time trace of the DC component (blue line) and the AC component (red line, filtered above 1 Hz) with the grey shaded region indicating periods during which HVS activity occurs. The corresponding spectrogram in Figure 4.10c shows an increase in high frequency activity during the events; the histogram in Figure 4.10d shows the distribution of event duration, with the most frequent length being around 5 seconds. To investigate for recurring patterns during HVS activity, Figure 4.10e shows the averaged spectrograms triggered at the onset of 37 individual events identifying prominent spectral components in the 7-10 Hz band. Taking advantage of the large number of sensors on the probe, Figure 4.10f shows in which cortical regions this spectral component is most expressed by mapping the averaged power distribution at this peak oscillation frequency. Interestingly, a symmetric distribution across the cortex can be seen with a slightly higher power on the right hemisphere. These preliminary results only provide a glimpse of the technologz capabilities for chronic brain state classification; more detailed studies are currently ongoing.

To summarize this chapter, the gSGFET technology carries great potential for the realization of large-scale neural interfaces with large sensor count, due to the unrivaled electronic properties of graphene and the gSGFET's characteristics as an active sensor. Next to the technology's conformability and it's sensitivity to brain activity across a wide frequency range, these findings present an essential cornerstone when assessing the gSGFET potential to contribute to the development of novel brain machine interfaces which surpass today's state-of-the-art. The technology's maturity as well as its compatibility with large-scale processing techniques and flexible substrates enables the fabrication of conformable sensor arrays of 1000 sensors and more with high yield and good homogeneity. The recordings obtained with either the FDM or the TDM read-out scheme are comparable to the recordings in steady operation, without significant increase in noise or artefacts from the multiplexed operation degrading the signal quality. Both multiplexing approaches present equally interesting alternatives, however, TDM might be better suited to operate μ-ECOG arrays of very high sensor count due to scalability benefits and FDM might be better suited for the operation of depth probes, which require much higher sampling rates to detect action potentials. Crosstalk remains the main hurdle as it equally affects both multiplexing approaches and increases with array size, which makes it an important factor when assessing the achievable sensor count. Replacing the discrete electronics used for this proof-of-concept validation by a tailor-built ASIC will eventually allow to test the fundamental limits of the technologies. Recordings from the cortex of both anaesthetized and awake rodents confirm the ability of the multiplexed gSGFET sensor array to detect brain activity of broad frequency range. The large sensor count and high sensor density enable a detailed mapping of electrophysiological activity patterns of the cortex.

Chapter 5

Sensor array with monolitically integrated switching matrix

Using external switches to multiplex the sensor array, greatly facilitates device fabrication, but poses restrictions on the achievable sensor count, due to the already discussed increase of inter-site cross-talk, which scales with the track resistance and the number of both columns and rows of the array. Due to long cable connections in chronic recordings and size limitations during implantation, it is virtually impossible to completely avoid track resistance and, hence, it is inevitable that with increasing array size cross-talk will eventually start to compromise the recording fidelity. Fortunately, this can be overcome by the incorporation of flexible switches directly on the array, which act as high-impedance elements serially connected to each non-addressed sensor. The feasibility of such a complex monolithic integration on flexible substrates has already been shown using ultra-thin thermally-grown silicon technology in combination with platinum electrodes [12, 63, 64] and organic electronic materials [65]. In the following, we explore the suitability of the MoS$_2$-FET as a flexible switching device for a monolithic integration with the gSGFET sensor technology. Combining both technologies would enable flexible μ-ECoG arrays which are compatible with TDM operation, yet more robust to inter-site cross-talk and would thus pave the way for a further increase of sensor count.
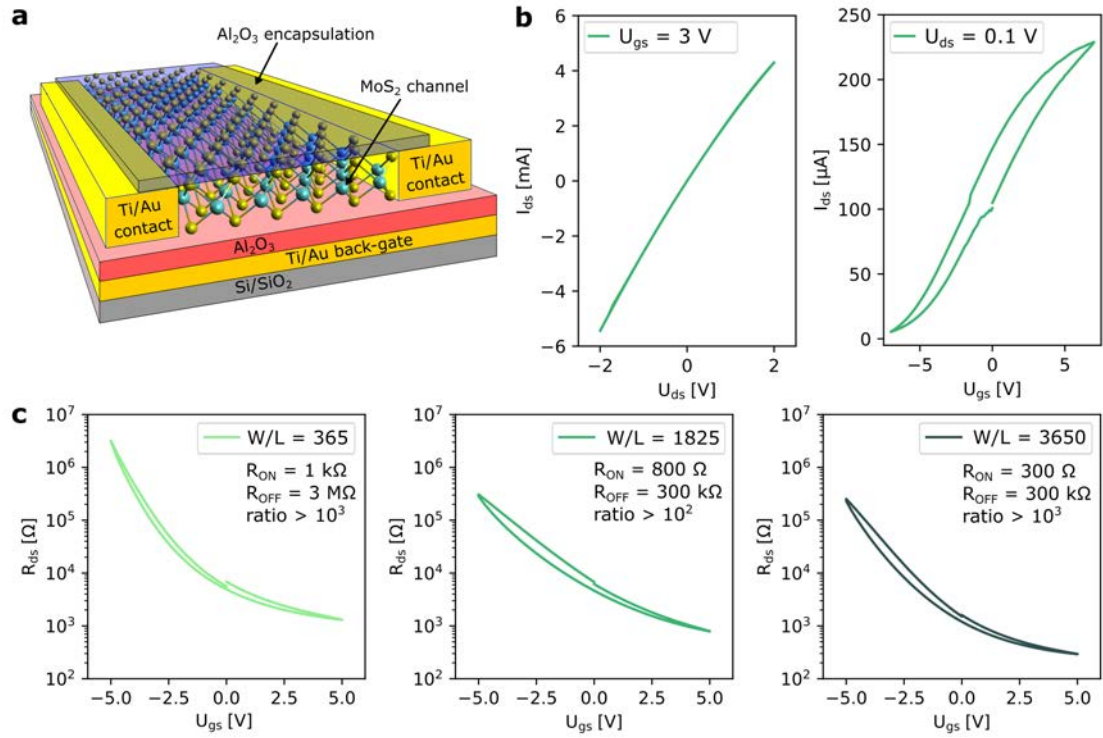
5.1   Molybdenum disulfide field-effect transistor

Figure 5.1: Electrical properties of MoS$_2$-FET: **a.** Schematic of MoS$_2$-FET device layout. **b.** Typical I$_{ds}$-U$_{ds}$ and I$_{ds}$-U$_{gs}$ transfer curves of MoS$_2$-FETs on a rigid silicon chip. **c.** Change of channel resistance R_{ds} with applied backgate voltage U_{gs} for devices designed with different levels of interdigitation, that describes an interlinked finger-like channel design which allows to obtain a large width-to-length ratio while maintaining a squared channel footprint. Devices of low (width-to-length ratio of 365), medium (width-to-length ratio of 1825) and high (width-to-length ratio of 3650) interdigitation are compared.

As mentioned in chapter 2, semiconducting TMDCs such as MoS$_2$ show great properties for application in flexible digital circuits due to their two-dimensional structure, their direct band-gap [151], and their relatively high carrier mobility values [152]. One of the most common applications of MoS$_2$ are field-effect-transistors, which take advantage of the semiconducting nature of the material to switch between a state of high and a state of low conductivity by control of the applied gate bias. Recently it has been shown that the MoS$_2$-FET technology has reached a level of maturity which enables the design of logic circuits and even the realization of simple microprocessors [92]. The wide conductivity range of the MoS$_2$-FET, combined with its mechanical conformability and fast frequency response, also suggest the suitability of the device to create addressing circuitry to multiplex flexible sensor arrays.
The architecture of the MoS$_2$-FET devices, which have been fabricated for this purpose, is shown in Figure 5.1a. It consists of a Ti/ Au/ Al$_2$O$_3$ back-gate [153] onto which a MoS$_2$ monolayer is transferred and patterned. In general, either a back-gate or top-gate architecture can be used to shift the Fermi level and thus control the conductivity of the channel. However, as the atomic layer deposition (ALD) of

ultra-thin, high quality oxide layers on top of the MoS_2 film is challenging [154], the back-gated transistor architecture provides a simpler approach for a first proof-of-concept integration with the gSGFET technology. Next, the MoS_2 monolayer is contacted by metal terminals at either end. As previously discussed, creating high quality interfaces for efficient charge injection between 3-dimensional metal contacts and 2-dimensional materials remains challenging because of e.g. the presence of surface adsorbates. The lack of short-channel effects and near ballistic charge carrier transport in 2D materials often leave the contacts as the predominant cause of power dissipation. Titanium-gold (Ti/Au) metal pads have been used in our technology to contact the MoS_2 film, as they provide relatively decent contact resistance due to the matching work functions of Ti and MoS_2 [155]. However, indium-gold contacts [156] and a stack of MoS_2, etched graphene and nickel [157] have been reported to show even better results with contact resistance values of $3\,k\Omega\mu m$ and $200\,\Omega\mu m$ respectively. Ultimately, the device is encapsulated by an additional Al_2O_3 layer, to prevent oxidation of the MoS_2 in the ambient atmosphere, which would otherwise degrade the electrical properties [92]. Both the back-gate oxide and the encapsulation layer are deposited by ALD, however, the second layer requires the use of a seeding layer to facilitate the formation of nucleation centres on MoS_2. The fabrication of the MoS_2-FET devices is described in more detail in Appendix C.1.

Typical I_{ds}-U_{ds} and I_{ds}-U_{gs} transfer characteristics of a MoS_2-FET are shown in Figure 5.1b. The change of drain-source current I_{ds} with applied gate voltage U_{gs} shows a near linear behaviour and reaches a saturation regime for large bias values, with the pinch-off voltage lying around 6 V. Using the MoS_2-FET as a switch, it should ideally be operated in the saturation regime, as the lowest on-resistance can be obtained here and it remains relatively stable under minor changes of effective gate voltage. Yet, the observed hysteresis under a forward-backward sweep also increases notably with the size of the bias window. To work as an efficient switch, the on-resistance of the MoS_2-FET should lie at least one order of magnitude below, and its off-resistance at least one order of magnitude above the resistance of the gSGFET sensor (around $2\,k\Omega$ at peak transconductance). This would ensure no hampering of the gSGFET's sensing capabilities and still mostly remove inter-site cross-talk. As the estimated field-effect mobility of MoS_2 on silicon substrate lies around 1-10 $cm^2V^{-1}s^{-1}$ and thereby several order of magnitude below the one measured in graphene, the MoS_2-FET channel geometry has to have a very large width-to-length ratio to provide a sufficiently low on-resistance. A common technique to achieve large width-to-length ratios (W/L-ratio) while maintaining a squared device footprint, is to use interdigitated contacts by patterning interlinked finger-like metal structures as illustrated in Figure 5.2a. To identify the optimal level of interdigitation, MoS_2-FETs with W/L-ratio of 365, 1825 and 3650 have been fabricated and characterized. Figure 5.1c shows the change of the device's resistance with applied gate bias for each geometry. Of the three measured W/L-ratios shown, the one with the highest level of interdigitation (W/L = 3650) presents the most suitable values for on- and off-resistance values, complying with our criteria.

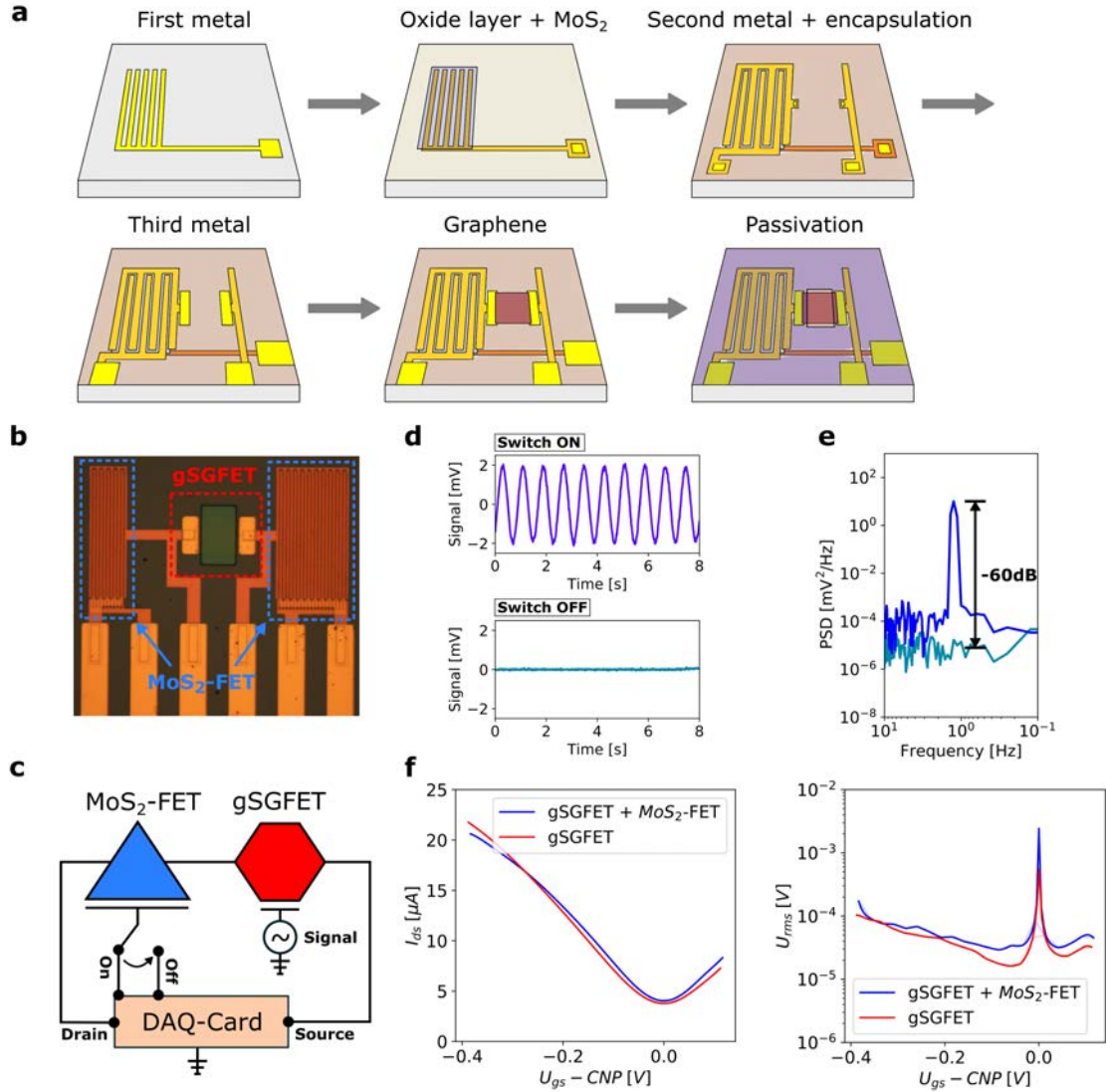## 5.2 Monolithically integrated MoS$_2$-FET/ gSGFET sensor technology

Figure 5.2: Monolithically integrated MoS$_2$-FET/ gSGFET sensor technology: **a.** Schematic of process flow to assemble the sensor technology by integrating the gSGFET sensors onto the MoS$_2$-FET switchable matrix. **b.** Optical image of a gSGFET sensor (red) serially connected to two MoS$_2$-FET switches (blue), one of medium and one of high interdigitation. **c.** Circuit diagram of the experimental setup. **d.** Sinusoidal test-signal recorded with the gSGFET with the connected MoS$_2$-FET either switched on (U_{BG} = +4V) or off (U_{BG} = -4V). **e.** Power spectral density (PSD) comparing the power of signal and crosstalk. **f.** I_{ds}-Ugs and U_{rms}-Ugs transfer curves, comparing the performance of the gSGFET sensor alone and of a serial connection with a MoS$_2$-FET in on-state (U_{BG} = +4V).

Having identified the optimal MoS$_2$-FET design, the next step is to monolithically integrate the MoS$_2$-FET with the gSGFET technology to form an array of hybrid sensors. This integration has the goal to obtain an equivalent addressing
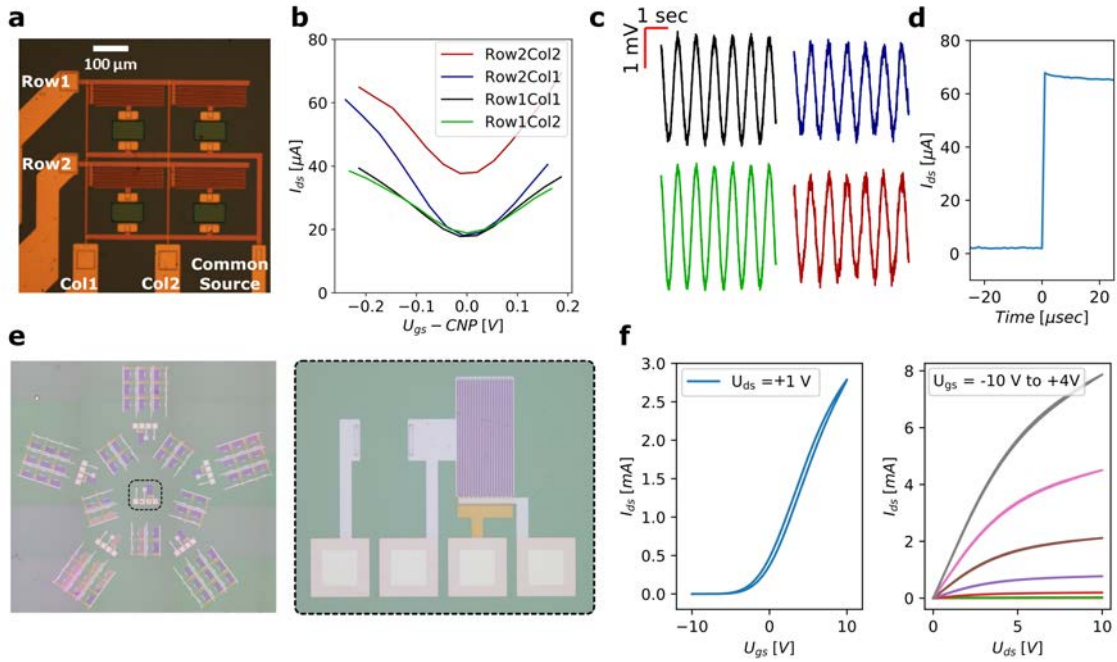
Figure 5.3: Multiplexed operation of integrated MoS$_2$-FET/ gSGFET sensor and translation to flexible substrate: **a.** Optical image of a 2x2 array of hybrid sensors on silicon substrate. **b.** Transfer curve of each gSGFET on the array. **c.** Recordings of a sinusoidal test signal measured at each site of the array in multiplexed operation with an effective sampling rate of 2.5 kHz. **d.** Transient response of the combined MoS$_2$-FET/ gSGFET sensor when switched from off- to on-state. **e.** Optical images of partially processed hybrid arrays on flexible polyimide substrate and a magnified image of a single sensor. **f.** I$_{ds}$-U$_{gs}$ transfer curve for U$_{ds}$ = +1 V and I$_{ds}$-U$_{ds}$ transfer curves for U$_{gs}$ ranging from -10 V to +4 V in steps of 2 V, for a MoS$_2$-FET fabricated on the flexible polyimide substrate.

functionality as for the external MOSFET switches in section 4.2.1, yet preventing the inter-site crosstalk which resulted from current flow through neighbouring recording sites. To achieve this goal it is important, that the MoS$_2$-FET switches are directly placed next to the gSGFET sensors on the array to prevent current from passing through non-addressed recording sites and thus produce crosstalk. Figures 5.2a-b show a scheme of the monolithic fabrication of both technologies and an optical image of such a device fabricated on a rigid Si/ SiO$_2$ substrate. The MoS$_2$-FET and the gSGFET are each fabricated following the respective process as described in Appendix C.1. To interlink both technologies, via-holes are etched into the encapsulation layer of the MoS$_2$-FET after initial completion, through which later the connections to the gSGFETs are made. As the serial arrangement of the two devices requires the resulting current signal of each gSGFET to also pass through the adjacent MoS$_2$-FET, transfer curves and flicker-noise of the combined technology can potentially be limited by the MoS$_2$-FET. Therefore, it is important to compare the sensing capabilities of the hybrid sensor (with MoS$_2$-FET in on-state) to the ones of the gSGFET alone. Figure 5.2c shows the circuit schematic of a hybrid sensor, and Figure 5.2f the I$_{ds}$-U$_{gs}$ and U$_{rms}$-U$_{gs}$ transfer curves for the gSGFET alone and serially connected to the MoS$_2$-FET. It can be seen that in its on-state, the MoS$_2$-FET barely has any influence on the transfer curve of the gSGFET and

that the effective gate noise U_{rms} is only slightly increased at peak g_m (blue line in Figure 5.2f), compared to the one measured for the gSGFET alone (red line in Figure 5.2f). Also, the measured amplitude of a sinusoidal test signal applied to the gate of the gSGFET is shown for the cases of the MoS_2-FET switched on (+4V) and switched off (-4V) (Figure 5.2d). While in the first case the signal is clearly visible, in the latter case it is strongly suppressed. This becomes more clear when comparing the power spectral density of both cases which indicates a cross-talk suppression by more than -60dB (Figure 5.2e). This proof of concept of a serial connection to a MoS_2-FETs switch allows effectively addressing distinct gSGFETs on a sensor-array without significantly hampering their recording sensitivity, while strongly suppressing inter-site cross-talk. In a next step, we aim to assess the ability of the hybrid technology under dynamic operation of time-division multiplexed readout. To this end, a small array of 2x2 hybrid cells (Figure 5.3a) is run in multiplexed operation, with an identical sinusoidal test signal of 1.25 Hz frequency and 1.5 mV_{rms} amplitude applied to each sensor through a shared electrolyte. Figure 5.3b depicts the measured transfer curves of each hybrid sensor and the signals recorded at each site in TDM mode. Each sensor was operated at 2.5 kHz sampling rate, clearly resolving the test signal. Yet, the recorded signals and the transfer curves of the measured array show some variances, making further technology improvements necessary to achieve similar results as for TDM with external switches. The transient response of the hybrid sensor under switching is shown in Figure 5.3d and is comparable to the one presented for external MOSFET switches in section 4.2.1 for both off-to-on and on-to-off transitions. This suggests that the integrated MoS_2-FETs do support rapid switching to achieve high sampling rates, even for large sensor arrays. Having validated the suitability of the hybrid technology as multiplexed sensor arrays on rigid silicon chips, the next steps towards their in-vivo application is the transfer of the technology to flexible substrates and a scale-up of the sensor count. Figure 5.3e shows optical images of partially processed arrays and a single hybrid sensor on flexible polyimide substrate. Figure 5.3f shows the I_{ds}-U_{gs} and I_{ds}-U_{ds} transfer curves of one of the MoS_2-FET on polyimide substrate. The field-effect mobility lies around 0.5 $cm^2V^{-1}s^{-1}$ and is significantly reduced compared to the one measured on silicon substrate. Yet, the transfer characteristics remain suitable for the application of the MoS_2-FET as a switch, showing a sufficiently large on/off-ratio of 10^5.

In this chapter, the suitability of two-dimensional TMDCs, such as MoS_2, for the implementation of digital circuits on flexible substrates has been shown. More specifically, the MoS_2-FET's large on-/ off-ratio of over five orders of magnitude, a rapid time response under switching and the device compatibility with conformable substrates make it an interesting device to provide a monolithically integrated addressing functionality for multiplexed gSGFET sensor arrays. A fabrication procedure for vertical integration of both technologies has been proposed and its translation to flexible substrates is ongoing. The resistance of the MoS_2-FET was tailored by adjusting the level of channel interdigitation to allow unaltered transfer characteristics of the combined MoS_2-FET/ gSGFET sensor, while providing a significant reduction of inter-site crosstalk. Further, does the combined device not show in-

creased noise characteristics and its sensitivity to neural activity is equivalent to the one of the pristine gSGFET. However, further efforts will have to be devoted to further improve the electronic characteristics as well as homogeneity and yield of the combined sensor technology to reach the maturity required for arrays of large sensor count.

Chapter 6

Conclusion and outlook

This thesis highlights the immense potential two-dimensional materials such as graphene and molybdenum disulfide (MoS_2) have for an application in a novel class of flexible brain-machine-interfaces (BMIs). Graphene's large interfacial capacitance, its record high charge carrier mobility and stable interface with aqueous solutions combined with its mechanical flexibility and biocompatibility, make it ideal for biosensing applications. The graphene solution gated field-effect transistor (gSGFET) takes advantages of these characteristics to accurately measure electric fields originating in ionic dynamics, which form the microscopic basis of neural activity in the brain. MoS_2 and other transition metal dichalcogenides are a suitable complementary material owing to their large direct band-gap which allows the formation of digital circuits required to simultaneously address many of such sensors. To obtain a detailed cortical mapping of brain activity needed to grant for example accurate control of neuro-prostheses, would necessitate BMIs of high sensor count arranged into a dense array providing both, high spatial resolution and large surface coverage. The main focus of this work is to provide a roadmap on how to employ the gSGFET and the MoS_2-FET technologies to develop electrocorticography (ECoG) probes matching these requirements. Such technology development faces two primary challenges. On the one hand, high-resolution BMIs require sensors of high signal-to-noise ratio and recording fidelity due to the spectral diversity of neural signals and their small amplitude on the cortical surface. Yet, the planar atomic structure of two-dimensional materials and their high surface-to-volume ratio make them particularly prone to be affected by poor contact charge injection and high flicker noise, which influence not only the sensor's performance and homogeneity but also its high-frequency operation and its miniaturization towards high-density arrays. On the other hand, connecting each sensor on the array to an external amplifier for signal acquisition becomes an increasingly challenging endeavour for decreasing sensor size and growing sensor number, which typically requires the implementation of multiplexed readout schemes.

The first challenge is discussed in chapter 3. This work investigates different measures to lower the dominant sources of flicker noise in the gSGFET, which originates in both the contact and the channel region. Noise in the contact region is primar-

ily driven by a poor charge injection between the metal contacts and the graphene sheet, which remains a common issue in devices using two-dimensional materials. To improve the charge injection and thus reduce contact noise, the exposure of the graphene contact region to ultra-violet ozone (UVO) prior to metal deposition was explored; it was found to be highly effective owing to a combined effect of surface residue cleaning and controlled defect creation in the graphene sheet underneath the metal contacts. In addition to the benefit on the noise characteristics, the reduction of contact resistance also leads to additional improvements in the sensing capability of the gSGFET, improving the linearity of signal transduction and the homogeneity across devices. Interestingly, it was found that the contact region is the dominant noise source for devices with short channel lengths and, conversely, the channel region was dominant for devices with long channels. Hence, engineering devices of low contact resistance proved critical when developing high density arrays with small sensor dimensions. Noise originating in the channel region, on the other hand, results from an interaction of the free charge carriers with scattering centres and trap states in the channel's proximity. Encapsulating the channel with hexagonal boron nitride (hBN) or similar dielectric films is proposed as a complementary measure to the UVO contact treatment, as it allows to shield transport in the channel from such impurities. Combining and advancing both technological enhancements will ultimately produce graphene-based neural sensors with ultra-low noise characteristics and, thereby, will mark a decisive step in the maturity of the technology.

The challenge of simultaneously connecting a vast number of sensors on such a high density array is addressed in chapter 4. More specifically, the gSGFET technology is explored for operation in a multiplexed addressing scheme, which allows to share connections between several sensors on the array, thus leading to a strongly reduced connector footprint. Graphene's record high carrier mobility and its purely capacitive interface with aqueous solutions offer advantages for high-speed applications such as multiplexed operation compared to other materials such as silicon and organic polymers. Further, it is shown that the nature of the gSGFET as an active electrical component with intrinsic signal amplification allows the realization of multiplexed sensor arrays without the necessity of integrated addressing circuitry, as would be required when using electrodes as sensing elements. Such a strongly simplified addressing concept, which overcomes the hurdle of excessively complex device fabrication, has been utilized to demonstrate the compatibility of the gSGFET with both time-division multiplexed (TDM) and frequency-division multiplexed (FDM) readout schemes, each having advantages and disadvantages. The FDM method relies on more complex electronic circuitry for demodulation and filtering, but provides extremely high sampling rates and compatibility with capacitively coupled biasing, which would be beneficial for a potential translation to an application in humans. Yet, quantization error, bandwidth limitations and inter-site cross-talk pose strict scalability constraints, which can put the promise of sensors far beyond 1000 recording sites out of reach. The TDM method, on the contrary, does not offer equally high sampling rates but allows to incorporate integrated addressing circuitry for crosstalk suppression and would thus be capable to operate arrays of even larger sensor count. To verify that the multiplexed operation of the gSGFET

array is capable of providing artefact-free, high-fidelity recordings of broad-band neural signals, acute and chronic in-vivo recordings in rodents with probes of up to 256 recording sites were acquired in the frame of this PhD with a signal quality comparable to state-of-the-art commercially available neuro sensors. Ultimately, this PhD thesis also explores the integration of flexible switches for multiplexed addressing of the gSGFETs, as a mean to prevent crosstalk degrading recording quality and to allow a further scale-up in sensor count of the μ-ECoG probes. To this end, molybdenum disulfide field-effect transistors (MoS_2-FETs) have been investigated, showing promising capabilities regarding stability, on/off resistance, noise characteristics and transient response, and thus demonstrating their application as such addressing components in flexible probes. A successful monolithic integration of both technologies has been achieved, able to provide cross-talk free recordings of multiplexed sensor arrays without affecting the gSGFET's ability to sense neural activity.

While these results prove that two-dimensional materials are capable to form high quality neural interfaces with multiplexed readout functionality, further steps remain necessary to unlock the technology's full potential. First, despite the progress made in recent years regarding growth and device integration of two-dimensional materials, the reported charge carrier mobilities and low-frequency noise of both graphene and MoS_2 are still falling significantly short of their fundamental limitations. Optimization of these characteristics would not only require to significantly improve the crystal quality of the grown films but also to allow full access to their electronic properties; for instance by creating ideal interfaces with contact materials to improve charge injection and by using encapsulation strategies to decouple the 2D materials from degrading influences of charges in their environment. Second, next to improving the quality of two-dimensional materials and their devices, also their uniformity, reproducibility and yield have to be further increased. This is not only important for fabricating μ-ECoG probes with several thousands of sensors but also essential for their multiplexed operation to minimize switching artefacts and maximize signal amplification. Considering the young age of research on two-dimensional materials and its rapid development during the past years, however, it is very likely that material synthesis, fabrication procedures and technology integration will continue to improve in the years to come, leading to further progress towards solving the challenges discussed above. Such progress could allow the gSGFET to match and even surpass the performance of other neuro-sensing technologies such as platinum-black and PEDOT:PSS-coated electrodes in recording quality, durability, bio-compatibility and scalability. Lastly, to provide a mature and ready-to-use platform for neuro-scientific research and clinical application, the discrete electronic components used in this PhD work to address the sensor-matrix and postprocess signals must be upgraded to commercial grade integrated circuitry. Such transition is currently ongoing with first generations of application-specific integrated circuits (ASICs) for both TDM and FDM undergoing testing.

In summary, the multiplexed μ-ECoG technology developed in the frame of this PhD compares favourably to many state-of-the-art BMIs, paring high sensitivity to not only spike patterns and local-field-potentials but also slow oscillatory brain

activity with the probe's full flexibility and high scalability. A sensor technology with such unique set of compelling features is likely to have a major contribution to the ongoing pursuit of a better understanding of the brain.

Appendix A

Primary publications

A.1 Improved metal-graphene contacts for low-noise, high-density microtransistor arrays for neural sensing

This article reports on efforts to improve the level of low-frequency flicker noise and sensor uniformity in the gSGFET technology and presents an important first steps towards the realization of multiplexed arrays with large sensor count. Poor charge injection at the metal-graphene interface was found to be one of the dominant drivers of low-frequency noise in the gSGFET, in particular for small sensor sizes which are required for high-bandwidth brain-machine-interfaces (BMIs). Treating the contact region with ultraviolet ozone prior metal deposition has been previously reported to lower the contact resistance in graphene field-effect transistors and is also found to significantly improve the noise characteristics in the gSGFET. In addition to low noise, it also provides better bias stability during long recordings, higher sensor homogeneity and extended range of linear signal transduction. A finite elements method model is presented to tentatively explain the reduced noise by current crowding effect through the contact edge and resulting recording quality improvement are verified in-vitro.

Improved metal-graphene contacts for low-noise, high-density microtransistor arrays for neural sensing

Nathan Schaefer [a, b, 1], Ramon Garcia-Cortadella [a, b, 1], Andrea Bonaccini Calia [a, b, 1], Nikolaos Mavredakis [b], Xavi Illa [c, d], Eduard Masvidal-Codina [c], Jose de la Cruz [a], Elena del Corro [a], Laura Rodríguez [a], Elisabet Prats-Alfonso [c, d], Jessica Bousquet [a], Javier Martínez-Aguilar [c, d], Antonio P. Pérez-Marín [a], Clement Hébert [e], Rosa Villa [c, d], David Jiménez [b], Anton Guimerà-Brunet [c, d], Jose A. Garrido [a, f, *]

[a] Catalan Institute of Nanoscience and Nanotechnology (ICN2), CSIC and The Barcelona Institute of Science and Technology, Campus UAB, Bellaterra, Spain
[b] Departament d'Enginyeria Electrònica, Escola d'Enginyeria, Universitat Autònoma de Barcelona, Bellaterra, Spain
[c] Instituto de Microelectrónica de Barcelona IMB-CNM (CSIC), Esfera UAB, Bellaterra, Spain
[d] Centro de Investigación Biomédica en Red en Bioingeniería, Biomateriales y Nanomedicina (CIBER-BBN), Madrid, Spain
[e] Inserm and Université Grenoble Alpes, Saint Martin d'Hères, France
[f] ICREA, Barcelona, Spain

ARTICLE INFO

ABSTRACT

Poor metal contact interfaces are one of the main limitations preventing unhampered access to the full potential of two-dimensional materials in electronics. Here we present graphene solution-gated field-effect-transistors (gSGFETs) with strongly improved linearity, homogeneity and sensitivity for small sensor sizes, resulting from ultraviolet ozone (UVO) contact treatment. The contribution of channel and contact region to the total device conductivity and flicker noise is explored experimentally and explained with a theoretical model. Finally, in-vitro recordings of flexible microelectrocorticography (μ-ECoG) probes were performed to validate the superior sensitivity of the UVO-treated gSGFET to brain-like activity. These results connote an important step towards the fabrication of high-density gSGFET μ-ECoG arrays with state-of-the-art sensitivity and homogeneity, thus demonstrating the potential of this technology as a versatile platform for the new generation of neural interfaces.

© 2020 Elsevier Ltd. All rights reserved.

1. Introduction

With its exceptional properties such as high mobility [1], biocompatibility [2], transparency [3] and mechanical strength [4], graphene has been extensively investigated for application in numerous fields such as electonics [5], photonics and optoelectronics [6], and more recently biomedical engineering [7—9]. Despite the vast potential of graphene, graphene-based devices often fall short of demonstrating their full capabilities, as large metal-graphene contact resistance [10], inhomogeneity among devices [11] and high 1/f noise [12] still hamper their performance.

Hence, great efforts have been undertaken to properly understand the source of noise and of the high contact resistance as well as to find ways to minimize their impact on the device performance.

In a graphene-based field-effect transistor (FET), we can distinguish several contributions to low-frequency noise [12]. For instance, variations in the scattering cross-section of lattice defects generate mobility fluctuations which ultimately cause changes in the resistance of graphene. In addition, charge trap states in the graphene channel or in the surrounding materials such as the substrate, gate dielectrics or encapsulation layers can cause fluctuations in the number of charge carriers. Due to the 2-dimensional nature of graphene, the latter is expected to be dominant, as shown for certain transistor configurations [13]. The use of buffer layer materials such as hexagonal boron nitride (hBN) [14] or engineering free-standing graphene channels [15] has been proposed to decouple the graphene sheet from the environment, and thus reduce flicker noise. Degradation of the electrical properties due to

---

the closer environment the is not restricted to graphene but has been also observed for other two-dimensional materials such as transition-metal-dichalcogenites (e.g. MoS_2) [16] and layered III-VI semiconductors (i.e. InSe) [17].

High contact resistance, resulting from the work function mismatch between graphene and metals as well as from the low density of states of graphene, has a negative impact on the performance of graphene FETs, resulting in a poor charge transfer and thus in a low conductance of graphene FETs [10,18,19]. Common strategies to reduce contact resistance include the use of metals which interact strongly with graphene [20–22] or the creation of defects in the graphene lattice; for instance, the introduction of dangling bonds can enhance the graphene-metal interaction. Typical ways to create defects in graphene include, patterning the graphene sheet beneath the metal contacts, increasing the graphene edge length [23–25], as well as treating the contacted graphene with oxygen plasma [26] or ozone [27]. Despite the vast number of available techniques to provide low contact resistance, the goal of most published studies focuses on setting new performance benchmarks for a single device by using nanofabrication techniques and exfoliated graphene [14,28], and only very few of them address the technique's scalability for wafer-size fabrication [29]. Since the success of 2D materials will ultimately depend on their translation from the laboratory to industry, demonstration of large-scale fabrication processes with high homogeneity and high yield are of critical importance. In addition to their impact on the current-voltage characteristics of the transistor, metal-graphene

contacts have also been reported to exhibit time-dependent resistance fluctuations [30], thus contributing to the low-frequency noise. Although significant efforts have been devoted to a better understanding of the electrical noise in graphene [12], no consensus has been reached yet on whether channel or contact noise is dominant in graphene FETs, what the underlying noise-generating mechanisms are and how noise depends on channel and contact geometry [28,31–35].

Here we use wafer-processed graphene solution-gated field-effect transistors (gSGFETs) to demonstrate the effect of the contact resistance on the sensing performance of these devices. gSGFETs have been widely explored for application in micro-electrocorticography (μ-ECoG) arrays to record neural activity [9,36,37]. As neural signals are usually extremely small in amplitude (typically below 100 μV), having devices with good signal-to-noise ratio (SNR) is of paramount importance for high-quality recordings. Previous work investigated the bias-dependence of low-frequency noise in gSGFETs and demonstrated that carrier density fluctuations can generate low-frequency noise in the channel [13]. However, the impact of contact noise in g-SGFETs has not been addressed so far. In this work, in addition to present a fundamental noise study, we also explore the impact of low contact resistance on the actual recording quality of neural sensor-arrays considering factors such as signal-to-noise ratio, sensor homogeneity and linearity of signal transduction.
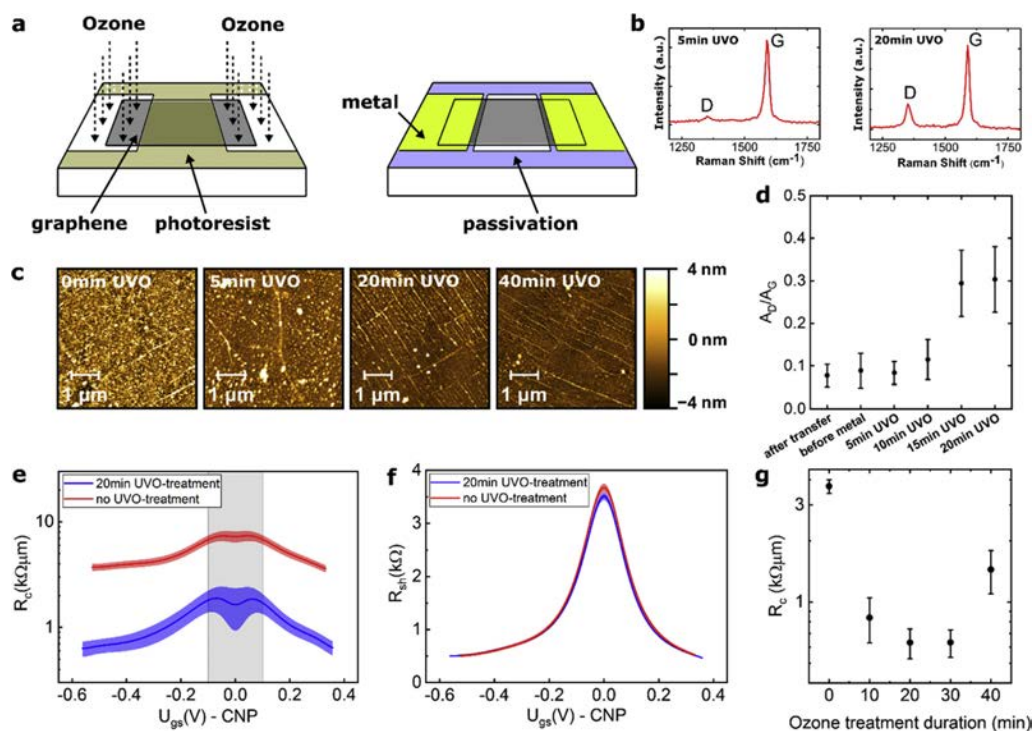

Fig. 1. **Improving contact resistance by surface cleaning and defect creation**. a. Schematic of device fabrication with UVO applied to the graphene contact region prior to the metal deposition. b. Raman spectra after 5 min and 20 min treatment, indicating an increase of the D-peak with treatment duration. c. Surface roughness of the graphene layers measured by AFM. The lowering of the root-mean-square values with longer UVO treatments (2.1 nm, 1.3 nm, 1.1 nm and 0.8 nm, for 0 min, 5 min, 20 min, and 40 min duration, respectively) indicates the continuous cleaning of surface residues. d. Ratio of peak intensities of the D-band and G-band of single-layer graphene used as an indicator for the amount of residues and defects in the graphene sheet. R_c (e) and R_{sh} (f) measured as a function of applied gate bias for UVO-treated and non-treated devices. The shaded region close to the charge neutrality point (CNP) does not yield reliable values for R_c, as here the applied gate bias reaches similar values than the drain-source bias ($U_{ds} = 20$ mV), leading to a non-constant R_{sh} along the channel. g. R_c at U_{gs} - CNP $= -0.5$ V as a function of UVO-treatment duration, showing optimal results for 20 min−30 min UV ozone exposure. (A colour version of this figure can be viewed online).

2. Experimental

2.1. Graphene CVD growth and wet transfer

The copper foil used for the chemical vapor deposition of graphene (25 μm thick Alfa Aesar coated of size 4.5 cm × 7 cm) was first electropolished for 5 min in a solution (1 L of H_2O, 0.5 L of H_3PO_4, 0.5 L of ethanol, 0.1 L of isopropanol and 10 g of urea) at a fixed current density of 62 mA/cm2 and subsequently loaded into a planar quartz tube (length of 160 cm and diameter of 6 cm) heated by a three-zone oven. A thermal annealing was performed for 1 h at 1050 °C (under 400 sccm Argon flow at 100 mbar pressure) to stabilize the temperature prior to the 10 min graphene growth step (gas mixture of 1000 sccm of Argon, 200 sccm of hydrogen and 2 sccm of methane, at 12 mbar pressure). The sample is then quenched down to room temperature by removing the tube from the heating zone. To transfer the graphene film, poly(methyl methacrylate) (PMMA A4) was spun onto the sample and dried at room temperature for 12 h. Afterwards, the backside graphene was removed by oxygen plasma and the sample was kept floating for at least 6 h in solution of $FeCl_3$/HCl to remove the copper. Subsequently, the sample was cleaned several times in deionized water, before being transferred onto the substrate. The wafer was then dried and thermally annealed in ultra-high vacuum (30 min at 40 °C, then gradually ramped up to 180 °C), before the PMMA was dissolved in acetone and isopropanol. Right after the growth, the quality and uniformity of the graphene monolayer is assessed by scanning electron microscopy (SEM) and Raman Spectroscopy (30 μm × 30 μm mapping). As detailed in the supplementary information, the graphene layers exhibit a domain size between 10 μm and 20 μm, a low defect density and high uniformity across the entire sample. The averaged full-width-half-maximum of the 2D Raman peaks of the used samples is around 33 cm^{-1}, indicating a low percentage of second nucelation.

2.2. Device fabrication

The devices for the transfer length method (TLM) study were fabricated by contact photolithography on 4 inch Si/SiO_2 wafers. In a first step, graphene was transferred, patterned (HiPR6512 photoresist, FujiFilm) and etched by deep reactive-ion etching (DRIE) for 1 min at 150 W in oxygen plasma. Subsequently, the photoresist for the contact metal layer was deposited, illuminated through a chromium mask and developed. Before evaporating 20 nm Ni and 200 nm Au (using an e-beam evaporator) the wafer was exposed to UV-ozone [Jelight Model 42] [27]. After lift-off, a 2 μm passivation layer (SU8-2005 MicroChem) is deposited with open windows in the channel region.

The flexible ECoG-probes were processed following the same protocol; however, a 7 μm layer of polyimide (PI-2611 HD MicroSystems) was spun onto the Si wafer prior to fabrication to serve as the flexible substrate and structured via DRIE to allow individual peeling of each probe after all steps are finished. Due to the higher mechanical stress in the flexible probes, an additional metal layer (20 nm Ti and 200 nm Au) was used to improve adhesion between the top metal layer and the substrate, yet not directly contacting the graphene channel.

2.3. Device characterization and recording setup

Transfer characteristics and noise were measured with custom-built electronics, performing current-to-voltage conversion, filtering and bias-control of up to 16 transistors simultaneously. To allow sensitivity towards large DC currents and high gain for noise detection, the converted signals are split into DC (frequency < 0.1 Hz) and AC (0.1 Hz < frequency < 5 kHz) components. A commercial data acquisition system (National Instruments USB-6363) was used to provide the applied biases and record the voltage signals after conversion [36].

2.4. Raman spectroscopy and atomic force microscopy

The Raman spectra were acquired with a Witec spectrometer in backscattering configuration, using a 600 gr/nm grating which provided a spectral resolution of 3 cm^{-1}/pixel. A 488 nm excitation laser (1 mW power) was focused on the sample with a 50x objective leading to a spatial resolution below 0.8 μm. The integrated peak intensity ratio A_D/A_G is calculated by fitting each peak with a Lorentzian after previously substrating the background. Each data point shown in Fig. 1a was obtained from the statistical analysis of Raman mappings of 15 μm × 40 μm contact region. An Asylum MFP-3D atomic force microscope (AFM) was used to characterize the surface in standard air-tapping mode (Fig. 1c).

2.5. Contact resistance from transfer length method

The contact resistance (R_c) and the sheet resistance (R_{sheet}) values shown in Fig. 1e—g have been extracted by applying the TLM to different devices of 2.5 μm, 5 μm, 8 μm, 10 μm, 20 μm and 40 μm channel length and 40 μm channel width. For each length, the resistance value has been extracted from the mean value of several measurements and fitted with a linear regression model to extract the values for R_c and R_{sheet}. To further improve the accuracy of this approach, outlier resistance values which strongly deviate from the median of each transistor type (outside the 25th and 75th percentile) were not used in the analysis.

3. Results and discussion

3.1. Low contact resistance by surface cleaning and defect creation

Ultraviolet ozone (UVO) treatment has been previously reported as an efficient way to reduce contact resistance in graphene FETs [27,29]. Part of the effect is attributed to removal of fabrication residues which leads to a decrease of the intensity ratio of the D-peak to the G-peak (A_D/A_G). However, longer treatment durations are known to break up the sp^2-bonds and cause defects, which increases A_D/A_G. During the initial phase of defect creation, UVO exposure predominately leads to the formation of sp^3-bonds through the attachment of oxygen containing groups [38]. On the other hand, in the case of high defect density (n_D/n_C above 10^{-3}) due to long UVO treatment durations or increased sample temperature during the treatment, it has been shown that a transition from sp^3-type towards vacancy-type dominated defects takes place [42,43]. In our study, the UVO has been applied at room temperature and due to the relatively small size of the exposed contact region, surrounded by areas covered with photoresist, defects in the graphene film at the contacts are induced at a slow rate. In the case of the 20 min UVO duration, the resulting low A_D/A_G-ratio (0.3) together with the absence of a noticeable D' band indicates a low defect density, predominantly with a sp^3-type nature [42,43]. Since the sp^2 orbitals hinder charge injection along the z-plane [44,45], the creation of defects by long UVO-treatments further decreases the contact resistance.

Fig. 1d shows the evolution of A_D/A_G as a function of treatment duration. The results are comparable to the ones presented in literature [27], with the exact duration depending on the experimental conditions of the UVO-treatment. The accompanying change in surface topology was analyzed by AFM. Fig. 1c illustrates the surface roughness before and after treatments of varying
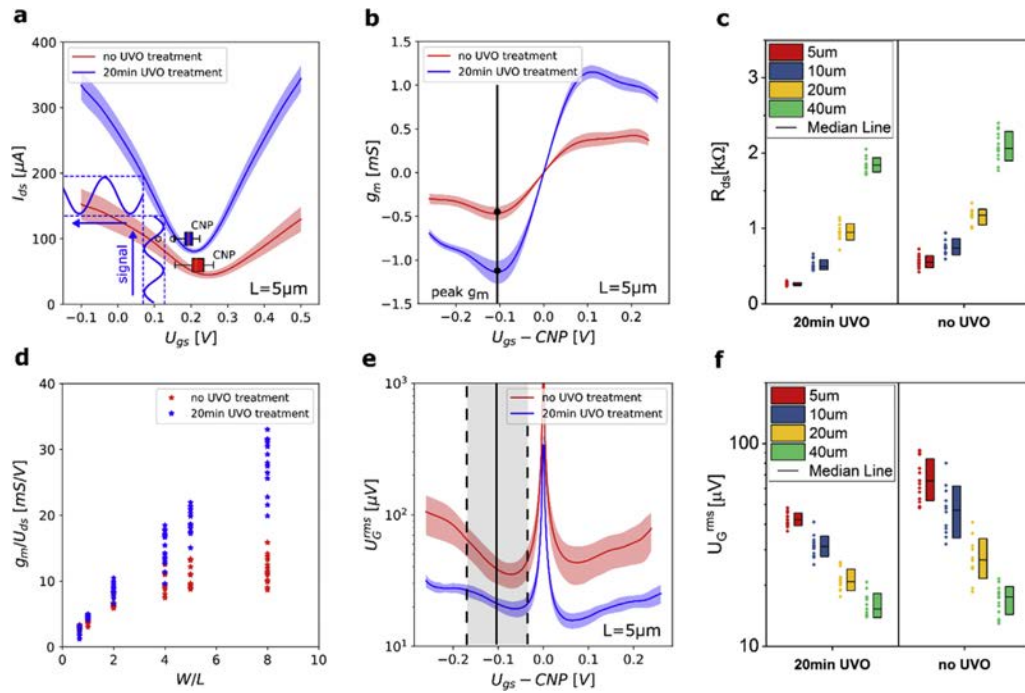
Fig. 2. Effect of contact resistance on linearity of signal transduction, homogeneity and signal-to-noise ratio of gSFGETs. Average value and standard deviation of transfer curves for **a.** drain-source current I_{ds}, **b.** transconductance g_m and **e.** effective gate noise U_G^{rms} for devices of 5 μm channel length and 40 μm channel width. **d.** Normalized transconductance g_m/U_{ds} (values within 25th and 75th percentile) versus width-to-length ratio of the channel. The statistical variation of the R_{ds} (**c**) and U_G^{rms} (**f**) values at peak transconductance (U_{gs} = CNP - 0,1 V) for devices of different length are also shown. (A colour version of this figure can be viewed online).

duration, revealing the continuous cleaning of surface residues; this results in a lowering of the measured roughness (from a root-mean-square value of 2.1 nm for no treatment, down to 0.8 nm for 40min of UVO treatment) and a better visualization of the wrinkled surface of the graphene sheet. Fig. 1e and 1f shows the UVO influence on the contact resistance and sheet resistance of the graphene channel. The symmetric decrease (for electrons and holes) of R_c away from the charge neutrality point (CNP) has been previously reported for back-gated graphene FETs using Ni contacts [18,21] and has been associated to the poor charge screening in 2D materials with low charge carrier densities [46]. It is important to note that the TLM assumes a constant sheet resistance per unit area across the whole transistor channel. However, this assumption is only correct for cases in which the applied gate bias is much larger than the drain-source bias. While this is mostly true for field-effect-transistors that usea relatively thick dielectrics, solution-gated FETs are normally operated at much lower gate voltages. In this case, the potential difference between channel and gate is not constant but changes gradually along the channel, which leads to a non-uniform sheet resistance and can result in unreliable values for R_c in the grey shaded region of Fig. 1e. Values for R_c far away from the CNP (Fig. 1g), yield around 3-4 kΩμm for the case of a pristine Ni/Au top-contact structure and reach a minimum as low as 600 Ωμm for a 20−30 min UVO treatment duration. Longer treatments result in an increase of contact resistance, as a high defect density in the UVO-treated graphene sheet eventually hampers charge conduction. On the other hand, the sheet resistance remains independent of the UVO treatment as expected, since the channel region is protected by the photoresist.

3.2. Improved linearity of signal transduction, homogeneity and signal-to-noise ratio in short channel transistors

When planning the use of gSGFETs as a transducer for neural activity, there are several factors to be considered to obtain distortion-free, high-resolution recordings. Fig. 2 illustrates how contact resistance influences the sensing performance of gSGFETs, by comparing devices (of varying channel length and 40 μm channel width) with low (20 min UVO treatment) and high contact resistance (no UVO treatment). The suitability of the gSGFET for sensing applications, in which the device converts the voltage variation of a signal at the gate into a current modulation between the drain and source terminals, depends on the linearity of its transfer characteristics. A high contact resistance at the metal-graphene interface causes a flattening of the transfer curve away from the CNP (Fig. 2a), limiting the range of linear operation. The resulting non-linearities can cause distortions in the transduced signal, thus degrading the recording quality of the graphene transistors. Furthermore, a flattening of the transfer curve also limits the gSGFET's transconductance, defined as the change of drain-source current induced by a changing gate bias ($g_m = dI_{ds}/dU_{gs}$), which is a measure for the device's sensitivity. The gSGFET is commonly operated at the bias conditions which provide peak transconductance (illustrated in Fig. 2b). Fig. 2d shows how the normalized peak-transconductance value changes for devices of varying channel length (L = 5 μm, 8 μm, 10 μm, 20 μm, 40 μm, 60 μm) and constant channel width (W = 40 μm). In case of low R_c (i.e. for UVO-treated devices) the g_m/U_{ds} exhibits a near-linear increase with W/L, while for devices with high R_c (non-treated) it is increasingly limited for short channels. As a high transconductance is generally desirable for sensing applications to allow for best
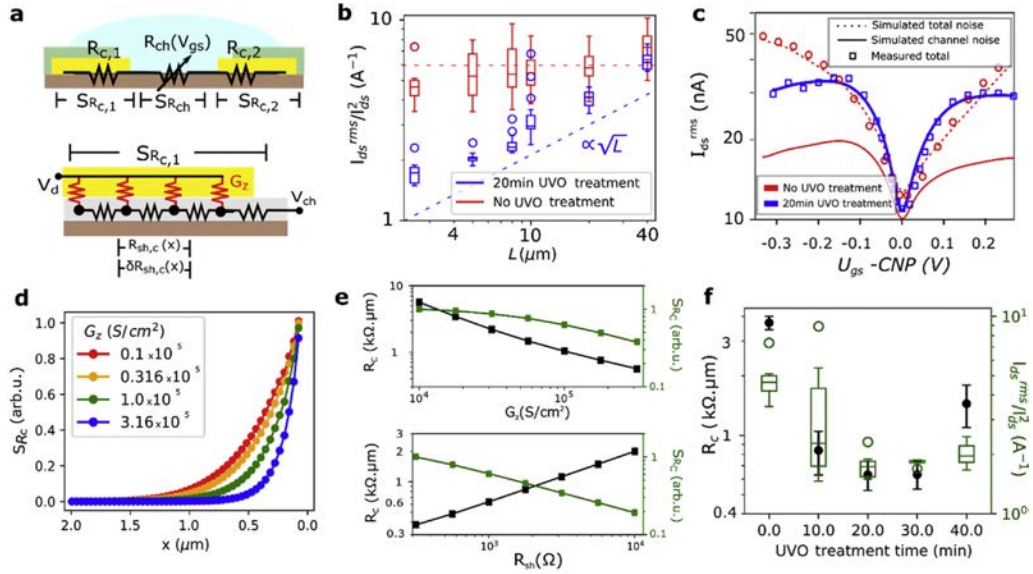
Fig. 3. Geometrical dependence of contact and channel noise in gSGFETs. a. Top: schematic of a gSGFET showing the contact resistance ($R_c = R_{c,1} + R_{c,2}$), channel resistance (R_{ch}) and the noise contributions from the contacts ($S_{R_c} = S_{R_{c,1}} + S_{R_{c,2}}$) and channel ($S_{R_{ch}}$). Bottom: Schematic of the equivalent circuit of the transmission-line contact at the graphene-metal interface. The distributed elements representing the sheet resistance of graphene along the contact ($R_{sh,c}(x)$) are defined together with the local fluctuations in the sheet resistance ($\delta R_{sh,c}(x)$). The drain voltage (V_d) and the potential at the channel/contact interface (V_{ch}) are also defined. b. Dependence of the normalized noise (I_{ds}^{rms} / I_{ds}^2) versus the channel length (L) for devices with non-treated contacts and for devices with contacts treated with UVO for 20 min ($U_{gs} = CNP - 0.1\ V$). A change from an approximately L-independent regime to a $\propto \sqrt{L}$ regime is observed. c. Experimentally obtained integrated noise I_{ds}^{rms} versus U_{gs}, plotted for non-treated contacts and contacts treated with UVO for 20 min and channel length of 5 μm. The lines correspond to the fitting of the experimental data with a model that considers the contributions of the channel noise (solid line) only and of the channel plus contact noise (dashed line). In UVO-treated devices the channel noise model fully describes the U_{gs} dependence of I_{ds}^{rms} (both curves exactly overlap). d. Local contribution of resistance fluctuations to S_{R_c} along the contact, shown for different values of conductance across graphene-metal interface (G_z), according to the FEM model described in the main text. e. Evolution of R_c (left axis) and S_{R_c} (right axis) with G_z (top) and $R_{sh,c}$ (bottom). f. Experimentally obtained R_c (left axis) and I_{ds}^{rms} / I_{ds}^2 (right axis) shown for different UVO treatment durations and channel length of 5 μm. (A colour version of this figure can be viewed online).

signal transduction, the influence of the contact resistance has to be considered for the choice of the sensor channel geometry.

Arguably, one of the most critical performance indicators of the gSGFET is its equivalent rms gate noise U_G^{rms} (Fig. 2e), which relates the intrinsic rms current noise I_{ds}^{rms} (integrated current noise over the frequency bandwidth of interest; here filtered between 1 and 100 Hz) of the transistor with its transconductance ($U_G^{rms} = I_{ds}^{rms} / g_m$), and represents the detection threshold for signals applied to the gate. At peak-g_m a significant reduction of the effective gate noise can be seen in the UVO-treated devices, which is most striking for short channel lengths. This difference becomes more pronounced when moving further away from the CNP: U_G^{rms} remains fairly constant in the case of low R_c and increases rapidly for devices with high R_c. This is particularly interesting when operating the gSGFET in-vivo, which typically requires using a common bias point for all devices. However, local changes in doping across the different recording sites, as well as electrochemical drifts of the reference electrode during long-lasting chronic recordings make it virtually impossible to operate all devices simultaneously at their ideal bias condition. As neural interfaces are mainly considered for long-term recordings, ranging from several days up to months or even years of implantation time, stable recording quality is mandatory. Consequently, having a constant SNR in a large bias window, resulting from a voltage-independent U_G^{rms}, is crucial to providing optimal sensing capabilities across the sensor array throughout long recording times. In addition to the positive effect of the UVO treatment on the contact resistance and noise of the devices, Fig. 2f shows that the dispersion across different recording sites is significantly reduced in the case of devices with the UVO treatment. This suggests that poor contact interfaces are

responsible for the dispersion observed in the array in terms of noise (Fig. 2f) and conductance (Fig. 2c), possibly overruling the contribution of the dispersion in graphene quality in the channel.

3.3. Noise contribution from contact and channel

The improvement in device performance resulting from the contact treatment directly leads to two questions: i) What is the contribution from the contact noise compared to the channel noise?, and ii) What is the reason for the contact noise improvement? Answering these questions is critical for knowing to which extent contact noise mitigation will affect the total noise in g-SGFETs, and to understand how to optimize the contact treatment procedure. The total normalized noise S_I/I_{ds}^2 generated in a gSGFET includes the contribution from the contacts (S_{R_c}) and from the channel ($S_{R_{ch}}$) (see Fig. 3a-top). The contributions of these terms to the measured current noise can be added linearly with the proper normalization:

$$\frac{S_I}{I_{ds}^2} = \frac{S_{R_c} + S_{R_{ch}}}{R_T^2} \tag{1}$$

where R_T is the total resistance of the transistor. The dependence of each of these terms on the channel width (W) and length (L) will determine their relative contribution to the total noise for different geometries and sizes. The dependence on geometry of S_{R_c} and $S_{R_{ch}}$ can be expressed explicitly:
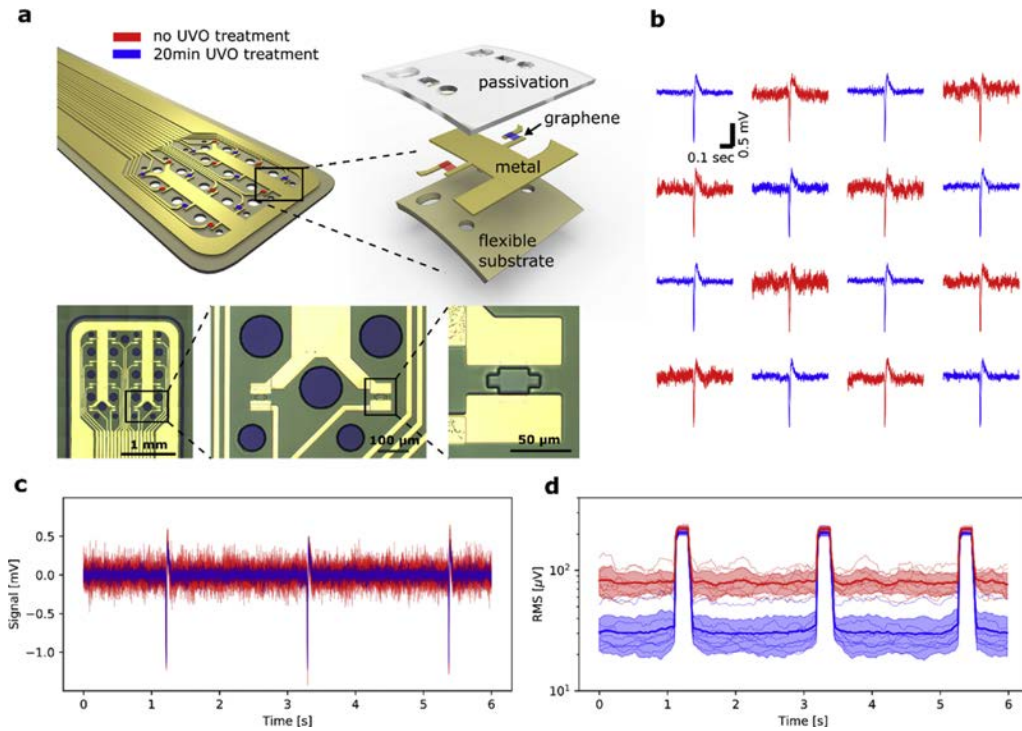
Fig. 4. In-vitro assessment of recording quality of gSGFETs using hippocampal population spike-like signals. a. Schematic and optical images of a flexible epicortical probe with 16 gSGFET sensors (20 μm × 20 μm channel area), with UVO-treated and non-treated sensors arranged in a chessboard layout. b. Map of a single spike event recorded by each transistor of the array. c. Overlapped presentation of all recordings for several spike events. d. The root-mean-square (rms) value of the recorded signal (for each point integrated over a timespan of 200 ms) and its standard deviation are shown for each individual gSGFET as well as the mean value of all devices, revealing a significant improvement of the signal-to-noise ratio. (A colour version of this figure can be viewed online).

$$\frac{S_I f}{I_{ds}^4} = \left[k_{R_c} \Big/ W^3 + k_{R_{ch}} L \Big/ \left(W^3 \right) \right] \Big/ V_{ds}^2 \qquad (2)$$

where k_{R_c} and $k_{R_{ch}}$ include all the constants which are independent of the channel dimensions for S_{R_c} and $S_{R_{ch}}$ respectively (see supplementary information). The relative contribution of each term can therefore be identified by evaluating the dependence of noise on L. Fig. 3b shows the normalized integrated current noise, I_{ds}^{rms}/I_{ds}^2 (where $I_{ds}^{rms} \propto \sqrt{S_I}$), for different channel lengths. As demonstrated above, the measured noise is reduced for devices with the UVO treatment. Interestingly, the derived dependence of the measured noise on L reveals the transition from a regime dominated by contact noise to a regime dominated by channel noise. The channel length for which the two terms contribute equally is approximately 60 μm. For devices with shorter channel length the UVO treatment results in a significant improvement on the total noise of the g-SGFETs. It is important to note that the improvement in U_G^{rms} is not only caused by the increase in g_m (Fig. 2), but also by the reduction of the intrinsic noise of the contact S_{R_c}. The transition from a regime dominated by contact noise to one dominated by channel noise can be confirmed by modelling the U_{gs}-dependence of the measured current noise. Following the model presented in Ref. [13], which describes the U_{gs}-dependence of I_{ds}^{rms} when channel noise dominates, and including the contribution of the contact noise using Eq. (1) (assuming a constant R_c), we have fitted the experimental data to separate the contributions of contact and channel to the total noise. Fig. 3c compares the measured $I_{ds}^{rms} - U_{gs}$ for g-SGFETs with UVO-treated and non-treated contacts. In the

case of the non-treated devices the contribution from the contacts dominates the total transistor noise in most of the U_{gs} range. Conversely, for UVO-treated devices the U_{gs} dependence of the channel noise presents a characteristic M-shape, which has been attributed to the dominance of channel noise [13]. Note that in Fig. 3c the I_{ds}^{rms} is not normalized, therefore it does not directly represent the noise sources S_{R_c} and $S_{R_{ch}}$.

We turn now to discussing the cause of the contact noise improvement by the UVO treatment. To this end, we start by modelling the contact in graphene with the transmission-line model equivalent circuit shown in Fig. 3a, with G_z representing the conductance through the metal-graphene interface z-plane and $R_{sh,c}(x)$ representing the local values of the graphene sheet resistance at the contact. In this type of contacts, the current crowding [47] effect causes a non-homogenous current injection into the graphene sheet, with the highest current flowing next to the metal edge and the lowest at the end of the contact (see supplementary information). This attenuation of the current density at the contact is characterized by the transfer length L_T, at which the current density has decreased by a factor e. We suggest that the UVO treatment causes an increase in G_z, possibly due to elimination of fabrication residues and/or the creation of defects in graphene [27]. Such defects also produce an increase in the sheet resistance of graphene ($R_{sh,c}$) at the contacts, see Fig. 3a and [48]. Note that both the increase of G_z and increase of R_{sh} promote the current crowding effect, producing the shortening of L_T (see supplementary information). Following previous work [14], we assume that the noise originates from resistance fluctuations in the graphene sheet under the metal contacts. These fluctuations can be caused by mobility

fluctuations or by changes in the number of charge carriers trapped in the graphene substrate. Considering the equivalent circuit shown in Fig. 3a, the power of local fluctuations in the sheet resistance of graphene $\delta R_{sh,c}$ adds up linearly. However, in this distributed elements circuit the resistance fluctuations at different positions along the contact contribute differently to the overall contact noise. The contribution of each local noise source can be calculated by weighting its noise power with the term $dR_C/dR_{sh,c}(x)$ and integrating over the whole contact length (L_c) (see supplementary information). To perform this calculation, we have modelled the transmission-line contact using the finite elements method (FEM), as detailed in the supplementary information. Fig. 3d shows the calculated local contribution from each section of the contact for different values of conductance across the z-plane (G_z). When the current crowding effect is enhanced, the contribution to noise from local sources is confined closer to the metal edge. Similarly, when $R_{sh,c}$ is increased the same effect occurs (see supplementary information). The total integrated contact noise S_{R_c} is shown in Fig. 3e together with R_c as a function of G_z and $R_{sh,c}$, revealing that the simultaneous drop in R_c and in S_{R_c} can only be caused by an increase in G_z. Fig. 3f shows the measured R_c and S_{R_c} of the gSGFETs for different UVO treatment durations. It is possible to observe a monotonic decrease of both parameters until 20 min treatment duration, indicating that the contact noise mitigation in this range of UVO treatment is caused by an increase in G_z, rather than by an increase in $R_{sh,c}$. For UVO treatments above 30 min, however, the trend changes: R_c increases with the treatment duration, while S_{R_c} remains approximately constant (see supplementary information). We tentatively explain the increase in R_c as a result of the creation of defects on the graphene sheet at the contact, that causes a significant increase in $R_{sh,c}$ [39]. These results demonstrate the reduction of the noise contributions from the contacts by UVO treatment and offer an explanation to understand the origin and limits of this improvement.

3.4. Enhanced performance of flexible gSGFET ECoG-array for neural interfaces

After the above discussion on the effect of contact resistance on overall gSGFET performance and its low-frequency noise, we examine now how this improved performance is translated to the application of flexible gSGFET probes for neural activity recordings. Fig. 4a shows an illustration of this technology, combining several metal and passivation layers on a flexible polyimide substrate (fabrication described in the experimental section), corresponding to an array of 16 microtransistors. A squared channel geometry of 20 μm × 20 μm for each transistor is used to validate the performance of the flexible probe. The distance between transistors is 400 μm.

To exclude the variability due to the use of different graphene samples, the graphene transfer procedure or local changes of electronic properties in the graphene sheet, UVO-treated and non-treated gSGFETs are distributed in a chessboard arrangement on the same array (see transfer curves in Fig. S4 in supplementary information). A reliable comparison of recording quality across different recording sites is difficult in-vivo, as locally recorded signals depend on many factors such as the underlying brain tissue and the adhesion of each sensor to it. Therefore, a periodically generated artificial hippocampal population spike (Multi Channel Systems signal generator ME-W-SG) was applied to a phosphate-buffered saline solution (PBS, 10 mM). Fig. 4b displays one spike event recorded by each transistor of the array. Fig. 4c overlaps all the recordings for several events, demonstrating the improvement of SNR for the UVO-treated devices. To better quantify the SNR, the root-mean-square value of the recording in Fig. 4c and its standard

deviation are plotted in Fig. 4d, showing average noise values around 80 μV for non-treated and 30 μV for UVO-treated devices. This presents an over twofold improvement of signal resolution for such sensor geometry, due to the improved metal-graphene contacts and compares very favorably to previously reported noise values in gSGFETs [36] (see Fig. S4d in supplementary information). Significantly reduced noise values due to the contact treatment have been reproduced across several probes on a single wafer and between different batches, validating the high reliability of this technique (see Fig. S4c in supplementary information). Small dispersion in noise values can be explained by minor variations in graphene quality and by the amount of surface residues between different devices.

4. Summary

Here we have shown the critical importance of the contact resistance for the performance of graphene solution-gated field-effect transistors in neural sensing applications. Poor contacts reduce the linearity of the transfer characteristics causing signal distortions, lower the signal-to-noise ratio of the recorded signal and limit the sensor homogeneity. Exposing the contact region of the graphene channel to UV-ozone before deposition of the contacting metal, is shown to significantly improve charge injection at the contacts by a combination of surface cleaning and defect creation. A theoretical model is used to understand the transition from contact-dominated to channel-dominated noise as a consequence of low contact resistance, and to assess its effect on the total noise of gSGFETs with different channel geometries. Finally, the compatibility of the contact improvement treatment with flexible substrates is validated, demonstrating the fabrication of flexible ECoG-arrays of gSGFETs exhibiting high signal-to-noise ratio.

The development of a novel class of brain-machine interfaces capable of providing further insights into the working paradigms of the brain and granting accurate control of neuro-prostheses might eventually require integrating brain-machine interfaces (BMIs) with single-neuron resolution (cell-body only several μm in size). Considering the increasing dominance of poor contacts on the SNR with decreasing sensor size, improved contact interfaces will become indispensable when moving the gSGFET technology towards this goal. Our work demonstrates a scalable technique to provide high-quality metal-graphene interfaces with low contact resistance, paving the way for low noise, high-density neural interfaces based on graphene transistors.

Acknowledgements

Appendix A. Supplementary data

Supplementary data to this article can be found online at https://doi.org/10.1016/j.carbon.2020.01.066.

References

[1] L. Banszerus, M. Schmitz, S. Engels, J. Dauber, M. Oellers, F. Haupt, K. Watanabe, T. Taniguchi, B. Beschoten, C. Stampfer, Ultrahigh-mobility graphene devices from chemical vapor deposition on reusable copper, Sci. Adv. 1 (2015) 1—7, https://doi.org/10.1126/sciadv.1500222.

[2] J. Conroy, N.K. Verma, R.J. Smith, E. Rezvani, G.S. Duesberg, J.N. Coleman, Y. Volkov, Biocompatibility of pristine graphene monolayers, nanosheets and thin films, ArXiv. http://arxiv.org/abs/1406.2497, 2014.

[3] R.R. Nair, P. Blake, A.N. Grigorenko, K.S. Novoselov, T.J. Booth, T. Stauber, N.M.R. Peres, A.K. Geim, Fine structure constant defines visual transparency of graphene, Science 320 (2008) 1308, https://doi.org/10.1126/science.1156965, 80.

[4] D.G. Papageorgiou, I.A. Kinloch, R.J. Young, Progress in Materials Science Mechanical properties of graphene and graphene-based nanocomposites, Prog. Mater. Sci. 90 (2017) 75—127, https://doi.org/10.1016/j.pmatsci.2017.07.004.

[5] F. Schwierz, Graphene transistors, Nat. Publ. Gr. 5 (2010) 4—5, https://doi.org/10.1038/nnano.2010.89.

[6] F. Bonaccorso, Z. Sun, T. Hasan, A.C. Ferrari, Graphene photonics and opto-electronics, Nat. Photon. 4 (2010) 611—622, https://doi.org/10.1038/nphoton.2010.186.

[7] C. Bussy, D. Jasim, N. Lozano, D. Terry, K. Kostarelos, The current graphene safety landscape-a literature mining exercise, Nanoscale 7 (2015) 6432—6435, https://doi.org/10.1039/c5nr00236b.

[8] T. Kuila, S. Bose, A.K. Mishra, P. Khanra, N.H. Kim, J.H. Lee, Chemical functionalization of graphene and its applications, Prog. Mater. Sci. 57 (2012) 1061—1105, https://doi.org/10.1016/j.pmatsci.2012.03.002.

[9] K. Kostarelos, M. Vincent, C. Hebert, J.A. Garrido, Graphene in the design and engineering of next-generation neural interfaces, Adv. Mater. 29 (2017) 1—7, https://doi.org/10.1002/adma.201700909.

[10] F. Giubileo, A. Di Bartolomeo, The role of contact resistance in graphene field-effect devices, Prog. Surf. Sci. 92 (2017) 143—175, https://doi.org/10.1016/j.progsurf.2017.05.002.

[11] Y. Zhang, V.W. Brar, C. Girit, A. Zettl, M.F. Crommie, Origin of spatial charge inhomogeneity in graphene, Nat. Phys. 5 (2009) 722—726, https://doi.org/10.1038/nphys1365.

[12] A.A. Balandin, Low-frequency 1/f noise in graphene devices, Nat. Nanotechnol. 8 (2013) 549—555, https://doi.org/10.1038/nnano.2013.144.

[13] N. Mavredakis, R. Garcia Cortadella, A. Bonaccini Calia, J.A. Garrido, D. Jiménez,

[14] P. Karnatak, T.P. Sai, S. Goswami, S. Ghatak, S. Kaushal, Current crowding mediated large contact noise in graphene field-effect transistors, Nat. Commun. 7 (2016) 1—8, https://doi.org/10.1038/ncomms13703.

[15] Z. Cheng, Q. Li, Z. Li, Q. Zhou, Y. Fang, Suspended graphene sensors with improved signal and reduced noise, Nano Lett. 10 (2010) 1864—1868, https://doi.org/10.1021/nl100633g.

[16] X. Cui, G. Lee, Y.D. Kim, G. Arefe, P.Y. Huang, C. Lee, D.A. Chenet, X. Zhang, L. Wang, F. Ye, F. Pizzocchero, B.S. Jessen, K. Watanabe, T. Taniguchi, D.A. Muller, T. Low, P. Kim, J. Hone, Multi-terminal transport measurements of MoS2 using a van der Waals heterostructure device platform, Nat. Nanotechnol. (2015) 1—7, https://doi.org/10.1038/nnano.2015.70.

[17] W. Feng, W. Zheng, W. Cao, P. Hu, Back gated multilayer InSe transistors with enhanced carrier mobilities via the suppression of carrier scattering from a dielectric interface. https://doi.org/10.1002/adma.201402427, 2014, 6587-6593.

[18] S.M. Song, J.K. Park, O.J. Sul, B.J. Cho, Determination of work function of graphene under a metal electrode and its role in contact resistance, Nano Lett. 12 (2012) 3887—3892, https://doi.org/10.1021/nl300266p.

[19] A. Allain, J. Kang, K. Banerjee, A. Kis, Electrical contacts to two-dimensional semiconductors, Nat. Mater. 14 (2015) 1195—1205, https://doi.org/10.1038/nmat4452.

[20] Low contact resistance metals for graphene based devices, Diam. Relat. Mater. 24 (2012) 171—174, https://doi.org/10.1016/J.DIAMOND.2012.01.019.

[21] W.S. Leong, C.T. Nai, J.T.L. Thong, What does annealing do to metal—graphene contacts? Nano Lett. 14 (2014) 3840—3847, https://doi.org/10.1021/nl500999r.

[22] A. Gahoi, V. Passi, S. Kataria, S. Wagner, A. Bablich, M.C. Lemme, Systematic comparison of metal contacts on CVD graphene, in: 2015 45th Eur. Solid State Device Res. Conf., IEEE, 2015, pp. 184—187, https://doi.org/10.1109/ESSDERC.2015.7324744.

[23] W.S. Leong, H. Gong, J.T.L. Thong, Low-contact-resistance graphene devices with nickel-etched-graphene contacts, ACS Nano 8 (2014) 994—1001, https://doi.org/10.1021/nn405834b.

[24] H.Y. Park, W.S. Jung, D.H. Kang, J. Jeon, G. Yoo, Y. Park, J. Lee, Y.H. Jang, J. Lee, S. Park, H.Y. Yu, B. Shin, S. Lee, J.H. Park, Extremely low contact resistance on graphene through n-type doping and edge contact design, Adv. Mater. 28 (2016) 864—870, https://doi.org/10.1002/adma.201503715.

[25] J.T. Smith, A.D. Franklin, D.B. Farmer, C.D. Dimitrakopoulos, Reducing contact resistance in graphene devices through contact area patterning, ACS Nano 7 (2013) 3661—3667, https://doi.org/10.1021/nn400671z.

[26] X. Yan, K. Jia, Y. Su, Y. Ma, J. Luo, H. Zhu, Y. Wei, Edge-contact formed by oxygen plasma and rapid thermal annealing to improve metal-graphene contact resistance, ECS J. Solid State Sci. Technol. 7 (2018) M11—M15, https://doi.org/10.1149/2.0251802jss.

[27] L. Wei, Y. Liang, D. Yu, L. Peng, K.P. Pernstich, T. Shen, A.R. Hight Walker, G. Cheng, C.A. Hacker, C.A. Richter, Q. Li, D.J. Gundlach, X. Liang, Ultraviolet/ozone treatment to reduce metal-graphene contact resistance, Appl. Phys. Lett. 102 (2013), https://doi.org/10.1063/1.4804643.

[28] G. Liu, S. Rumyantsev, M. Shur, A.A. Balandin, Graphene thickness-graded transistors with reduced electronic noise, Appl. Phys. Lett. 100 (2012), https://doi.org/10.1063/1.3676277.

[29] W. Li, C.A. Hacker, G. Cheng, Y. Liang, B. Tian, A.R. Hight Walker, C.A. Richter, D.J. Gundlach, X. Liang, L. Peng, Highly reproducible and reliable metal/graphene contact by ultraviolet-ozone treatment, J. Appl. Phys. 115 (2014), https://doi.org/10.1063/1.4868897.

[30] G. Liu, S. Rumyantsev, M. Shur, A.A. Balandin, Graphene Thickness-Graded Transistors with Reduced Low-Frequency 1/f Noise, (n.d.).

[31] G. Liu, S. Rumyantsev, M.S. Shur, A.A. Balandin, Origin of 1/f noise in graphene multilayers: surface vs. volume, Appl, Phys. Lett. 102 (2013), https://doi.org/10.1063/1.4794843.

[32] G. Xu, C.M. Torres, Y. Zhang, F. Liu, E.B. Song, M. Wang, Y. Zhou, C. Zeng, K.L. Wang, Effect of spatial charge inhomogeneity on 1/f noise behavior in graphene, Nano Lett. 10 (2010) 3312—3317, https://doi.org/10.1021/nl100985z.

[33] Y. Zhang, E.E. Mendez, D. Xu, Mobility-Dependent Low-Frequency Noise in Graphene Field-E Ff Ect Transistors, 2011, pp. 8124—8130.

[34] A.K.M. Newaz, Y.S. Puzyrev, B. Wang, S.T. Pantelides, K.I. Bolotin, Probing charge scattering mechanisms in suspended graphene by varying its dielectric environment, Nat. Commun. 3 (2012) 734—736, https://doi.org/10.1038/ncomms1740.

[35] S. Chatoor, I. Heller, J.B. Oostinga, A.F. Morpurgo, S.G. Lemay, C. Dekker, J. Männik, M.A.G. Zevenbergen, Charge noise in graphene transistors, Nano Lett. 10 (2010) 1563—1567, https://doi.org/10.1021/nl903665g.

[36] C. Hébert, E. Masvidal-Codina, A. Suarez-Perez, A.B. Calia, G. Piret, R. Garcia-Cortadella, X. Illa, E. Del Corro Garcia, J.M. De la Cruz Sanchez, D.V. Casals, E. Prats-Alfonso, J. Bousquet, P. Godignon, B. Yvert, R. Villa, M.V. Sanchez-Vives, A. Guimerà-Brunet, J.A. Garrido, Flexible graphene solution-gated field-effect transistors: efficient transducers for micro-electrocorticography, Adv. Funct. Mater. 28 (2018) 1—15, https://doi.org/10.1002/adfm.201703976.

[37] E. Masvidal-Codina, X. Illa, M. Dasilva, A.B. Calia, T. Dragojević, E.E. Vidal-Rosas, E. Prats-Alfonso, J. Martínez-Aguilar, J.M. De la Cruz, R. Garcia-Cortadella, P. Godignon, G. Rius, A. Camassa, E. Del Corro, J. Bousquet, C. Hébert,

T. Durduran, R. Villa, M.V. Sanchez-Vives, J.A. Garrido, A. Guimerà-Brunet, High-resolution mapping of infraslow cortical brain activity enabled by graphene microtransistors, Nat. Mater. 18 (2019) 280–288, https://doi.org/10.1038/s41563-018-0249-4.

[38] G.H. Ryu, J. Lee, D. Kang, H.J. Jo, H.S. Shin, Z. Lee, Effects of Dry Oxidation Treatments on Monolayer Graphene, 2012, pp. 1–10.

[39] N. Leconte, J. Moser, P. Ordejón, H. Tao, A. Lherbier, A. Bachtold, F. Alsina, C.M. Sotomayor Torres, J.C. Charlier, S. Roche, Damaging graphene with ozone treatment: a chemically tunable metal - insulator transition, ACS Nano 4 (2010) 4033–4038, https://doi.org/10.1021/nn100537z.

[42] M. Seifert, J.E.B. Vargas, M. Bobinger, M. Sachsenhauser, A.W. Cummings, S. Roche, J.A. Garrido, Role of grain boundaries in tailoring electronic properties of polycrystalline graphene by chemical functionalization, 2D Mater. 2 (2015) 1–10, https://doi.org/10.1088/2053-1583/2/2/024008.

[43] A. Eckmann, A. Felten, A. Mishchenko, L. Britnell, R. Krupke, K.S. Novoselov, C. Casiraghi, Probing the nature of defects in graphene by Raman spectroscopy, Nano Lett. 12 (2012) 3925–3930, https://doi.org/10.1021/nl300901a.

[44] Y. Matsuda, W.Q. Deng, W.A. Goddard, Contact resistance for "end-contacted" metal-graphene and metal-nanotube interfaces from quantum mechanics, J. Phys. Chem. C 114 (2010) 17845–17850, https://doi.org/10.1021/jp806437y.

[45] W.S. Leong, H. Gong, J.T.L. Thong, Low-contact-resistance graphene, ACS Nano (2014), https://doi.org/10.1021/nn405834b.

[46] H. Yu, A. Kutana, B.I. Yakobson, Carrier delocalization in two-dimensional coplanar p-n junctions of graphene and metal dichalcogenides, Nano Lett. 16 (2016) 5032–5036, https://doi.org/10.1021/acs.nanolett.6b01822.

[47] P. Zhang, Y.Y. Lau, R.M. Gilgenbach, Analysis of current crowding in thin film contacts from exact field solution, J. Phys. D Appl. Phys. 48 (2015) 475501, https://doi.org/10.1088/0022-3727/48/47/475501.

[48] D.C. Kim, D.Y. Jeon, H.J. Chung, Y. Woo, J.K. Shin, S. Seo, The structural and electrical evolution of graphene by oxygen plasma-induced disorder, Nanotechnology 20 (2009), https://doi.org/10.1088/0957-4484/20/37/375703.

A.2 Multiplexed neural sensor array of graphene solution-gated field-effect transistors

Here, the realization of time-domain multiplexed (TDM) data readout of a 8x8 μ-ECoG-array of gSGFETs is being presented. The performance and uniformity of the probe technology is being assessed and the signal reconstruction scheme described. Limitations regarding scalability due to the transient response and intersite crosstalk are discussed and the recording fidelity of the multiplexed acquisition mode is found to be equivalent to the one of the regular non-multiplexed acquisition. Finally, the in-vivo assessment of the multiplexing gSGFET array certifies high sensitivity to neural activity across a broad frequency window and compares favourably with competing state-of-the-art technologies.

Multiplexed Neural Sensor Array of Graphene Solution-Gated Field-Effect Transistors

Nathan Schaefer[1,2], Ramon Garcia-Cortadella[1,2], Javier Martínez-Aguilar[3,4], Gerrit Schwesig[5], Xavi Illa[3,4], Ana Moya Lara[3,4], Sara Santiago[6], Clement Hébert[7], Gonzalo Guirado[6], Rosa Villa[3,4], Anton Sirota[5], Anton Guimerà-Brunet[3,4] and Jose A. Garrido[1,8]

[1]Catalan Institute of Nanoscience and Nanotechnology (ICN2), CSIC and the Barcelona Institute of Science and Technology, Campus UAB, Bellaterra, Spain
[2]Departament d'Enginyeria Electrònica, Escola d'Enginyeria, Universitat Autònoma de Barcelona, Bellaterra, Spain
[3]Instituto de Microelectrónica de Barcelona IMB-CNM (CSIC), Esfera UAB, Bellaterra, Spain
[4]Centro de Investigación Biomédica en Red en Bioingeniería, Biomateriales y Nanomedicina (CIBER-BBN), Madrid, Spain
[5]Bernstein Center for Computational Neuroscience, Ludwig-Maximilians-University Munich, Planegg-Martinsried, Germany
[6]Departament de Química, Universitat Autònoma de Barcelona, Bellaterra, Barcelona, Spain
[7]Inserm and Université Grenoble Alpes, Saint Martin d'Hères, France
[8]ICREA, Barcelona, Spain

E-mail: joseantonio.garrido@icn2.cat

Abstract

Electrocorticography (ECoG) is a well-established technique to monitor electrophysiological activity from the surface of the brain and has proved crucial for the current generation of neural prostheses and brain-computer interfaces. However, existing ECoG technologies still fail to provide the resolution necessary to accurately map highly localized activity across large brain areas, due to the rapidly increasing size of connector footprint with sensor count. This work demonstrates the use of a flexible array of graphene solution-gated field-effect transistors (gSGFET), exploring the concept of multiplexed readout using an external switching matrix. This approach does not only allow for an increased sensor count, but due to the use of active sensing devices (i.e. transistors) over microelectrodes it makes additional buffer transistors redundant, which drastically eases the complexity of device fabrication on flexible substrates. The presented results pave the way for upscaling the gSGFET technology towards large-scale, high-density μECoG-arrays, eventually capable of resolving neural activity down to a single neuron level, while simultaneously mapping large brain regions.

Keywords: Multiplexed μECoGs, graphene solution-gated field-effect transistor, flexible probes, neurosensing

1. Introduction

Exploration of novel materials and improved micro- and nano-fabrication techniques are bringing up a new class of brain-computer interfaces (BMIs) which promise to revolutionize neuroprosthetics and unveil the underlying vast functionalities of the brain. Impressive breakthroughs have been recently achieved in motor control rehabilitation, understanding the mechanisms for learning and formation of memory, treating neuropsychiatric disorders (e.g. depression) and synthesizing audible speech using machine learning algorithms, emphasizing the immense potential BMIs have.[1–10] While the presented capabilities to interface with the brain are already very impressive, they mostly rely on relatively simple epi-cortical electrode arrays with low number of recording sites and large inter-site spacing, and are unsuitable for long chronic implantation. Higher cognitive functions do typically arise from a complex interplay of activity in several brain regions at once, therefore a detailed analysis of the neural activity underlying such functions would require sensor arrays recording from all involved areas with high local resolution in each of them. Current commercially available neural sensor arrays fail to provide the high sensor counts necessary for such endeavor, mostly due to the technologic challenge of excessive wiring with increasing array size, which could only

84

be overcome by the employment of multiplexed read-out circuitry. Multiplexing strategies are not new to the field of neuro-sensing and have previously been used as a versatile tool to manage large amounts of recording sites. Most of the emerged technologies are based on a CMOS-compatible monolithic integration of recording electrodes and read-out electronics to minimize connection distance for preserving signal integrity and maximizing the density of recording sites. Using rigid silicon substrates, however, restricts such concepts to applications in which device flexibility is expendable such as depth-probes or MEAs for ex-vivo recordings.[11–14] Yet, considering the extensive damage rigid depth-probes cause to the brain tissue, sets a clear limitation to the amount of insertable shanks and thus the simultaneously mappable brain regions. Here, electrocorticography offers a minimally invasive alternative with clear advantage on sensor resolution over large areas by using flexible μECoG arrays to record from the surface of the cortex.[15] Still, so far only very few examples of multiplexed μECoG arrays have been realized, due to the scarcity of durable materials for low-noise, high-performance switches compatible with flexible substrates as well as the high level of complexity such device fabrication requires. An example is the work of Rodgers which utilizes a combination of buffer and addressing transistor (ultrathin Si) to process the signals of an array of 360 passive platinum electrodes.[16, 17] Using passive elements, i.e. electrodes, as sensors requires the implementation of an additional transducer (buffer transistor) to decouple the electrode from the read-out circuitry, which otherwise would lead to load currents affecting the electrodes performance. This additional complexity can be avoided by directly using active elements i.e. transistors to interface with the brain. Such approach has recently been explored for organic electrochemical transistors (OECTs) with the conductive polymer poly(3,4-ethylenedioxythiophene):poly(styrenesulfonate) (PEDOT:PSS) as channel material.[18, 19] However, it has only been used to selectively address different sites, but not yet to actually acquire signals in multiplexed operation, which might be due to the relatively low carrier mobility in PEDOT:PSS prohibiting the rapid switching needed for multiplexing.

As the brain consists of corrugated soft tissue moving at every heartbeat, highly flexible probes are imperative to create intimate interfaces for best signal quality and to avoid gradual cicatrizing of the neural tissue. In this work, we present flexible multiplexed μ-ECoG arrays based on active sensing devices, namely graphene solution-gated field-effect transistors (gSGFETs). The gSFGET has emerged as one of the most promising technologies for brain-machine interfaces (BMIs) as it provides essential properties such as

biocompatibility, chemical stability, mechanical flexibility and high signal-to-noise ratio.[20, 21] In particular, it has shown great potential for application in μ-ECoG arrays with its high sensitivity over a broad frequency range (0.001Hz up to 10kHz), making it an efficient transducer of both infra-slow and fast neural activity.[20, 22] While the gSGFETs suitability to provide high-quality recordings has already been proven for up to 16 recording sites in previous publications, its potential has never been evaluated for high-density arrays of large sensor count. Graphene is commonly considering as an ideal material for high-frequency application, as its reported mobilities up to 350 000 $cm^2V^{-1}s^{-1}$ for CVD grown graphene, can easily surpass materials such as Si and PEDOT:PSS with respective mobilities of 1400 $cm^2V^{-1}s^{-1}$ and 0.01 $cm^2V^{-1}s^{-1}$, which makes it an interesting candidate to consider for multiplexed devices.[23, 24] Moreover, we demonstrate that by using active sensing devices, the integration of multiplexing circuitry, i.e. buffer and switching transistors, is unnecessary, thus drastically easing the complexity of fabricating flexible multiplexed sensor arrays.

2. Methods

2.1 Probe fabrication

In a first step 10um thick biocompatible Polyimide (PI-2611 HD MicroSystems) was spun on 4'' Si/SiO2 support wafers and cured under nitrogen atmosphere at 350 °C. The perpendicular metal lines of the array (columns/ rows) were patterned in two standard lift-off steps (negative photoresist AZ5214E, Clariant, Germany) with the metal deposited by e-beam evaporation (30nm Ti/ 300nm Au, 10nm Ti/ 100nm Au) and separated by a 2 μm PI spacer layer. Interconnecting via-holes through the spacer layer were etched by oxygen plasma using a photolithographically defined protective aluminum mask (AZ5214E, 300nm Al). Then, single layer graphene, grown and transferred by Graphenea, is patterned by photolithography (H6512 photoresist) and etched by oxygen-based reactive ion etching (100W for 1min) to form the transistor channel area. A third metal layer (20nm Ni/ 200nm Au) is added to form sandwich contacts improving the gSGFET's durability and lowering its contact resistance due to work function matching. A subsequent thermal annealing step at 300°C in ultra-high vacuum has been found to reduce surface contamination from photoresist residues and improving the conformality of the Ni-graphene interface, thus improving contact resistance and device performance. To passivate the metal leads, a 2 μm thick layer of SU8 epoxy photoresist (SU-8 2005 MicroChem) was deposited, leaving open windows in the channel regions to allow a direct electrolyte graphene interface. In a final step, the polyimide

2

was structured by deep reactive ion etching using a photoresist etching mask (AZ9260, Clariant) and the flexible probes were mechanical peeled from the support wafer.

2.2 Characterization and multiplexing setup

Custom-build electronics were used for bias control and to convert the drain source current signal into voltage by a transimpedance amplifier (10k gain). The voltage signal was split into DC (frequency < 0.1 Hz) and AC (0.1 Hz < frequency > 5 kHz) components. The AC signal is amplified by an additional factor of 100 for the noise evaluation. The voltage read out was done by a standard data acquisition system (National Instruments DAQ-Card, USB-6363). For the multiplexed data acquisition, a similar system was used as for the probe characterization, however the gain of the AC stage was reduced by a factor of 10 to prevent saturation of the amplifier's dynamic range due to mismatch in transistor resistance. The digital output lines were used to address the n-type MOSFET switching matrix by applying either +5V for ON- and 0V for OFF-state. All software to control the DAQ-Card and handle data acquisition is based on self-built python code.

2.3 In-vivo experiments

Long Evans rats (Charles River) were kept under standard conditions (room temperature $22 \pm 2\,°C$, 12:12 h light–dark cycle, lights on at 10:00). Food and water were provided ad libitum. All experiments were performed in accordance with the European Union Directive 2010/63/EU as well as the German Law for Protection of Animals (TierSchG) and approved by the local authorities (ROB-55.2-2532.Vet_02-16-170). Three adult rats (2 males, 1 female), 3-8 month of age, weighing in the range of 400-600g were used in this study. In preparation of electrophysiological measurements, they were deeply anaesthetized with MMF (Midazolam 2mg/kg), Medetomidin 0.15 mg/kg, Fentanyl 0.005 mg/kg) and supplemented after 1h with Isoflurane 0.5%-1% and Metamizol at 110 mg/kg. After subcutaneous infiltration with Bupivacain the skin above the cranium was incised and the dorsal skull surface exposed. Craniotomies were performed bilaterally, with a maximum width of 5 mm and extending anterior-posteriorly between +2 mm and -8mm with respect to bregma. The dura mater was opened and carefully resected. The craniotomies were subsequently covered with prepolymerized PDMS (Sylgard 184, Dow Corning) with mixing ratio 1:10 and fastened with Vetbond (3M). In one rat an additional 1x1 mm craniotomy was performed over the cerebellum for the placement of a reference wire. For placement of the recording arrays the PDMS covers were flapped open partially and the gSGFET array was placed on the right hemisphere while the NeuroNexus array (E32-600-10-100) was symmetrically positioned on the left hemisphere, (between ca -7 to -3 mm from bregma) each partially covering the primary visual cortex. Subsequently the PDMS covers were flapped back to cover arrays and craniotomies. A reference wire (Ag/Ag-Cl) was inserted either in the cerebellar craniotomy (n=1) or temporal muscle (n=2). Data from the NeuroNexus array was acquired at 25 kHz using the eCube recording system (WhiteMatter LLC) while data from the gSGFET was acquired using custom build electronics described in the previous section. Anesthesia was kept at 0.5% isoflurane during the recordings of spontaneous activity and cortical spreading depression (CSD) and 2% isoflurane for the recording of optically evoked activity with reduced spontaneous activity. The CSD event was triggered by application of 1uL KCl (3 mMol) with a glass-micropipette and Nanoject II injection device (Drummond Scientific) at ca 4 mm anterior to bregma, approximately 7 mm anterior to the closest site on the recording array. The optically evoked response was triggered by a contralaterally placed blue LED in front of the left eye, which delivered 100 msec light pulses every 5 seconds.

3. Results and discussion

3.1 Device performance and multiplexing methodology

Scalable thin-film technology of 8x8 gSGFET sensor arrays was fabricated on 7um-thick flexible polyimide (PI) using 4-inch support wafers. The layout of the probe can be seen in Figure 1a and consists of a stack of two metal layers constructing the perpendicular lines of the sensor grid with a separating PI layer in between. The 64 gSGFET sensors have single-layer graphene channels of 50μm x 50μm dimension and 400μm inter-site separation (detailed description of probe fabrication in experimental section). A picture of the final probe, after releasing it from the Si support wafer is shown in Figure 1c. In contrast to their solid-state counterparts, solution-gated transistors are being modulated through the creation of a charge double layer at the interface between transistor channel and an electrolyte solution. Potential fluctuations in the surroundings (e.g. neural activity) can modulate this double layer and result, in turn, in a shift of the Fermi level of the channel material, which is detectable as a current fluctuation. Graphene's ability to create a stable interface with aqueous solutions in combination with its high transconductance, resulting from its large interfacial capacitance and carrier mobility, makes the gSGFET an ideal device for bio-sensing.[20–22, 25–28]
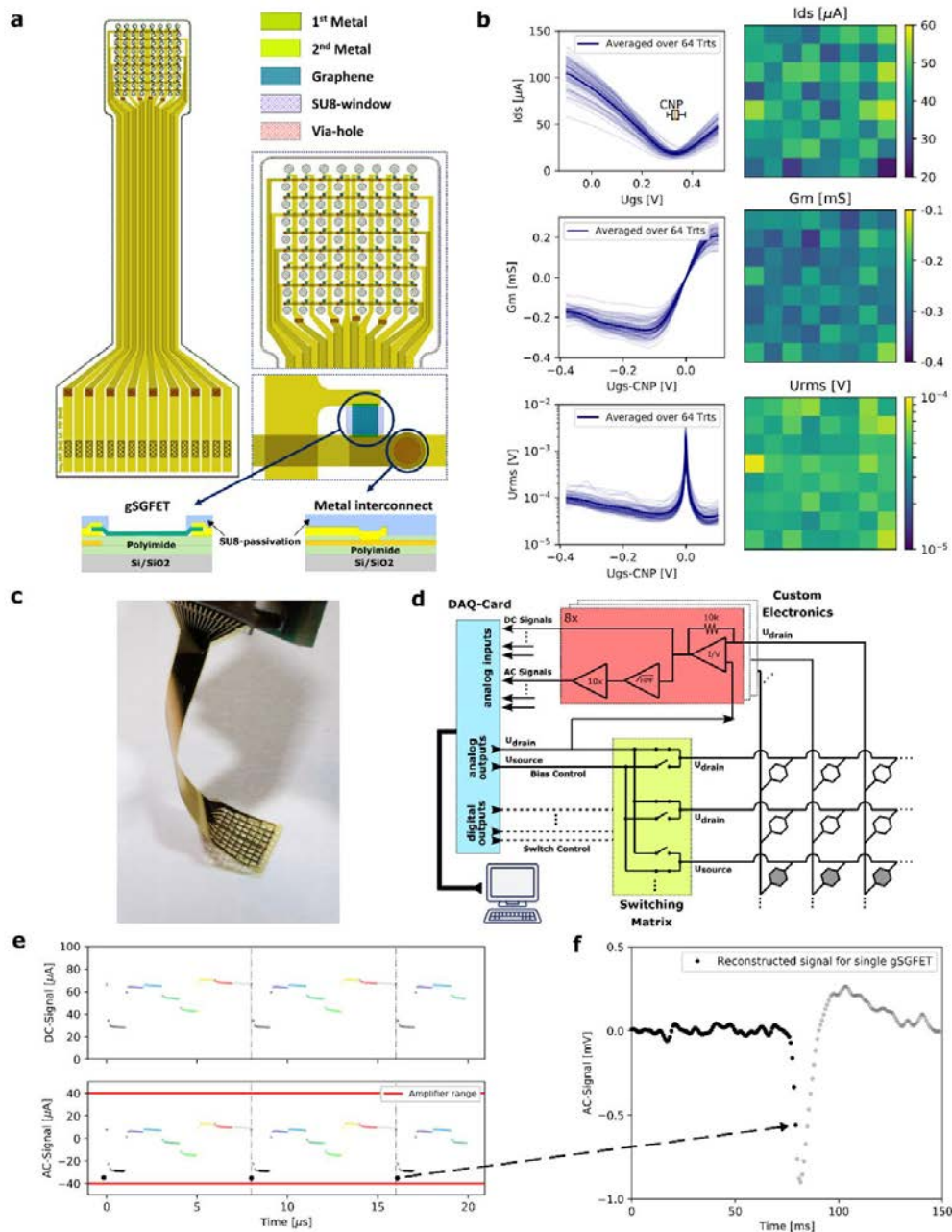
Figure 1. Multiplexed gSGFET μECoG-array: a. Layout and cross section of flexible ECoG array with 64 gSGFETs showing the grid construction with two metal layer and tapered via-holes (Figure S1 in supporting information) crossing the PI interlayer. **b.** gSGFET's transfer curve showing the change of drain-source current with applied gate bias (I_{ds}-U_{gs}, measured at U_{ds}=100mV), its transconductance (G_m-U_{gs}) and the device's equivalent gate noise (U_{rms}-V_{gs}). Also, the respective distribution of each parameter at peak G_m (bias point yielding highest absolute transconductance) across the array is being shown in the adjacent color map. **c.** Picture of flexible probe after release from Si support wafer. **d.** Schematic of discrete multiplexing setup using a DAQ-card for bias control and read-out (blue) and a custom-build PCB board for switching (yellow), filtering and current-to-voltage conversion (red). **e.** Acquired DC and AC raw signal for one column showing eight distinct current levels corresponding to the transistors in each row, which repeat for every cycle (grey dashed line). Due to the high gain (100k) applied to the AC component of the signal, the dynamic amplifier range sets a limit to the allowable current mismatch between devices, before amplifier saturation occurs (solid red line). **f.** From the 10 data points taken for each transistor per cycle, an average value of the last 5 points is taken, to yield one sample in the final reconstructed signal for each sensor.

87

Figure 1b shows a performance and homogeneity assessment of the gSGFET array. The transfer curve, namely the change of drain-source current I_{ds} with applied gate bias U_{gs} is presented as an averaged value and for all 64 individual devices, with the boxplot indicating the variation of charge neutrality point (CNP). Also, the transconductance Gm is shown (normalized to each transistor's CNP), which is defined as the first derivative of I_{ds} over U_{gs}. Of crucial importance to any sort of sensor array is the signal-to-noise ratio (SNR) and its homogeneity across recording sites. The SNR in the gSGFET is mainly affected by two physical parameters: the transconductance, which sets the transistor's sensitivity to signal fluctuations at the gate and the intrinsic device noise integrated over the relevant frequency range I_{rms}. A common figure of merit to quantify the gSGFET's SNR is the U_{rms} value (I_{rms}/G_m), which represents the equivalent gate noise below which signals are undetectable. As can be seen, the U_{rms} values of the gSGFETs on the array, are around 40 μV_{rms} (for the frequency band from 1Hz to 100Hz), which allows the detection of local field potentials (typical amplitude above 100μV) from the surface of the brain. The distribution across the array of each parameter (I_{ds}, G_m, U_{rms}), calculated at the bias point of highest absolute transconductance (peak-G_m), where the device shows lowest U_{rms}, is shown in the corresponding color maps. With yields above 90% on a 4-inch wafer (each wafer carrying 14 probes) and large, evenly distributed SNR across all recording sites, the gSGFET technology shows high maturity and homogeneity, which is a key requirement to enable multiplexed addressing schemes.

The most common type of multiplexing is time-division multiplexing (TDM), which refers to a technique of sequentially addressing the columns of a sensor array, while continuously measuring from its rows. Such addressing is normally being achieved by switches, which can be placed either directly on the array or externally.[14, 17, 18] While placing the switches directly on the array has the advantage of reducing inter-site crosstalk it requires complex fabrication of flexible switching technology, as previously mentioned.[17] Complementing arrays of passive sensing elements (i.e. electrodes) with an external addressing configuration is challenging, as their recorded voltage signal is prone to pick up noise; if the preamplifier is placed far from the electrode, additional buffer transistors are required to convert the signal into current and feed it to the read-out circuitry. The use of active sensing elements (i.e. transistors) offers a great benefit here, as they feature an intrinsic voltage-to-current conversion, making the recorded signal more robust to noise. A schematic representation of the addressing and acquisition methodology is shown in Figure 1d. For this purpose, a custom-build PCB board consisting of two main functional blocks has been developed using discrete electronics. One functional block performs the filtering and amplification of the simultaneously acquired AC and DC signals; the other block selects the row to which the bias difference is applied to, using the external switching matrix for addressing. Figure 1e illustrates the acquired AC and DC raw input signals for a column of eight gSGFETs and how they can subsequently be used to reconstruct the original signal at each site (Figure 1f). Resistance mismatch between different transistors leads to current jumps when switching between transistors, which results in the different DC levels in the acquired signal (each gSGFET corresponds to one color in Figure 1e). The vertical dashed grey line in Figure 1e indicates the point at which all eight rows were addressed and a new readout cycle begins. At each site a total of 10 points is taken at 100 kHz sampling speed; we discard the first 5 to avoid any switching artefacts and average the rest to a single data point resulting in 1.25 kHz effective sampling rate. It should be here emphasized that array homogeneity carries an additional importance in multiplexed operation owing to two reasons. First, the trade-off between applicable AC signal gain and transistor resistance mismatch; as previously mentioned, current jumps can exceed the dynamic range of the amplifier (indicated in Figure 1e) leading to saturation and signal loss. Second, the switching artefacts scale with the level of mismatch between devices, requiring longer stabilization times before reliable data points can be collected.

3.2 Scalability and in-vitro assessment

With the goal of creating a high-density, large-scale sensor array, an important discussion to undertake is the one on scalability of this technology. The most important aspects to consider here are the transient response of the transistor, which limits the achievable switching speeds, and the increase of inter-site crosstalk with array size and track resistance. To obtain distortion-free, high-quality recordings in multiplexed operation, it is important to allow sufficient stabilization time after switching, for the transistor to adjust to the changed drain-source bias conditions. This stabilization time is device specific and generally scales with channel length and carrier mobility. Owing to the high carrier mobility of graphene, which is for our devices 1000-2000 $cm^2V^{-1}s^{-1}$ but can potentially reach up to 350 000 $cm^2V^{-1}s^{-1}$, the transient response of the gSGFET is extremely short (Figure 2a) compared to other technologies (e.g. transistors based on silicon or conducting polymers).[23] The ON-state is reached before 1μs, which is the time resolution of the used measurement equipment (NI DAQ-Card X-Series 6363); for a channel length of 50μm and a carrier mobility of 2000 $cm^2V^{-1}s^{-1}$ the actual stabilization time from a time-of-flight

estimation is expected to be in the range of hundred nanoseconds. Such fast device stabilization can eventually allow switching speeds beyond 1MHz (our current configuration is limited by the electronics to 10kHz). Thus, much larger arrays could be operated this way while maintaining enough sampling speed (>10kHz) to record even high frequency activity such as spikes. Due to the solution-gated nature of the device, a small drift occurs during the ON-state of the device which is tentatively associated to the migration of ions when the bias conditions in the channel change under switching. This phenomenon happens at a much slower time scale due to the low ionic mobility; however, it does only create a minor inaccuracy in the measured DC current and does not impact the AC recordings.

As previously stated, the use of external switches bears the disadvantage of not allowing to cut the connections to non-addressed sensors within the array, which leads to the so-called crosstalk. The lack of on-site switches opens alternative current pathways leading to current contribution from adjacent sites which carry signals from the respective gates and are wrongly attributed to the measured sensor (see Figure 2b). Such crosstalk can be strongly reduced and, in the ideal case of vanishing track resistance, even fully suppressed by setting the bias point of the non-addressed rows to the same voltage as the data lines, thus preventing any current flow through non-addressed lines.[18] However, in real-world applications the issue of finite track resistance cannot be completely avoided, as the requirements of high sensor density and probe flexibility limit the allowed width and thickness of the metal lines. The presence of these additional resistances create local potential drops, driving current through otherwise suppressed pathways whose amplitude depends on the ratio between track resistance (R_{track}) and transistor resistance (R_{gSGFET}) as well as the number n of columns and rows in the array. To quantify crosstalk in the gSGFET array experimentally, lateral Ag-gates and confined pads of solid polyelectrolyte were placed at each gSGFET of a 2x2 array by means of inkjet printing (Figure 2c). This approach allows for selective gate control, which is not possible in a shared liquid electrolyte. Figure 2d shows the measured signal at each of the transistors, with a test signal (sine wave of 10Hz frequency and 30mV amplitude) only being applied to one of them (black circle in Figure 2c). Sensors on the same column (red curve in Figure 2d) or row (dark-red curve in Figure 2d) as the applied signal are the ones with the largest impact of crosstalk, showing a

crosstalk level of -40dB at peak transconductance compared to the signal amplitude.

Diagonally placed sensors (orange curve in Figure 2d) are much less affected; however, in the latter case the exact level of crosstalk cannot be extracted with accuracy because the signal lies below the floor noise of the electronics. To validate this estimation of the crosstalk, we compared the experimental data with the results obtained from a PSpice simulation of a gSGFET array in which we used a standard p-type MOSFET element tailored to fit the gSGFET's transfer curve (Figure S2a-b in supporting information). Figure 2e shows the aggregated crosstalk on a single site depending on the track resistance and the array size, assuming identical signals on all remaining sites of the array which sum up to the total crosstalk value. The PSpice model validates the expected near-linear relation with both track resistance and array size. For a 2x2 array with 20Ω track resistance and a gSGFET resistance of 1,25kΩ, both the experiment and the simulation model yield a crosstalk of -40dB. Extrapolating to an array of size 32x32 (1024 sensors), a crosstalk lower than -20dB can be obtained by reducing the track resistance below 5 Ω or by increasing the resistance of the gSGFET. Such track resistance reduction could be achieved by increasing metal track thickness, using higher number of stacked metal layers and, most importantly, relaxing constraints on probe dimensions. While the ECoG array in this work was designed for application in rodents, which imposes strict size restrictions due to the dimensions of the craniotomy, many other application (e.g. neural probes for large animals or humans) would loosen those significantly.

To validate the fidelity of the gSGFET recordings in the multiplexed operating mode, the recording quality must be compared to the one obtained in steady, non-multiplexed operation. For instance, the rapid switching between devices can potentially increase the noise or generate artefacts in the multiplexed operation mode. Figure 2f compares recordings of an artificially generated electrocardiogram signal (ME-W-SG, Multichannel Systems), containing components of different frequencies. The multiplexed and non-multiplexed representation of both test signals are nearly identical, suggesting that the rapid sequential addressing by the multiplexed mode does not generate any visible artefacts, neither in the low nor in the mid frequency band. The root-mean-square value of both recordings is also compared, showing equivalent SNR ratio (Figure 2g) in both acquisition modes.
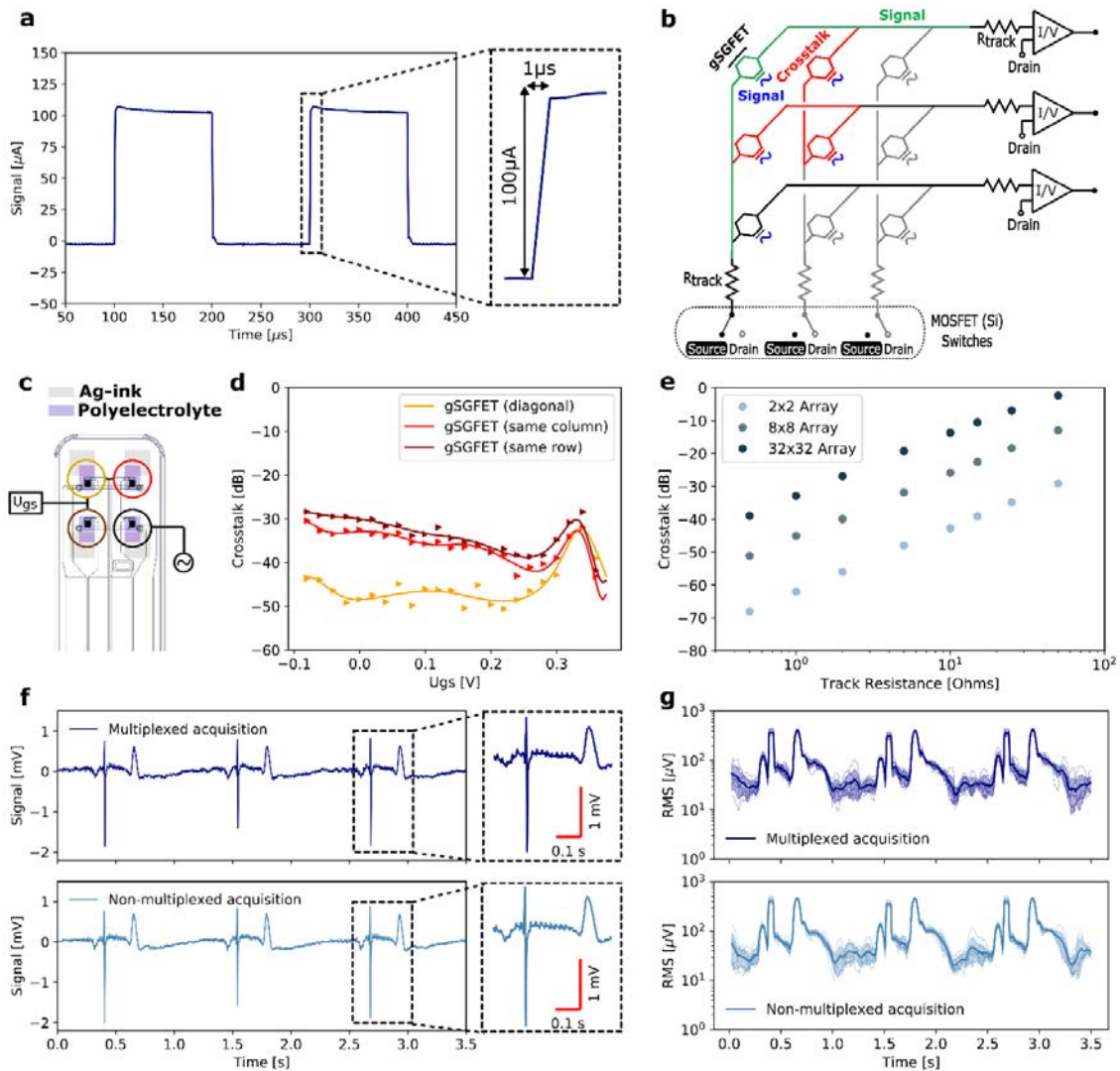
Figure 2. Scalability and in-vitro assessment: a. Transient response of gSGFET when switched between ON and OFF state, showing short stabilization time of the device. Response below 1μs cannot be resolved due to sampling rate limitation of the setup (1MHz). **b.** Origin of crosstalk in array without on-site switches and finite track resistance. Biasing to U_{drain} of non-addressed columns significantly decreases the amount of crosstalk. **c.** Location of measured gSGFETs on a 2x2 probe for crosstalk evaluation, utilizing inkjet printing to pattern confined gates consisting of Ag and polyelectrolyte pads. **d.** Crosstalk versus gate bias when applying a test signal (sinewave 30mV, 10Hz) to a single gSGFET and measuring the signal on each of the adjacent sensors. The devices in the same column and row as the one, to which the test signal is applied to, show a crosstalk of -40dB while the device on the diagonal shows crosstalk lower than -50dB (below floor noise of electronics). **e.** Simulated (PSpice) crosstalk for a 2x2, 8x8 and 32x32 arrays in dependence of the track resistance. The aggregated crosstalk value is presented assuming a superposition of identical signals on all but the probed sensor. **f.** Recordings of one gSGFET on the same 8x8 μECoG-array, acquired in either multiplexed or steady (non-multiplexed) acquisition. An artificial electrocardiogram signal was used to compare the fidelity of both acquisition modes. In both cases, the same averaging method was applied (cycles of 10 points, discarding first 5 points and averaging last 5 points), to ensure comparability. **g.** For each acquisition mode, the root-mean-square (RMS) value is calculated as the mean value of all 8 gSGFETs on one column, indicating the signal-to-noise ratio of the recorded signal.

90

3.3 In-vivo validation

Having confirmed the recording fidelity of the gSGFET in the multiplexed operation compared to the standard non-multiplexed acquisition mode, we demonstrate the unimpaired sensitivity of the multiplexed µECoG-array towards biological signals. Electrocortiography is primarily used to record local field potentials (LFPs) from the surface of the brain, which originate from spatio-temporal summation of transmembrane-currents generated by synaptic and active conductances, excluding the action potentials.[29, 30] The characteristic spectral content of the LFP signal reflects the time scale of network synchronization and ranges from <1Hz to hundreds of Hz. Figure 3a shows a time trace of spontaneous LFP activity in an anesthetized Long Evans rat, recorded in an acute in-vivo experiment using an array of gSGFETs operated in the multiplexed mode (more details in methods section). Under deep anaesthesia, such cortical LFP reflects slow oscillations that are highly coherent across the whole cortical mantle; indeed, no significant differences in signal shape can be seen across all the 64 sensors in the array.[31] To benchmark the recording capabilities of the gSGFET array against other state-of-the-art technologies, a NeuroNexus ECoG array (with 32 circular platinum electrodes of 100µm diameter) was simultaneously placed on the opposite hemisphere (Figure S3 in supporting information). Figure 3c-d show recordings and corresponding spectrograms from an electrode and a gSGFET, displaying the expected synchronicity in activity of both hemispheres. Filtering the signals from 0.1Hz to 200Hz (dark-blue and red curve in Figure 3c), a clear difference in signal shape can be noticed. This difference reflects the high-pass filter of the AC-coupled headstage used for passive ECoG recordings (see Experimental Section), which is necessary to prevent amplifier saturation due to drifts; also the high impedance of passive ECoG electrodes at low frequency leads to reduced gain in such signals, which results in an attenuation of the infraslow frequency content in the LFP signal.[22] Removing these low-frequency components from the gSGFET signal (green curve in Figure 3c), it is possible to validate that both technologies show very similar recordings of the LFP activity as can also be seen in the corresponding spectrograms.

Visually evoked LFP activity exhibits a well-defined spatial topography and thus can be used for validating the mapping

capabilities of the multiplexed gSGFET technology.[32] Figure 3b shows the averaged response over 10 consecutive evoked events recorded with an array of gSGFETs in the multiplexed mode. Visually evoked activity typically exhibits a clear response with a delay of 40 ms after both the ON- and OFF-switching of the stimulus (Figure 3e). The recordings show a main peak (ON response) lasting until 70 ms after the stimulation with and peak amplitude of 500 µV. Hence, signal shape and amplitude are in nice agreement with previously reported results of non-multiplexed gSGFETs.[20] Further, Figure 3f presents the spatial distribution of both amplitude and time-delay of the ON-peak. The earliest response is detected on the lower end of the array which represents sensors directly placed on the primary visual cortex (V1) where the activity originates, and spreads then radially towards other higher visual cortical areas. However, highest peak-amplitude is measured in the centre-left region (secondary visual cortex, V2) which likely reflects a different magnitude and proximity current dipole, that gives rise to the surface LFP (LGN input to LIV in V1 vs V1 input to L2/3 pyramidal cells in V2).[33]

In addition, to its capability to record LFPs, the gSGFETs exhibit a unique sensitivity towards slow and infra-slow (below 0.1Hz) signals, which in the case of passive electrode recordings are hidden by baseline drifts and the impedance-related loss of gain at low frequency.[22] In order to confirm that multiplexed acquisition preserves signal quality in this frequency band, we have investigated recordings of a cortical spreading depression (CSD). CSDs emerge due to a cellular depolarization of neurons and astrocytes which is associated to brain injury and migraines among others.[34] Here, the CSD was artificially triggered by injecting KCl into the cortex that caused a slowly propagating wave moving across the cortex. Figure 3g depicts the recording of a gSGFET in the array. The DC component of the signal shows the characteristic large shift of 15mV amplitude. The AC component and its corresponding spectrogram (Figure 3h) reveals a silencing of the high-frequency activity during the event, caused by the cellular depolarization and which is characteristic for the CSD. The maps below (Figure 3i) show the respective position of the depolarising wave at different times after KCL injection, moving from the top right to the bottom left at about 7mm per minute speed.
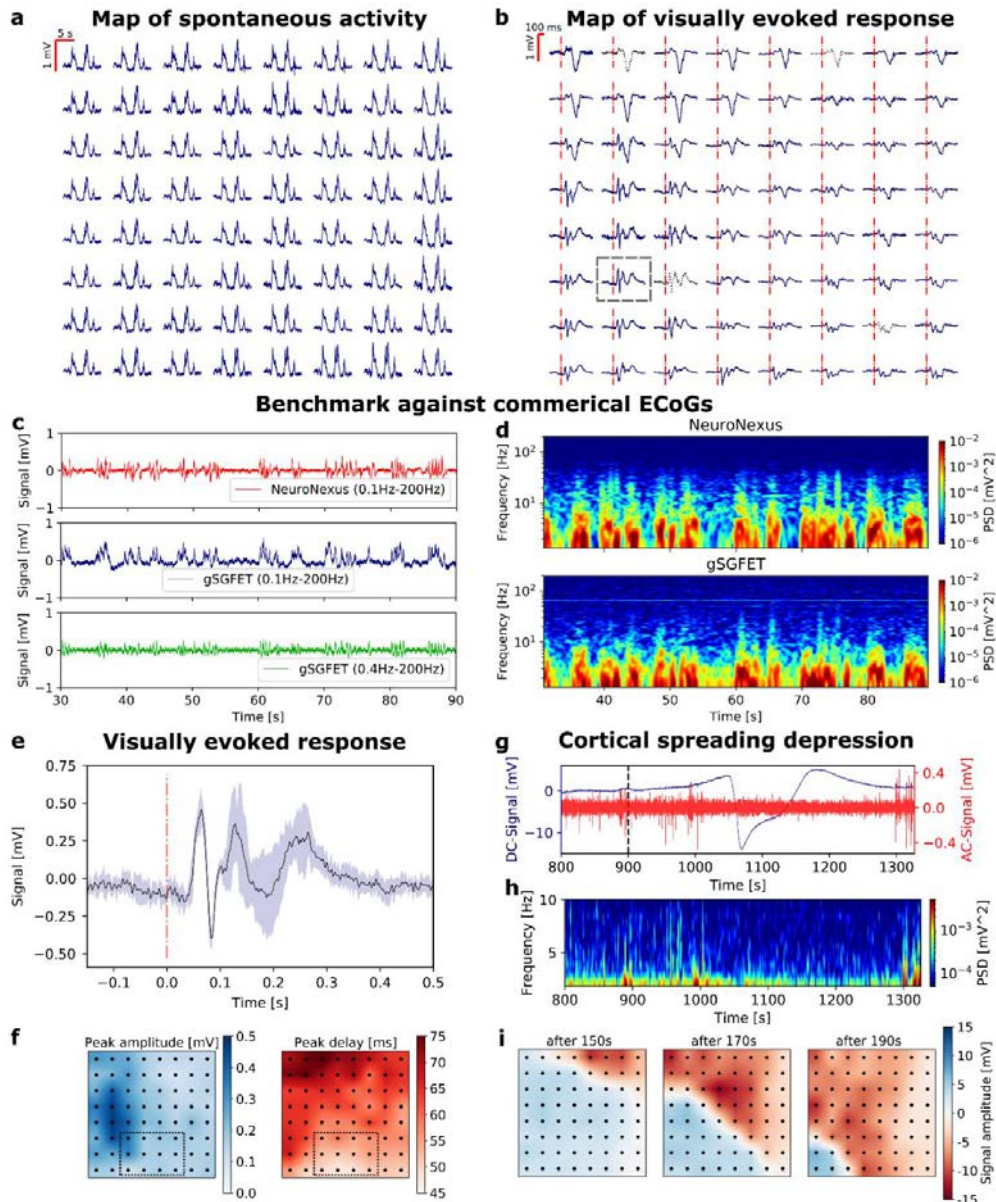
8

Figure 3. In-vivo validation of multiplexed gSGFET μECoG-array: a. Map of spontaneous LFP activity showing near identical shape across all sites. **b.** Map of visually evoked activity averaged over 10 consecutive events (dashed red line indicates timing of optical stimulus; dashed black curves are interpolated values from neighbouring sites for non-functioning sensors. **c.** Recording trace derived from AC-coupled passive ECoG-array (NeuroNexus, platinum electrode) as well as DC and AC-filtered gSGFET's. Note prominent infraslow oscillations (0.1-0.4Hz), which are not visible in the AC electrode recordings. **d.** Corresponding spectrograms of both, NeuroNexus and gSGFET recordings. **e.** Visually evoked response recorded on a single sensor (dashed grey box in Figure 3b), with an ON- and OFF-response of 50 ms delay and 500μV peak amplitude. **f.** Array maps displaying the distribution of amplitude and time-delay of the ON-peak response across all sites. While the shortest delay is measured for the sensors placed directly on the primary visual cortex (V1), the highest peak-amplitude is seen in the secondary visual cortex (V2). **g.** DC-signal (blue, lowpass-filtered below 20Hz) and AC signal (red, bandpass-filtered between 1-20Hz) of a single gSGFET during the cortical spreading depression (CSD). A strong DC shift of -15mV occurs simultaneously with a silencing of high-frequency activity, which is characteristic for a CSD. **h.** Corresponding spectrogram of CSD event to validate the silencing. **i.** Array map showing the propagating front of the spreading depolarization wave across the array from the right upper to the left lower corner.

4. Conclusion

This work demonstrates the compatibility of graphene solution-gated field-effect transistors (gSGFETs) with time-division multiplexed acquisition mode, utilizing a strongly simplified addressing concept to overcome the hurdle of excessively complex device fabrication. The superiority of graphene over silicon and organic polymers for high-speed applications makes the gSGFET an ideal device for multiplexed sensor arrays. In-vitro and in-vivo assessments confirm the fidelity of broad-band signal representation (infra-slow oscillations and local field potentials) in multiplexed operation, with signal quality comparable to the state-of-the-art of commercially available neuro-sensors. Consequently, next to their potential as efficient transducers of neural activity, gSGFETs show great promise as a building block for multiplexed brain-machine interfaces of high sensor count. Thus, this work represents an important cornerstone in the development of large-scale, flexible gSGFET μECOG arrays capable of providing high resolution mappings of neural activity to control neuroprosthetics and to help exploring the operation and functionalities of the brain.

Acknowledgements

References

1. Lee B, Kramer D, Salas MA, Kellis S, Brown D, Dobreva T, Klaes C, Heck C, Liu C, Andersen RA (2018) Engineering artificial somatosensation through cortical stimulation in humans. Front Syst Neurosci 12:1–11

2. Ajiboye AB, Willett FR, Young DR, et al (2017) Restoration of reaching and grasping movements through brain-controlled muscle stimulation in a person with tetraplegia: a proof-of-concept demonstration. Lancet 389:1821–1830

3. Moxon KA, Foffani G (2015) Brain-machine interfaces beyond neuroprosthetics. Neuron 86:55–67

4. Orsborn AL, Pesaran B (2017) Parsing learning in networks using brain–machine interfaces. Curr Opin Neurobiol 46:76–83

5. Clancy KB, Koralek AC, Costa RM, Feldman DE, Carmena JM (2014) Volitional modulation of optically recorded calcium signals during neuroprosthetic learning. Nat Neurosci 17:807–809

6. Shanechi MM (2019) Brain–machine interfaces from motor to mood. Nat Neurosci 22:1554–1564

7. Mayberg HS, Lozano AM, Voon V, Mcneely HE, Seminowicz D, Hamani C, Schwalb JM, Kennedy SH (2005) Deep Brain Stimulation for Treatment-Resistant Depression ing electrical stimulation of the subgenual cingulate. Neuron 45:651–660

8. Holtzheimer PE, Husain MM, Lisanby SH, et al (2017) Subcallosal cingulate deep brain stimulation for treatment-resistant depression: a multisite, randomised, sham-controlled trial. The Lancet Psychiatry 4:839–849

9. Dagamseh AMK, Wiegerink RJ, Lammerink TSJ, Krijnen GJM (2012) Towards a high-resolution flow camera using artificial hair sensor arrays for flow pattern observations. Bioinspiration and Biomimetics. https://doi.org/10.1088/1748-3182/7/4/046009

10. Anumanchipalli GK, Chartier J, Chang EF (2019) Speech synthesis from neural decoding of spoken sentences. Nature 568:493–498

11. Raducanu BC, Yazicioglu RF, Lopez CM, et al (2016) Time multiplexed active neural probe with 678 parallel recording sites. Eur Solid-State Device Res Conf 2016-Octob:385–388

12. Jun JJ, Steinmetz NA, Siegle JH, et al (2017) Fully integrated silicon probes for high-density recording of neural activity. Nature 551:232–236

13. Angotzi GN, Boi F, Lecomte A, Miele E, Malerba M, Zucca S, Casile A, Berdondini L (2019) SiNAPS: An implantable active pixel sensor CMOS-probe for simultaneous large-scale neural recordings. Biosens Bioelectron 126:355–364

14. Eversmann B, Jenkner M, Hofmann F, et al (2003) A 128 x 128 CMOS Biosensor Array for Extracellular\rRecording of Neural Activity. Ieee J Solid-State Circuits, 38:2306–2317

15. Khodagholy D, Gelinas JN, Thesen T, Doyle W, Devinsky O, Malliaras GG, Buzsáki G (2015) NeuroGrid: Recording action potentials from the surface of the brain. Nat Neurosci. https://doi.org/10.1038/nn.3905

16. Escabi MA, Read HL, Viventi J, et al (2014) A high-density, high-channel count, multiplexed ECoG array for auditory-cortex recordings. J Neurophysiol 112:1566–1583

17. Viventi J, Kim DH, Vigeland L, et al (2011) Flexible, foldable, actively multiplexed, high-density electrode array for mapping brain activity in vivo. Nat Neurosci 14:1599–1605

18. Lee W, Kim D, Matsuhisa N, Nagase M, Sekino M, Malliaras GG, Yokota T, Someya T (2017) Transparent, conformable, active multielectrode array using organic electrochemical transistors. Proc Natl Acad Sci 201703886

19. Lee W, Kim D, Rivnay J, Matsuhisa N, Lonjaret T, Yokota T, Yawo H, Sekino M, Malliaras GG, Someya T (2016) Integration of Organic Electrochemical and Field-Effect Transistors for Ultraflexible, High Temporal Resolution Electrophysiology Arrays. Adv Mater 28:9722–9728

20. Hébert C, Masvidal-Codina E, Suarez-Perez A, et al (2018) Flexible Graphene Solution-Gated Field-Effect Transistors: Efficient Transducers for Micro-Electrocorticography. Adv Funct Mater 28:1–15

21. Kostarelos K, Vincent M, Hebert C, Garrido JA (2017) Graphene in the Design and Engineering of Next-Generation Neural Interfaces. Adv Mater 29:1–7

22. Masvidal-Codina E, Illa X, Dasilva M, et al (2019) High-resolution mapping of infraslow cortical brain activity enabled by graphene microtransistors. Nat Mater 18:280–288

23. Banszerus L, Schmitz M, Engels S, Dauber J, Oellers M, Haupt F, Watanabe K, Taniguchi T, Beschoten B, Stampfer C (2015) Ultrahigh-mobility graphene devices from chemical vapor deposition on reusable copper. Sci Adv 1:1–7

24. Stavrinidou E, Leleux P, Rajaona H, Khodagholy D, Rivnay J, Lindau M, Sanaur S, Malliaras GG (2013) Direct measurement of ion mobility in a conducting polymer. Adv Mater 25:4488–4493

25. Dankerl M, Hauf M V., Lippert A, et al (2010) Graphene solution-gated field-effect transistor array for sensing applications. Adv Funct Mater 20:3117–3124

26. Li X, Cai W, An J, et al (2009) Large-area synthesis of high-quality and uniform graphene films on copper foils. Science (80-) 324:1312–1314

27. Hess LH, Hauf M V., Seifert M, Speck F, Seyller T, Stutzmann M, Sharp ID, Garrido JA (2011) High-transconductance graphene solution-gated field effect transistors. Appl Phys Lett 99:2009–2012

28. Hess LH, Jansen M, Maybeck V, Hauf M V., Seifert M, Stutzmann M, Sharp ID, Offenhäusser A, Garrido JA (2011) Graphene transistor arrays for recording action potentials from electrogenic cells. Adv Mater 23:5045–5049

11

29.   Buzsáki G, Anastassiou CA, Koch C (2012) The
        origin of extracellular fields and currents-EEG,
        ECoG, LFP and spikes. Nat Rev Neurosci
        13:407–420

30.   Pesaran B, Vinck M, Einevoll GT, Sirota A, Fries
        P, Siegel M, Truccolo W, Schroeder CE,
        Srinivasan R (2018) Investigating large-scale
        brain dynamics using field potential recordings:
        Analysis and interpretation. Nat Neurosci
        21:903–919

31.   Sirota A, Buzsáki G (2005) Interaction between
        neocortical and hippocampal networks via slow
        oscillations. Thalamus Relat Syst 3:245–259

32.   Katzner S, Nauhaus I, Benucci A, Bonin V,
        Ringach DL, Carandini M (2009) Local Origin of
        Field Potentials in Visual Cortex. Neuron 61:35–
        41

33.   Michalareas G, Vezoli J, van Pelt S, Schoffelen
        JM, Kennedy H, Fries P (2016) Alpha-Beta and
        Gamma Rhythms Subserve Feedback and
        Feedforward Influences among Human Visual
        Cortical Areas. Neuron 89:384–397

34.   Cozzolino O, Marchese M, Trovato F, Pracucci E,
        Ratto GM, Buzzi MG, Sicca F, Santorelli FM
        (2018) Understanding spreading depression
        from headache to sudden unexpected death.
        Front Neurol 9:1–13

Appendix B

Complementary publications

B.1 Switchless multiplexing of graphene active sensor arrays for brain mapping

This article reports on the use of frequency-domain multiplexing (FDM) to address and readout a 4x8 μ-ECoG-array of gSGFETs. As FDM utilizes high-frequent sinusoidal carrier waves to bias the transistor, the fidelity of the resulting recordings in such AC-operation are compared to the ones obtained in static DC-mode. Moreover the scalability of FDM towards large sensor-arrays is evaluated, with a limited accessible frequency-band and amplifier range as well as increasing intersite crosstalk being the principal restrictions. Here, phase optimization and quadrature mode operation are presented as potential solutions for large arrays. Finally, acute in-vivo recordings in rodents are presented, accurately mapping a range of electrophysiological signals from infraslow oscillations (cortical spreading depression) to local-field-potentials (spontaneous and visually evoked activity).

Switchless Multiplexing of Graphene Active Sensor Arrays for Brain Mapping

Ramon Garcia-Cortadella,[∇] Nathan Schäfer,[∇] Jose Cisneros-Fernandez, Lucia Ré, Xavi Illa, Gerrit Schwesig, Ana Moya, Sara Santiago, Gonzalo Guirado, Rosa Villa, Anton Sirota, Francesc Serra-Graells, Jose A. Garrido,* and Anton Guimerà-Brunet*

ACCESS | Metrics & More | Article Recommendations | Supporting Information

ABSTRACT: Sensor arrays used to detect electrophysiological signals from the brain are paramount in neuroscience. However, the number of sensors that can be interfaced with macroscopic data acquisition systems currently limits their bandwidth. This bottleneck originates in the fact that, typically, sensors are addressed individually, requiring a connection for each of them. Herein, we present the concept of frequency-division multiplexing (FDM) of neural signals by graphene sensors. We demonstrate the high performance of graphene transistors as mixers to perform amplitude modulation (AM) of neural signals *in situ*, which is used to transmit multiple signals through a shared metal line. This technology eliminates the need for switches, remarkably simplifying the technical complexity of state-of-the-art multiplexed neural probes. Besides, the scalability of FDM graphene neural probes has been thoroughly evaluated and their sensitivity demonstrated *in vivo*. Using this technology, we envision a new generation of high-count conformal neural probes for high bandwidth brain machine interfaces.

KEYWORDS: Multiplexing, graphene, active sensors, bioelectronics, neural sensing
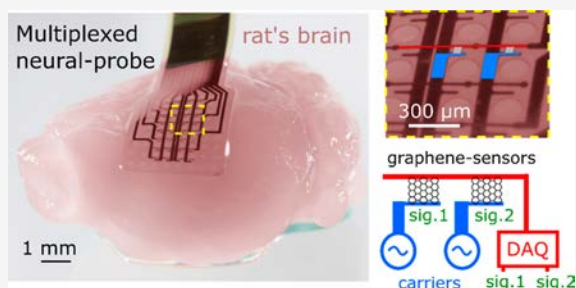
Over the last decades, progress in neurotechnology has enabled a deeper understanding of brain functions such as motor control[1,2] or speech processing and synthesis.[3,4] In turn, these insights have prompted the realization of technological breakthroughs in the field of brain-computer interfaces (BCIs) such as partial restoration of movement[5] or decoding of speech from neural activity.[6] Cortical functions involved in such tasks often emerge from the integration of information in distinct brain regions, yet local activity from small groups of neurons carries essential information for neural coding.[7] Therefore, combining the coverage of large brain areas with high sensor density (i.e., high sensor count) is paramount for both neuroscientific and biomedical applications.[8−10] In this sense, one of the main limitations in current neurotechnologies originates in the need of individually connecting each sensing element to a signal amplifier. This constrain implies having as many conductive lines as sensors in the neural probes, which imposes a trade-off between sensor density and coverage area. One way to overcome this constrain is to perform multiplexing among sensors which allows the transmission of multiple signals over a shared wire.

State-of-the-art sensing technologies for neuroscientific research are mostly based on micro electrode arrays, which can be embedded either in a narrow shank for intracortical mapping[11−14] or in a planar configuration.[8,15−18] Intracortical

electrode arrays can be fabricated on rigid substrates,[19] therefore enabling the incorporation of integrated-circuits (ICs) on the probes[12] to amplify and multiplex the measured signals. However, planar arrays on rigid substrate are not conformal with the surface of the brain and are therefore limited to *in vitro* studies.[16−18] Alternatively, flexible electrocorticography (ECoG) arrays are conformal, enabling the detection of local field potentials[20] (LFP) from the surface of the brain.[8,15] ECoGs represent an interesting technology for biomedical applications, since they could be applied to extract a similar information than that obtained with intracortical probes[21,22] but with the additional advantage of lower invasiveness. Nevertheless, the flexible substrate strongly limits the use of nanofabrication methodologies and available materials to fabricate integrated circuits on the neural probe, thus restricting the implementation of *in situ* signal amplification for time-division multiplexing (TDM) of neural
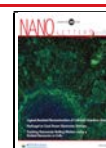
Figure 1. Frequency-domain multiplexing of g-SGFET arrays (a) Equivalent circuit of the g-SGFET together with an illustration of the device. (b) Schematic of the neural probe layout. On the left, the whole probe is displayed. A zoom-in of the probe tip is shown on the top-right image. The orange/yellow colors represent the first/second metal layers, separated by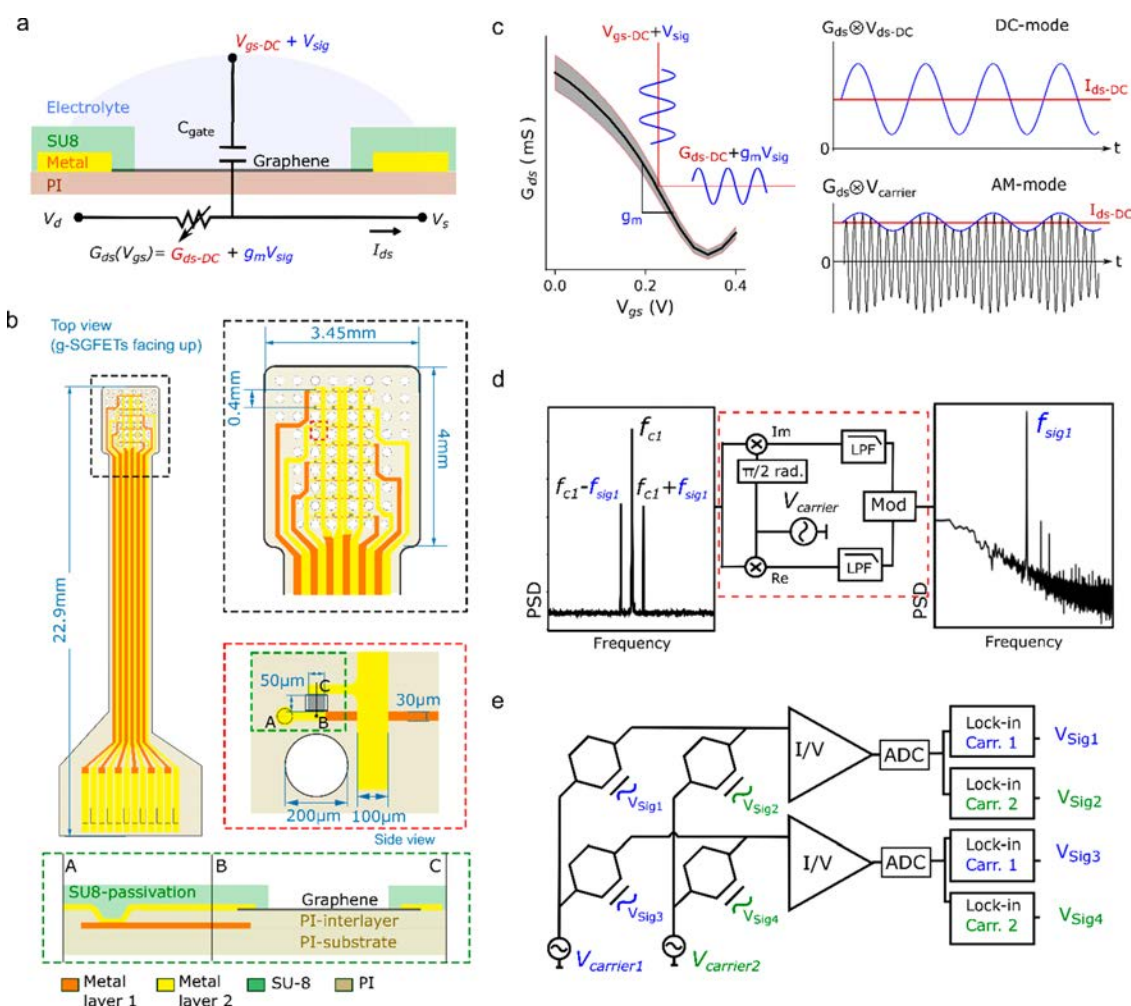 a 2 μm thick polyimide layer. A zoom-in of a single pixel is shown within the red dashed-line square. The bottom schematic depicts a side view of the g-SGFET, showing the connection between the first and second metal layer through a VIA hole in the PI. (c) Typical $G_{ds}-V_{gs}$ curve of g-SGFETs. The filled area represents the standard deviation ($n = 8$). The definition of normalized transconductance (g_m) as the slope of the $G_{ds}-V_{gs}$ curve is indicated in the graph. The g-SGFETs acts as a multiplier of the drain-to-source voltage and the signal at the gate. The resulting I_{ds} in the DC and AM modes is illustrated. (d) The signal folded by the carrier is shown in the frequency domain (left). Demodulation scheme (middle): the multiplication of the modulated signal by an oscillator at the carrier frequency of interest and the $\pi/2$ radians phase-shifted oscillator allows the recovery of the module of the signal in the baseband (right). (e) Basic schematic of the addressable g-SGFET array, which allows modulating the signals at the gate of different g-SGFETs with different carrier frequencies. The mixed signals, containing multiple carrier frequencies, are demodulated after current-to-voltage conversion and digitization.

signals.[23] Flexible materials have been proposed to perform switching among active sensors in an addressable array configuration, including organic semiconductors[24] or ultrathin silicon layers.[25] However, organic semiconductors present an insufficient mobility for high-speed operation, which is critical to achieve high sampling speed for a large number of sensors, and the high complexity of ultrathin silicon technology on flexible substrates limits its widespread application.

Herein, we present a novel approach that uses frequency-division multiplexing (FDM) of graphene solution-gated field-effect-transistors (g-SGFETs) in order to eliminate the need for on-site switches and to reduce the fabrication complexity of high-count neural probes. In this approach, neural signals detected by different graphene active sensors on the array are amplitude modulated (AM) by different carrier signals, allowing the transmission of multiple signals through a shared communication channel. We present the fabrication of g-SGFET arrays on an addressable column/row matrix configuration to demonstrate their high performance for FDM operation *in vivo*, sensing wide-band neural activity from the surface of the rat brain. Besides, we carefully assess the scalability of this technique, demonstrating the operation of g-SGFETs for a wide range of carrier frequencies, the low impact of crosstalk, and the requirements for an application specific integrated circuit (ASIC) to operate large-scale flexible arrays. The simplification of the technological complexity,
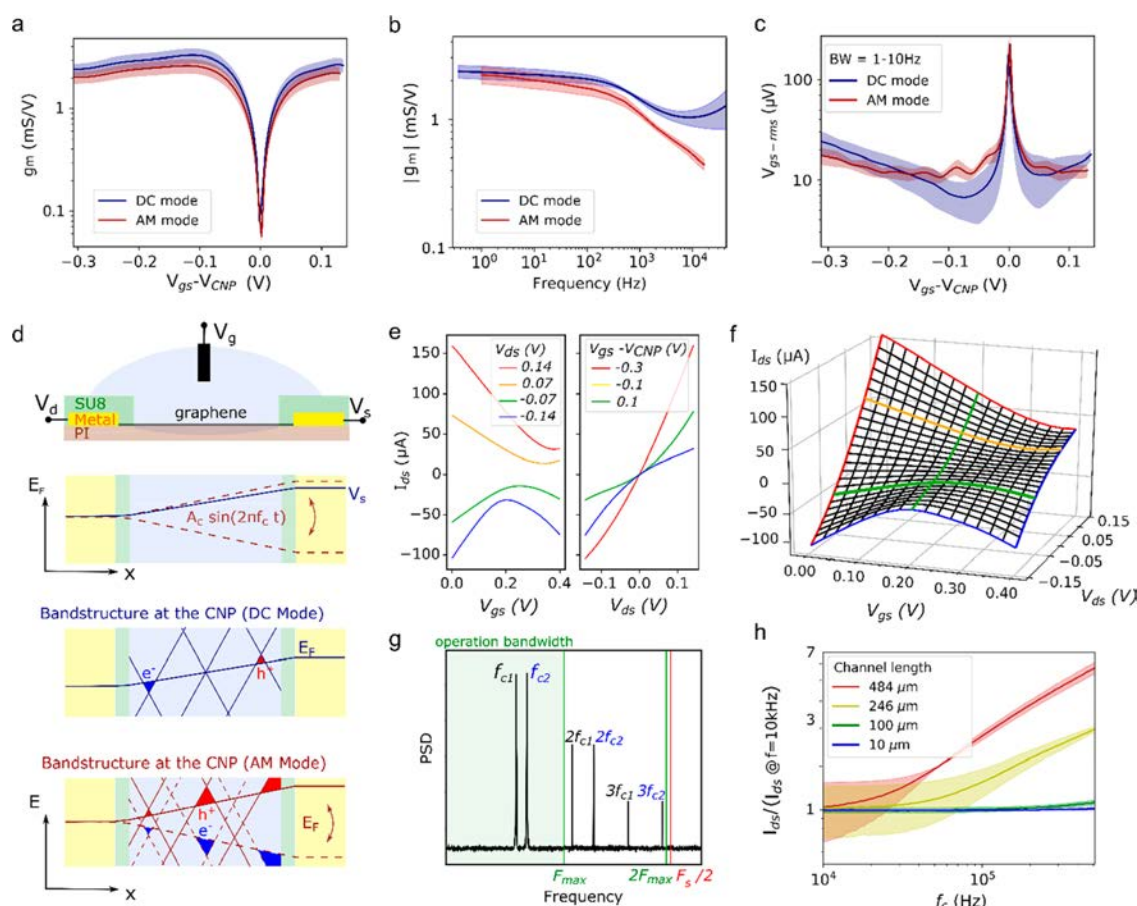
Figure 2. *In vitro* evaluation of g-SGFET performance in the AM mode. (a) g_m–V_{gs} relationship in the AM and DC modes, measured in a 3×3 g-SGFET array. (b) The magnitude of g_m over frequency of the signal applied at the gate is shown for the two modes. The response was measured in a 2×2 g-SGFET array. (c) V_{gs-rms} for an integration bandwidth of 1–10 Hz measured in the AM and DC modes; measurements performed with a 3×3 g-SGFET array. (d) Schematic representation of a g-SGFET and the Fermi energy in the graphene for the DC and AM mode (top). The band structure at the charge neutrality point (CNP) is shown along the graphene channel for the DC (middle) and AM (bottom) modes. (e) Dependence of I_{ds} on V_{gs} and V_{ds}, revealing the shift in the CNP, as well as the nonlinearities in the I_{ds}–V_{ds} produced by the effective gating. (f) Three-dimensional representation of the I_{ds} dependence on V_{gs} and V_{ds}. The relation between shifts of I_{ds}–V_{gs} along the V_{gs} axis and nonlinearities introduced in the I_{ds}–V_{ds} curves can be observed. (g) Two carrier signals and their second and third order harmonics are represented in the frequency domain. The frequency which defines the bandwidth of operation (F_{max}) and the position of the Nyquist frequency ($F_s/2$) with respect to F_{max} are indicated by the vertical lines. (h) The I_{ds} normalized by its value at 10 kHz is shown for different channel lengths. The filled area represents the standard deviation ($n = 3$).

achieved by the elimination of switches and the use of graphene electronics, opens the door to the implementation of high-count flexible neural probes as a readily available technology for neuroscientific studies as well as clinical applications.

FREQUENCY-DIVISION MULTIPLEXING OF G-SGFET ARRAYS

g-SGFETs have been proposed as signal transducers in the field of biosensing and bioelectronics,[15,26−28] presenting unique properties for the detection of full-band neural signals from infraslow to high-frequency components with a high spatial resolution.[29] Besides, as active sensors g-SGFETs provide an intrinsic preamplification of the signal and can be arranged in a column/row addressable matrix due to their two terminal (i.e., drain and source) configuration (see Figure 1a,b). These properties, combined with their remarkable

frequency response,[30] make g-SGFETs an ideal technology for the implementation of frequency-division sensor arrays.

In g-SGFETs, the graphene channel is placed in contact with an electrolyte gate, that is, the brain tissue in the case of neural sensing applications. Electrical potential fluctuations in the environment influence the conductivity of the transistor channel through the gate capacitance. The constant of proportionality between drain-source conductance (G_{ds}) and the electrical potential at the interface (V_{gs}) is referred to as the transconductance[31] (g_m). g-SGFETs can be modeled by the equivalent circuit shown in Figure 1a. Its stationary response to a constant bias (V_{gs-DC}) is described by the voltage dependent term G_{gs-DC}, while its dynamic response to a small-amplitude, time-dependent signal (V_{sig}) is characterized by the term $V_{sig}g_m$. In the typical operation mode (DC mode), the drain-source bias V_{ds} is constant; thus, the only time variations in the drain-source current (I_{ds}) are caused by variations in G_{ds}
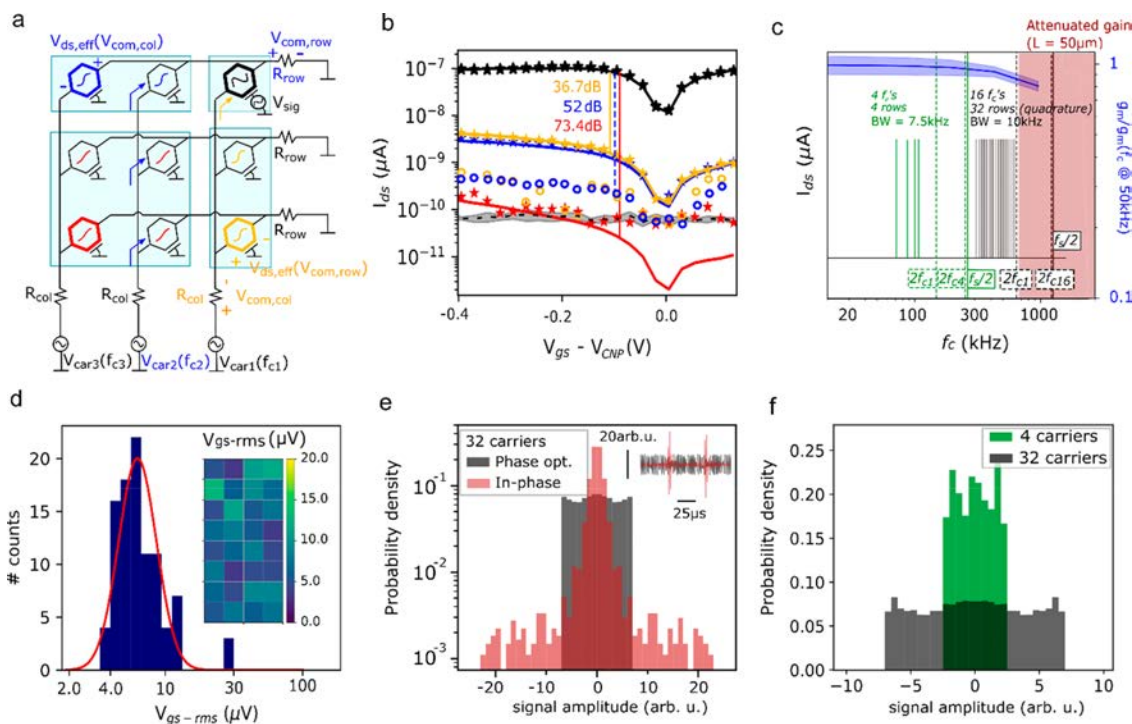
Figure 3. Scalability of g-SGFET arrays multiplexed in the frequency-domain: (a) Equivalent circuit of a 3 × 3 g-SGFET array. The metal track resistance of the columns and rows is modeled by R_{col} and R_{row} respectively. Each column is biased with a different carrier (V_{car1}, V_{car2}, and V_{car3}). Common voltage oscillations ($V_{com,coll}$ and $V_{com,row}$) produce changes in $V_{ds,eff}$. The light blue area indicates the position of four polyelectrolyte gates printed on a 3 × 3 array. (b) Response to a 5 Hz signal measured in different g-SGFETs on a 3 × 3 array for different V_{gs} values. The color of the symbols and lines indicate the position of the corresponding g-SGFET in the 3 × 3 array shown in panel a. The solid lines indicate the fitting by the analytical model. The noise (dashed black line) was measured at 7 Hz. The empty blue and orange circles indicate the crosstalk level after correction. The signal-to-crosstalk values (in dB) corresponding to uncorrected, corrected, and second order crosstalk are marked by the vertical lines. (c) The right axis indicates the normalized transconductance for g-SGFETs of (50 μm x 50 μm, n = 4). The carrier frequencies selected for the *in vivo* proof of concept (4 × 8 array) are shown in green and those proposed for a 32 × 32 sensor array are indicated in black. High order harmonics are indicated together with the required sampling frequency. (d) Histograms of V_{gs-rms} from htree neural probes of 32 g-SGFETs integrated in the 1−10 Hz frequency. The log-normal distribution indicates the mean and standard deviation of V_{gs-rms}. The values from the specific neural probe which was implanted is shown in the inset. (e) Histogram of 32 superposed carriers with phase optimization to minimize the peak-to-peak amplitude (black) and with all carriers in phase (red). The inset shows a fragment of the resulting signals. (f) Histogram of the 4 superposed carriers used for the *in vivo* proof of concept compared to the amplitude of a 32-carrier signal with phase optimization.

(Figure 1c). On the other hand, in FDM (or amplitude modulation- AM mode), the drain-source bias is typically a pure tone signal ($V_{carrier}(t)$). Therefore, I_{ds} results from the product of $V_{carrier}(t)(g_m V_{sig}(t) + G_{ds-DC})$ (see Figure 1c).

The multiplication of $V_{carrier}$ and V_{sig} produces the folding of their frequencies. In the frequency-domain representation of $V_{carrier}(t) * V_{sig}(t)$ (Figure 1d, left), a peak at the carrier frequency (f_c) can be observed, which is proportional to G_{ds-DC}. In addition, two side bands (at $f_c - f_{sig}$ and $f_c + f_{sig}$) appear, the amplitude of which is proportional to $g_m V_{sig}$. This mixed signal can then be demodulated by a lock-in amplifier (see Figure 1d, middle) producing the folding of the side bands back to the baseband frequency (see Figure 1d, right) with the DC-offset corresponding to the stationary component of I_{ds}. This demodulation can be repeated for different carrier frequencies to recover the neural signals detected in each of the graphene sensors. The schematic in Figure 1e represents the FDM of a 2 × 2 sensor array. Carrier signals with different frequencies (f_c) are applied at each column of the array and independent data-acquisition channels are connected to each of the drains to reliably recover the information from the

multiplexed sensors. Here, we present frequency-division multiplexed arrays of up to 4 × 8 graphene sensors fabricated on a flexible polyimide (PI) substrate (see Figure 1b and Supporting Information for more details of the fabrication method). For the characterization of the FDM sensor arrays and their operation *in vivo*, we have developed a recording system based on a PXIe for high sampling speed and a custom built front-end amplifier for current−voltage conversion (see Supporting Information).

■ *IN VITRO* CHARACTERIZATION OF FDM GRAPHENE NEURAL PROBES

In order to validate the suitability of g-SGFETs for frequency-division multiplexing, their sensitivity in the AM mode must be characterized and compared with the sensitivity in the DC mode. The characterization of g_m can be performed of the following two approaches: from the derivative of the stationary $G_{ds}-V_{gs}$ curve or from the dynamic response of g-SGFETs to signals with various frequency components applied at the gate (see Figure 1c). Figure 2a shows the g_m-V_{gs} curves extracted following the first approach for a 3 × 3 g-SGFET array,

demonstrating the equivalence of the stationary response in the DC and AM operation modes. Figure 2b presents the frequency dependence of g_m measured following the second approach. The magnitude of g_m presents similar values in both modes for frequencies <1 kHz, above which the effect of capacitive currents contributes significantly in the DC mode (see Supporting Information). In addition to the transconductance, the intrinsic electrical noise of the graphene transistors shall be considered in order to fully characterize the sensitivity of the graphene sensors. In Figure 2c, the equivalent noise at the gate (V_{gs-rms}), defined as the RMS current noise (I_{ds-rms}) normalized by the transconductance, is represented under different V_{gs} bias conditions for a transistor area of 50 μm × 50 μm. Figure 2c demonstrates that the sensitivity of g-SGFETs, defined by their noise performance, does not differ dramatically in both modes, showing only slight changes in its V_{gs} dependence.

These slight discrepancies presumably arise from the differences in the drain-source bias in both modes. The gradient in the work function of graphene along the channel induced by this bias causes a nonhomogeneous effective gating of the transistor (see Figure 2d and Supporting Information). In the DC mode, this gradient is constant over time, producing a constant offset in the channel doping for a certain V_{ds} bias. Changing V_{ds} produces a shift of the transfer curves of the g-SGFETs along the V_{gs} axis (see Figure 2e). This effective gating is also responsible for the dependence of G_{ds} on V_{ds}, which introduces nonlinearities in the output characteristics shown in Figure 2e. Figure 2f shows a three-dimensional representation of the $I_{ds}-V_{gs}$ and $I_{ds}-V_{ds}$ characteristic curves of the g-SGFETs. In the DC mode, the g-SGFETs are operated at a stationary point in the $V_{gs}-V_{ds}$ plane but in the AM mode the drain-source bias oscillates along the V_{ds} axis. In this way, nonlinearities in the $I_{ds}-V_{ds}$ curves will lead to distortion of the carrier signal, introducing harmonics at frequencies multiple of f_c (see Figure 2g and Supporting Information). Harmonic distortion constrains the selection of carrier frequencies that can be used for AM: high order harmonics must not lie within the frequency band of operation dedicated to the carrier signals. Thereby, the frequency of all carriers must be below the second order harmonic of the carrier of lowest frequency (see Figure 2g). In addition, the Nyquist frequency ($f_s/2$) must be above the second order harmonic of the highest carrier frequency in order to prevent folding of third order harmonics into the band of operation by aliasing.

Another important aspect affecting the selection of carrier frequencies is the frequency response of g-SGFETs. The graphene−electrolyte interface exhibits a capacitive response, which at high frequencies allows a displacement current to flow from drain to source through the electrolyte,[30] degrading the device performance. The characteristic cutoff frequency of this phenomenon appears at relatively high frequencies due to the high ratio between mobility and interface capacitance in graphene. Other active sensors, such as organic electrochemical transistors, which present a lower mobility and a larger interface capacitance,[32] are expected to present a worse frequency response.[30] Figure 4e shows the frequency response of g-SGFETs for multiple channel lengths, demonstrating an approximately constant response for channels shorter than 100 μm and frequencies below 500 kHz at least.

SCALABILITY OF FDM GRAPHENE NEURAL PROBES

Considering the ultimate goal of enabling high-density, large-area sensor arrays, the scalability of the FDM graphene neural probes has to be thoroughly explored. Important aspects limiting the scalability of FDM are the crosstalk in the g-SGFET array, the constrains in the selection of carrier frequencies, and the requirements for the electronics used to operate the arrays.

In FDM, no switching among sensing sites is required. Although this feature bears a clear advantage for ease of fabrication of the neural probes, it prevents from doing on-site switching of the sensors and can therefore lead to an increased susceptibility to crosstalk. Crosstalk can appear between g-SGFETs in the same row (i.e., sharing a readout channel) as well as in the same column (i.e., biased by the same carrier) due to common-mode voltage (V_{com}) oscillations in the resistance of metal tracks in series with the drain (R_{row}) and source (R_{col}). By analyzing the equivalent circuit in Figure 3a, an analytical expression can be derived, which indicates that crosstalk among rows and among columns is proportional to R_{row} and R_{col}, respectively (see Figure 3a and Supporting Information). Additionally, crosstalk signals couple with g-SGFETs that are out of the same column and row, causing a second order crosstalk (see Supporting Information S4). In order to experimentally determine the crosstalk level, we have patterned multiple polyelectrolyte gates on the graphene sensor arrays by inkjet printing (see Figure 3a and Supporting Information S5). Figure 3b shows the signal measured by an individually gated g-SGFET (black) and the crosstalk it induced on sensors in the same column (orange), the same row (blue), and on the rest of g-SGFETs (red), together with the fitting of the experimental data using the analytical expression presented in the Supporting Information. A crosstalk of ∼36 dB/∼73 dB is observed for g-SGFETs within/outside the same column or row, which corresponds to a $R_{row} \approx R_{col} = 50\ \Omega$. In order to reduce the crosstalk to the level achieved using on-site switches (∼65 dB),[33] the resistance of the tracks should be reduced to the range of few ohms. This target could be met by increasing the width of the metal lines, which can be implemented easily when translating this technology from rodents research into human clinical applications (see Supporting Information S8). Moreover, knowing the mechanism of crosstalk generation and the coupling parameters among all sensors, it is possible to define a mathematical method for crosstalk cancelation (see Supporting Information S8). Using such calibration, a mitigation of crosstalk by an additional ∼15 dB was achieved (see Figure 3b).

Another important aspect related to the scalability of FDM graphene neural probes is the selection of the carrier frequencies, which are constrained by the frequency response of g-SGFETs and the harmonic distortion of the carrier signals. The $g_m(f_c)$ was characterized by sweeping f_c and measuring the dynamic response of the graphene sensors to pure tone signals applied at the gate. Figure 3c shows that g_m remains approximately constant for carrier frequencies up to at least $F_{max} = 600$ kHz and a channel length of 50 μm, while the current noise remains approximately constant (see Supporting Information S10). This bandwidth limitation is presumably caused by the capacitive leakage through the electrolyte characterized in Figure 2h and could therefore be expanded by
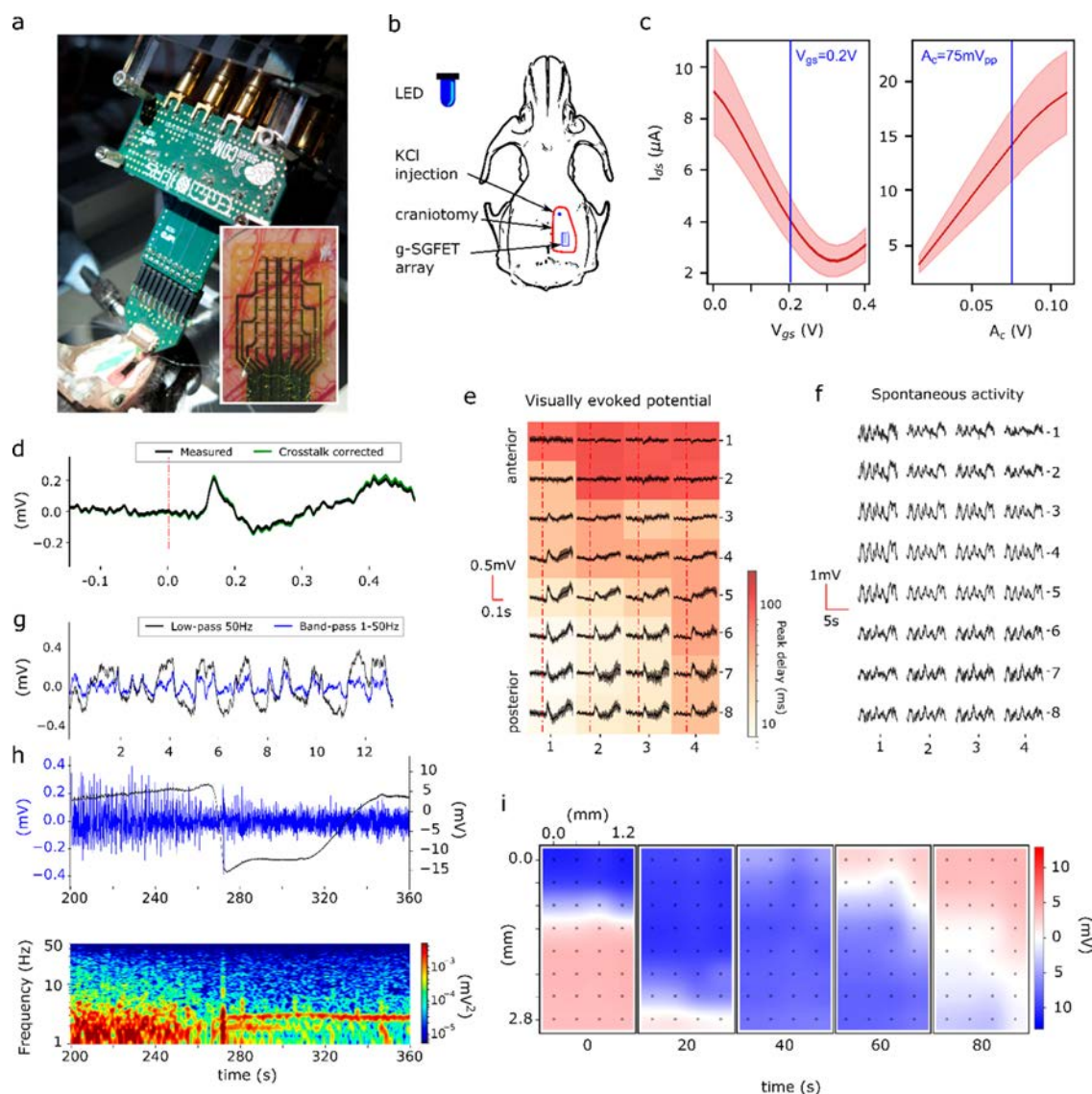
Figure 4. *In vivo* validation of FDM graphene neural probes for brain recordings. (a) Acute experiment setting. The g-SGFET array interfaces the brain with the custom-built front-end amplifier. (b) Illustration of a rat skull indicates the position of the craniotomy, the g-SGFET array, the LED, and the place of KCl injection. (c) Average and standard deviation of the $I_{ds}-V_{gs}$ and $I_{ds}-A_c$ curves obtained *in vivo* for the 32 channels. (d) The visually evoked potential averaged over 10 consecutive events is shown for the g-SGFET placed on the lower-left corner of the array before (black) and after (green) crosstalk correction. (e) Visually evoked potential averaged over 10 consecutive events for all g-SGFETs on the 4 × 8 array. The color map represents the delay between stimulus and the peak of the response. (f) Map of spontaneous activity under anesthesia. (g) Spontaneous activity filtered in two different bands indicates the presence of low-frequency components (<1 Hz) for channel in position (4,5). (h) CSD event recorded in a single g-SGFET. The top graph shows the activity in the 1−50 Hz band (blue, left axis) and the wide-band activity (0.001−50 Hz) (black, right axis). The corresponding spectrogram in the 1−50 Hz band is shown below. (i) The color maps indicate the signal amplitude in each of the g-SGFETs on the array at different times during the CSD propagation.

shortening the channel length of g-SGFET. Sampling at four times this F_{max} (i.e., $F_s \geq 4F_{max} = 2.4$ MHz) allows the use of carriers of up to ~600 kHz. Figure 3c shows a combination of carrier frequencies which meets all the requirements to allow the operation of 32 × 32 graphene sensor arrays. In this configuration, operation in quadrature AM[34] can be used to maximize the frequency bandwidth of each sensor to 10 kHz (see Figure 3c). The demodulated signals can then be high-pass filtered in the digital domain above ~5 kHz, given that

neural activity does not present significant power above such frequency. Importantly, the demodulated signals are still sampled in the megahertz range, allowing for an arbitrarily high oversampling. In this way, a 10 kHz guard-band between carriers can be kept to ensure a correct channel discrimination.

The discrete electronics system designed for the validation of the technology *in vivo* is limited to operate arrays of up to 4 × 8 g-SGFETs. This limitation comes from the constrained scalability of discrete electronics in opposition to ASICs.

Figure 3c shows the combination of carrier frequencies used for the in vivo proof of concept. The V_{gs-rms} from three probes of 4×8 g-SGFET arrays operated with this carrier's configuration is shown in Figure 3d, demonstrating a mean sensitivity of 6.29 μV with a standard deviation of 1.37 μV and a yield of 100%. This high sensitivity can eventually degrade due to the superposition of a large number of carrier signals, the large amplitude of which might challenge the resolution of the data acquisition (DAQ) system. The quantization error of the analog-to-digital converter (ADC), given by its less-significant bit (LSB), must be low enough to ensure signal integrity. When increasing the number of carriers, their amplitude (A_c) must be reduced in order to prevent saturation of the ADC (see Supporting Information S11). This decrease in A_c implies an attenuation of the transconductance (i.e., $A_c g_m$) of the g-SGFETs, while the LSB of the ADC remains unchanged. To minimize the amplitude of the carriers superposition for a certain A_c, the phase of the carriers can be adjusted. Figure 3e shows the improvement obtained by phase optimization for the combination of 32 carrier signals defined in Figure 3c, revealing a three-fold attenuation in the amplitude of the carrier superposition. The comparison with the superposition of the 4 carriers used for this proof of concept shows that upscaling to 32 carriers causes an increase in the amplitude by a factor of 2.8, which could be compensated by increasing the resolution of the ADC by 1−2 bits.[35] These results, together with the evaluation of crosstalk and the high frequency response of g-SGFETs, demonstrate the potential of this technology for high-count flexible neural probes.

■ IN VIVO EVALUATION OF FDM GRAPHENE NEURAL PROBES

Previous works have shown that g-SGFETs operated in the DC mode present a high sensitivity for the recording of neural activity.[15,26] Moreover, g-SGFETs have demonstrated a unique capability for the recording of infraslow neural activity with a high spatial resolution.[29] The FDM operation of g-SGFETs is not only expected to preserve their sensitivity for infraslow signals but to enhance their performance by eliminating flicker noise from the amplifiers due to the lock-in amplification in the AM mode. In addition, due to the low power consumption of g-SGFETs, heating of the tissue is not expected to be significant even for large scale arrays (see Supporting Information S12). To validate the in vivo functionality of FDM graphene probes, we have recorded electrical activity from the cortex of a Long Evans rat in an acute setting using a 4×8 FDM graphene neural probe (see Figure 4a,b and Supporting Information). The optimum V_{gs}, which maximizes g_m, and the highest carriers amplitude (A_c), which fills the dynamic range of the amplifiers, were determined in vivo (see Figure 4c).

The sensitivity of the sensors to high-frequency LFP activity was evaluated by measuring visually evoked potentials[36] triggered by a blue LED emitting light-pulses of 100 ms every 5 s. The sensors directly placed on the primary visual cortex V1 (lower left) exhibit a sharp response with 50 ms delay and 250 μV peak amplitude lasting until 100 ms after the initial trigger (Figure 4d). Sensors placed further away from the V1 show a distance-dependent suppressed response of smaller amplitude and extended delay (Figure 4e). This result is in full agreement with previously reported values,[36] demonstrating the preserved sensitivity of g-SGFETs in this

frequency band in the FDM operation mode. Besides, the crosstalk correction method discussed above showed the low impact of crosstalk in these signals (see Figure 4d and Supporting Information).

Similarly, the distortion-free recording of infraslow activity using g-SGFET has been previously shown in the DC mode by the recording of cortical spreading depression (CSD) events.[29] CSDs are a slowly propagating wave of depolarizing neurons and astrocytes, which has been clinically related to stroke, brain injury, and migraine.[37,38] CSDs can be easily triggered by injecting KCl into the brain cortex and present a propagation speed of approximately 5 mm per minute across the cortex. Figure 4f shows the spontaneous activity under anesthesia where highly coherent transitions from up to down states can be observed. Figure 4g shows the signal from channel in position (4,5) filtered in the 1−50 Hz frequency band (blue) together with the signal filtered in the 0.001−50 Hz band. This spontaneous activity is strongly suppressed during the depolarization wave, which results in a large infraslow signal drift with a duration over 70 s. Figure 3h shows the propagating front of the CSD wave across the array, demonstrating the capabilities of FDM graphene neural probes to study topography of wide-band oscillatory dynamics in the brain.

■ DISCUSSION

In summary, we have presented the concept of frequency-division multiplexing of graphene active sensor arrays to reduce the number of wires required for high sensor-count neural probes. This novel approach presents two main advantages over time-division multiplexing resulting from its switchless operation. First, the elimination of switches implies an enormous simplification of the technological complexity, eliminating the need for high-mobility and wide band gap flexible materials, such as ultrathin SiO_2. Second, FDM operates in a continuous mode, fully circumventing the problems derived from limited switching speed and artifacts in TDM, which ultimately limit the scalability of the arrays. Moreover, the signals from all sensors are continuously sampled at high speed in the megahertz range. Although the frequency separation between carriers determines the bandwidth of the sensors, the high sampling speed allows one to acquire the neural signals with an arbitrarily high oversampling. Finally, the modulation and subsequent demodulation of the signals in the FDM mode is based on a lock-in amplification scheme, which eliminates flicker noise from the amplifiers and improves the sensitivity of the system in the infraslow frequency band.

Our results demonstrate the high performance of g-SGFETs as mixers to perform on-site amplitude modulation of neural signals. We have shown their high sensitivity for wide-band neural signals both in the beaker as well as in vivo. Besides, we have also demonstrated the outstanding drain-source frequency response of solution-gated graphene sensors, validating their performance for high carrier frequencies, required for the operation of large-scale arrays. In addition, we have evaluated the crosstalk among sensing sites, which could reach the same level as for TDM with on-site switches when translating this technology to human scale neural probes. In order to maintain the sensitivity of the system for large arrays with up to 32 superposed carriers, we have described the use of carrier phase optimization as well as the requirements for the DAQ system, which could be met by an ASIC.[35]

The viability of large arrays controlled by an ASIC allows one to envision the realization of a new generation of high-density and large-area sensor arrays. The simplicity and robustness of the switchless, FDM methodology compared to state-of-the-art alternatives,[33,39] together with the high sensitivity, flexibility and biocompatibility of graphene active sensors make the implementation of these technologies very promising for both neuroscientific research as well as clinical applications.

■ ASSOCIATED CONTENT

Ⓢ Supporting Information

The Supporting Information is available free of charge at https://pubs.acs.org/doi/10.1021/acs.nanolett.0c00467.

> Fabrication process of the graphene sensor arrays; electrical setup hardware and software for device characterization and *in vivo* proof of concept; animal handling and device implantation; high-frequency response in DC-mode; nonhomogeneous doping of graphene transistors; carriers and baseband harmonic distortion; crosstalk modeling; crosstalk cancelation and scalability; validation of polyelectrolyte gating and frequency response in the DC-mode; dynamic range; frequency response of electrical noise and crosstalk; Power consumption and tissue heating; comparison of FDM graphene neural probes with state of the art technologies (PDF)

■ AUTHOR INFORMATION

Corresponding Authors

Jose A. Garrido − *Catalan Institute of Nanoscience and Nanotechnology (ICN2), CSIC and BIST, 08193 Bellatera, Barcelona, Spain; ICREA, 08010 Barcelona, Spain;* ⓞ orcid.org/0000-0001-5621-1067; Email: joseantonio.garrido@icn2.cat

Anton Guimerà-Brunet − *Instituto de Microelectrónica de Barcelona, IMB-CNM (CSIC), 08193 Bellatera, Spain; Biomateriales y Nanomedicina (CIBER-BBN), Centro de Investigación Biomédica en Red en Bioingenieria, 08193 Madrid, Spain;* Email: anton.guimera@imb-cnm.csic.es

Authors

Ramon Garcia-Cortadella − *Catalan Institute of Nanoscience and Nanotechnology (ICN2), CSIC and BIST, 08193 Bellatera, Barcelona, Spain;* ⓞ orcid.org/0000-0002-1506-6534

Nathan Schäfer − *Catalan Institute of Nanoscience and Nanotechnology (ICN2), CSIC and BIST, 08193 Bellatera, Barcelona, Spain*

Jose Cisneros-Fernandez − *Instituto de Microelectrónica de Barcelona, IMB-CNM (CSIC), 08193 Bellatera, Spain*

Lucia Ré − *Instituto de Microelectrónica de Barcelona, IMB-CNM (CSIC), 08193 Bellatera, Spain; Biomateriales y Nanomedicina (CIBER-BBN), Centro de Investigación Biomédica en Red en Bioingenieria, 08193 Madrid, Spain*

Xavi Illa − *Instituto de Microelectrónica de Barcelona, IMB-CNM (CSIC), 08193 Bellatera, Spain; Biomateriales y Nanomedicina (CIBER-BBN), Centro de Investigación Biomédica en Red en Bioingenieria, 08193 Madrid, Spain*

Gerrit Schwesig − *Bernstein Center for Computational Neuroscience Munich, Munich Cluster of Systems Neurology (SyNergy), Faculty of Medicine, Ludwig-Maximilians Universität München, Planegg-Martinsried, Germany 80539*

Ana Moya − *Instituto de Microelectrónica de Barcelona, IMB-CNM (CSIC), 08193 Bellatera, Spain;* ⓞ orcid.org/0000-0001-6793-9133

Sara Santiago − *Departament de Química, Universitat Autònoma de Barcelona, 08193 Bellatera, Barcelona, Spain*

Gonzalo Guirado − *Departament de Química, Universitat Autònoma de Barcelona, 08193 Bellatera, Barcelona, Spain*

Rosa Villa − *Instituto de Microelectrónica de Barcelona, IMB-CNM (CSIC), 08193 Bellatera, Spain; Biomateriales y Nanomedicina (CIBER-BBN), Centro de Investigación Biomédica en Red en Bioingenieria, 08193 Madrid, Spain*

Anton Sirota − *Bernstein Center for Computational Neuroscience Munich, Munich Cluster of Systems Neurology (SyNergy), Faculty of Medicine, Ludwig-Maximilians Universität München, Planegg-Martinsried, Germany 80539*

Francesc Serra-Graells − *Instituto de Microelectrónica de Barcelona, IMB-CNM (CSIC), 08193 Bellatera, Spain*

Complete contact information is available at:
https://pubs.acs.org/10.1021/acs.nanolett.0c00467

Author Contributions

R.G.C. contributed to the design and fabrication of the neural sensor arrays. He characterized the devices and contributed to the software development and *in vivo* experiments. N.S. contributed to the design of the sensor arrays, DAQ system design, and *in vivo* experiments. J.C. designed the front-end and contributed to the characterization of the DAQ system. L.R. contributed to the software development and devices characterization. X.I. contributed to the design and fabrication of the neural sensor arrays. G.S. did the surgery for the acute experiment. A.M. developed the inkjet printing procedure to evaluate the crosstalk. S.S. and G.G. developed the polyelectrolytes used for crosstalk determination. A.S. led the team for the *in vivo* proof of concept. F.S.G. contributed to the concept of frequency-division multiplexing of graphene sensor arrays and the design of the front-end. R.V. provided support for the development of the software and harware. A.G.B. contributed to the experimental design, development of the software and hardware, as well as *in vivo* proof of concept. J.A.G. led the team for development of the graphene sensor arrays and contributed to the experimental design. R.G.C., A.G.B., and J.A.G. wrote the manuscript.

Author Contributions

∇R.G.C. and N.S contributed equally to this work.

Notes

The authors declare the following competing financial interest(s): Patent application (no. EP18382593) filled by UAB, CSIC and ICN2; entitled Circuit for the multiplexing and read-out of variable-resistance sensor arrays (pending); inventors who are co-authors in the present article are A.G.B., F.S.G., and J.A.G.

■ ACKNOWLEDGMENTS

105

■ REFERENCES

(1) Jeannerod, M. *Motor Cognition: What Actions Tell the Self*; Oxford University Press, 2006.

(2) Georgopoulos, A. P.; Kettner, R. E.; Schwartz, A. B. Primate Motor Cortex and Free Arm Movements to Visual Targets in Three-Dimensional Space. II. Coding of the Direction of Movement by a Neuronal Population. *J. Neurosci.* **1988**, *8* (8), 2928−2937.

(3) Wilson, S. M.; Saygin, A. P.; Sereno, M. I.; Iacoboni, M. Listening to Speech Activates Motor Areas Involved in Speech Production. *Nat. Neurosci.* **2004**, *7* (7), 701−702.

(4) Galantucci, B.; Fowler, C. A.; Turvey, M. T. The Motor Theory of Speech Perception Reviewed. *Psychon. Bull. Rev.* **2006**, *13* (3), 361−377.

(5) Capogrosso, M.; Milekovic, T.; Borton, D.; Wagner, F.; Moraud, E. M.; Mignardot, J.-B.; Buse, N.; Gandar, J.; Barraud, Q.; Xing, D.; et al. A Brain−Spine Interface Alleviating Gait Deficits after Spinal Cord Injury in Primates. *Nature* **2016**, *539* (7628), 284−288.

(6) Anumanchipalli, G. K.; Chartier, J.; Chang, E. F. Speech Synthesis from Neural Decoding of Spoken Sentences. *Nature* **2019**, *568* (7753), 493−498.

(7) Averbeck, B. B.; Latham, P. E.; Pouget, A. Neural Correlations, Population Coding and Computation. *Nat. Rev. Neurosci.* **2006**, *7* (5), 358−366.

(8) Khodagholy, D.; Gelinas, J. N.; Thesen, T.; Doyle, W.; Devinsky, O.; Malliaras, G. G.; Buzsáki, G. NeuroGrid: Recording Action Potentials from the Surface of the Brain. *Nat. Neurosci.* **2015**, *18* (2), 310−315.

(9) Chang, E. F. Towards Large-Scale, Human-Based, Mesoscopic Neurotechnologies. *Neuron* **2015**, *86* (1), 68−78.

(10) Stringer, C.; Pachitariu, M.; Steinmetz, N.; Reddy, C. B.; Carandini, M.; Harris, K. D. Spontaneous Behaviors Drive Multi-dimensional, Brainwide Activity. *Science (Washington, DC, U. S.)* **2019**, *364* (6437), No. eaav7893.

(11) Chung, J. E.; Joo, H. R.; Fan, J. L.; Liu, D. F.; Barnett, A. H.; Chen, S.; Geaghan-Breiner, C.; Karlsson, M. P.; Karlsson, M.; Lee, K. Y.; et al. High-Density, Long-Lasting, and Multi-Region Electro-physiological Recordings Using Polymer Electrode Arrays. *Neuron* **2019**, *101* (1), 21−31.

(12) Jun, J. J.; Steinmetz, N. A.; Siegle, J. H.; Denman, D. J.; Bauza, M.; Barbarits, B.; Lee, A. K.; Anastassiou, C. A.; Andrei, A.; Aydın, Ç.; et al. Fully Integrated Silicon Probes for High-Density Recording of Neural Activity. *Nature* **2017**, *551* (7679), 232−236.

(13) Ferro, M. D.; Proctor, C. M.; Gonzalez, A.; Zhao, E.; Slezia, A.; Pas, J.; Dijk, G.; Donahue, M. J.; Williamson, A.; Malliaras, G. G. NeuroRoots, a Bio-Inspired, Seamless Brain Machine Interface Device for Long-Term Recording. *bioRxiv* **2018**, 460949.

(14) Musk, E. Neurolink. An Integrated Brain-Machine Interface Platform with Thousands of Channels. *bioRxiv* **2019**, 703801.

(15) Kostarelos, K.; Vincent, M.; Hebert, C.; Garrido, J. A. Graphene in the Design and Engineering of Next-Generation Neural Interfaces. *Adv. Mater.* **2017**, *29* (42), 1700909.

(16) Abbott, J.; Ye, T.; Qin, L.; Jorgolli, M.; Gertner, R. S.; Ham, D.; Park, H. CMOS Nanoelectrode Array for All-Electrical Intracellular Electrophysiological Imaging. *Nat. Nanotechnol.* **2017**, *12* (5), 460−466.

(17) Eversmann, B.; Jenkner, M.; Hofmann, F.; Paulus, C.; Brederlow, R.; Holzapfl, B.; Fromherz, P.; Merz, M.; Brenner, M.; Schreiter, M.; et al. A 128 × 128 CMOS Biosensor Array for Extracellular Recording of Neural Activity. *IEEE J. Solid-State Circuits* **2003**, *38*, 2306−2317.

(18) Tsai, D.; Sawyer, D.; Bradd, A.; Yuste, R.; Shepard, K. L. A Very Large-Scale Microelectrode Array for Cellular-Resolution Electro-physiology. *Nat. Commun.* **2017**, *8* (1), 1−11.

(19) Kook, G.; Lee, S. W.; Lee, H. C.; Cho, I.-J.; Lee, H. J. Neural Probes for Chronic Applications. *Micromachines* **2016**, *7* (10), 179.

(20) Andersen, R. A.; Musallam, S.; Pesaran, B. Selecting the Signals for a Brain−Machine Interface. *Curr. Opin. Neurobiol.* **2004**, *14* (6), 720−726.

(21) Chao. Long-Term Asynchronous Decoding of Arm Motion Using Electrocorticographic Signals in Monkey. *Front. Neuroeng.* **2010**. DOI: 10.3389/fneng.2010.00003.

(22) Yeager, J. D.; Phillips, D. J.; Rector, D. M.; Bahr, D. F. Characterization of Flexible ECoG Electrode Arrays for Chronic Recording in Awake Rats. *J. Neurosci. Methods* **2008**, *173* (2), 279−285.

(23) Obien, M. E. J.; Deligkaris, K.; Bullmann, T.; Bakkum, D. J.; Frey, U. Revealing Neuronal Function through Microelectrode Array Recordings. *Frontiers in Neuroscience*; Frontiers Media: S.A., 2015; p 423.

(24) Lee, W.; Kim, D.; Rivnay, J.; Matsuhisa, N.; Lonjaret, T.; Yokota, T.; Yawo, H.; Sekino, M.; Malliaras, G. G.; Someya, T. Integration of Organic Electrochemical and Field-Effect Transistors for Ultraflexible, High Temporal Resolution Electrophysiology Arrays. *Adv. Mater.* **2016**, *28* (44), 9722−9728.

(25) Viventi, J.; Kim, D.-H.; Vigeland, L.; Frechette, E. S.; Blanco, J. A.; Kim, Y.-S.; Avrin, A. E.; Tiruvadi, V. R.; Hwang, S.-W.; Vanleer, A. C.; et al. Flexible, Foldable, Actively Multiplexed, High-Density Electrode Array for Mapping Brain Activity in Vivo. *Nat. Neurosci.* **2011**, *14* (12), 1599−1605.

(26) Hébert, C.; Masvidal-Codina, E.; Suarez-Perez, A.; Calia, A. B.; Piret, G.; Garcia-Cortadella, R.; Illa, X.; Del Corro Garcia, E.; De la Cruz Sanchez, J. M.; Casals, D. V.; et al. Flexible Graphene Solution-Gated Field-Effect Transistors: Efficient Transducers for Micro-Electrocorticography. *Adv. Funct. Mater.* **2018**, *28*, 1703976.

(27) Blaschke, B. M.; Tort-Colet, N.; Guimerà-Brunet, A.; Weinert, J.; Rousseau, L.; Heimann, A.; Drieschner, S.; Kempski, O.; Villa, R.; Sanchez-Vives, M. V.; et al. Mapping Brain Activity with Flexible Graphene Micro-Transistors. *2D Mater.* **2017**, *4* (2), 025040.

(28) Hess, L. H.; Seifert, M.; Garrido, J. A. Graphene Transistors for Bioelectronics. *Proc. IEEE* **2013**, *101*, 1780.

(29) Masvidal-Codina, E.; Illa, X.; Dasilva, M.; Calia, A. B.; Dragojević, T.; Vidal-Rosas, E. E.; Prats-Alfonso, E.; Martínez-Aguilar, J.; De la Cruz, J. M.; Garcia-Cortadella, R.; et al. High-Resolution Mapping of Infraslow Cortical Brain Activity Enabled by Graphene Microtransistors. *Nat. Mater.* **2019**, *18* (3), 280−288.

(30) Drieschner, S.; Guimerà, A.; Cortadella, R. G.; Viana, D.; Makrygiannis, E.; Blaschke, B. M.; Vieten, J.; Garrido, J. A. Frequency Response of Electrolyte-Gated Graphene Electrodes and Transistors. *J. Phys. D: Appl. Phys.* **2017**, *50* (9), 095304.

(31) Mackin, C.; Hess, L. H.; Hsu, A.; Song, Y.; Kong, J.; Garrido, J. A.; Palacios, T. A Current−Voltage Model for Graphene Electrolyte-Gated Field-Effect Transistors. *IEEE Trans. Electron Devices* **2014**, *61* (12), 3971−3977.

(32) Rivnay, J.; Inal, S.; Salleo, A.; Owens, R. M.; Berggren, M.; Malliaras, G. G. Organic Electrochemical Transistors. *Nature Reviews Materials*; Nature Publishing Group, January 16, 2018. DOI: 10.1038/natrevmats.2017.86.

106

(33) Viventi, J.; Kim, D.-H.; Vigeland, L.; Frechette, E. S.; Blanco, J. A.; Kim, Y.-S.; Avrin, A. E.; Tiruvadi, V. R.; Hwang, S.-W.; Vanleer, A. C.; et al. Flexible, Foldable, Actively Multiplexed, High-Density Electrode Array for Mapping Brain Activity in Vivo. *Nat. Neurosci.* **2011**, *14* (12), 1599−1605.

(34) Chaparro, L. Fourier Analysis in Communications and Filtering. In *Signals and Systems Using MATLAB*; Elsevier, 2015; pp 449−490.

(35) Cisneros-Fernandez, J.; Dei, M.; Teres, L.; Serra-Graells, F. Switch-Less Frequency-Domain Multiplexing of GFET Sensors and Low-Power CMOS Frontend for 1024-Channel MECoG. In *2019 IEEE International Symposium on Circuits and Systems (ISCAS)*; IEEE, 2019; pp 1−5.

(36) Hébert, C.; Masvidal-Codina, E.; Suarez-Perez, A.; Calia, A. B.; Piret, G.; Garcia-Cortadella, R.; Illa, X.; Del Corro Garcia, E.; De la Cruz Sanchez, J. M.; Casals, D. V.; et al. Flexible Graphene Solution-Gated Field-Effect Transistors: Efficient Transducers for Micro-Electrocorticography. *Adv. Funct. Mater.* **2018**, *28* (12), 1703976.

(37) Dreier, J. P.; Reiffurth, C. The Stroke-Migraine Depolarization Continuum. *Neuron* **2015**, *86* (4), 902−922.

(38) Lauritzen, M.; Dreier, J. P.; Fabricius, M.; Hartings, J. A.; Graf, R.; Strong, A. J. Clinical Relevance of Cortical Spreading Depression in Neurological Disorders: Migraine, Malignant Stroke, Subarachnoid and Intracranial Hemorrhage, and Traumatic Brain Injury. *J. Cereb. Blood Flow Metab.* **2011**, *31* (1), 17−35.

(39) Fang, H.; Yu, K. J.; Gloschat, C.; Yang, Z.; Song, E.; Chiang, C.-H.; Zhao, J.; Won, S. M.; Xu, S.; Trumpis, M.; et al. Capacitively Coupled Arrays of Multiplexed Flexible Silicon Transistors for Long-Term Cardiac Electrophysiology. *Nat. Biomed. Eng.* **2017**, *1* (3), 0038.

Appendix C

Additional information

C.1 Device fabrication

gSGFET:
 The gSGFET μECoG-arrays which have been used throughout this thesis, are fabricated by standard micro-fabrication techniques using contact photolithography. In a first step, 7 μm thick biocompatible polyimide (PI-2611 HD MicroSystems) was spun on 4-inch Si/SiO$_2$ support wafers and cured under nitrogen atmosphere at 350 °C. The perpendicular metal lines of the array (columns/ rows) were patterned in two standard lift-off steps (negative photoresist AZ5214E, Clariant, Germany) with the metal deposited by e-beam evaporation (30 nm Ti/ 300 nm Au, 10 nm Ti/ 100 nm Au) and separated by a 2 μm polyimide spacer layer. Interconnecting via-holes through the spacer layer were etched by oxygen plasma using a photolithographically defined protective aluminum mask (AZ5214E, 300 nm Al), resulting in a smooth tapered profile for reliable metal-metal interconnections (figure C.1). Then, single layer graphene (grown and transferred by Graphenea) is patterned by photolithography (H6512 photoresist) and etched by oxygen-based reactive ion etching (100 W for 1 min) to form the transistor channel area. A third metal layer (20 nm Ni/ 200 nm Au) is used to contact the graphene film, either forming a sandwich contact with the bottom metal layer or a top contact for the UVO-treatment procedure, both improving the metal-graphene charge injection. In the latter case, the wafer was exposed to UV-ozone [Jelight Model 42] after developing the patterned photoresist and before depositing the metal layer. A subsequent thermal annealing step at 300 °C in ultra-high vacuum has been found to reduce surface contamination from photoresist residues and increasing the conformality of the Ni-graphene interface, thus further improving the contact resistance and device performance. To passivate the metal leads, a 2 μm thick layer of SU8 epoxy photoresist (SU-8 2005 MicroChem) was deposited, leaving open windows in the channel regions to allow a direct electrolyte graphene interface. In a final step, the polyimide was structured by deep reactive ion etching using a photoresist etching mask (AZ9260, Clariant) and the flexible probes were mechanically peeled from the support wafer.
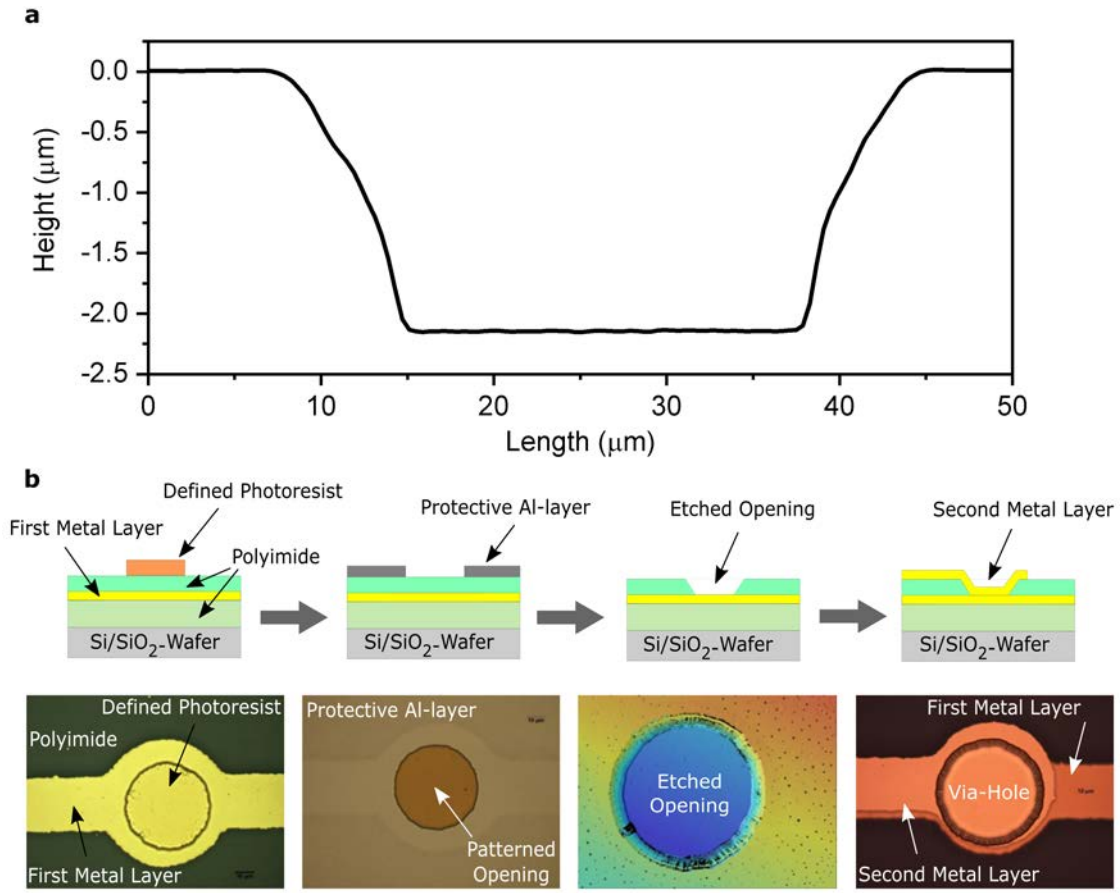
Figure C.1: Tapered via-hole technology: **a**. Profile of a polyimide via-hole from a profilometer measurement, showing a smooth slope enabling reliable metal-metal interconnections. **b.** A schematic and a microscope image is shown for each fabrication step of the interconnections, including the patterning of the photoresist to define the protective aluminium mask, the etching of the tapered profile with isotropic oxygen plasma and the deposition of top metal layer.

MoS$_2$-FET/ hybrid technology:

The MoS$_2$-FET technology presented in chapter 5 has been partially provided by the group of Prof. Dr. Thomas Müller from the Technical University of Vienna (fabrication in more detail described in [92]) and partially produced in our group. First, the bottom back-gate metal is patterned and Ti/Au is evaporated (5/25 nm). After, a back-gate oxide layer (Al$_2$O$_3$) of varying thickness between 20-40 nm is deposited by atomic layer deposition (ALD), via-holes are patterned and wet-etched by potassium hydroxide to allow interconnections between the subsequent metal layer. The MoS$_2$ film has been transferred by either dry or wet transfer. Subsequently, the rectangular channel shape is patterned and etched by Ar/SF$_6$ plasma. Next, the top metal (drain/source contact) layer is defined and deposited (Ti/Au 5/35 nm). To remove adsorbants from the surface and reduce device hysteresis, the sample is annealed in vacuum at 400 K for several hours. Finally, an encapsulation layer of either Al$_2$O$_3$ or polyimide has been deposited on top of the MoS$_2$-FETs to protect them from degradation in ambient conditions and subsequent fabrication steps. To

form the hybrid sensor technology additional via-holes were subsequently etched into this protective layer and the gSGFET technology is added on top by following the same fabrication steps as previously described.

C.2 Equation of amplitude modulation

$$I_{ds}\Big(U_{gs}(t), U_{ds}(t)\Big) \approx$$

$$\overset{(1)}{\approx} \frac{A_C sin(2\pi f_c t)}{R_{gSGFET}(U_{gs}(t))} \approx$$

$$\overset{(2)}{\approx} \left[\frac{1}{R_{gSGFET}}\bigg|_{U_{gs}^{Offset}} + \frac{\partial\Big(1/R_{gSGFET}\Big)}{\partial U_{gs}}\bigg|_{U_{gs}^{Offset}} U_{gs}(t)\right] A_C sin(2\pi f_c t) =$$

$$= \left[\frac{A_C}{R_{gSGFET}^0} + \frac{\partial\Big(1/R_{gSGFET}\Big)}{\partial U_{gs}}\bigg|_{U_{gs}^{Offset}} A_C A_S cos(2\pi f_s t + \phi)\right] sin(2\pi f_c t) =$$

$$= \left[\frac{A_C}{R_{gSGFET}^0} + g_m^{norm} A_C A_S cos(2\pi f_s t + \phi)\right] sin(2\pi f_c t) =$$

$$\overset{(3)}{=} \frac{A_C}{R_{gSGFET}^0} sin(2\pi f_c t) + \frac{g_m^{norm} A_C A_S}{2}\left[sin(2\pi(f_c + f_s)t + \phi) + sin(2\pi(f_c - f_s)t - \phi)\right]$$

(1): Approximation for the case that the channel resistance is independent of the drain bias modulation. This is not fully true since changing the drain bias has an influence on the effective gate voltage and thus also on the channel resistance.

(2): Taylor-Expansion to first order of $1/R_{gSGFET}$ in U_{gs} around U_{gs}^{Offset}. This is just true in the linear regime of the Dirac cone (constant transconductance).

(3): $sin(x) \cdot cos(y) = \frac{1}{2}\Big[sin(x + y) + sin(x - y)\Big]$
(4): g_m^{norm} is the transconductance normalized over the applied source-drain voltage

Bibliography

[1] Dimitrios G Papageorgiou, Ian A Kinloch, and Robert J Young. Progress in Materials Science Mechanical properties of graphene and graphene-based nanocomposites. *Progress in Materials Science*, 90:75–127, 2017.

[2] R. R. Nair, P. Blake, A. N. Grigorenko, K. S. Novoselov, T. J. Booth, T. Stauber, N. M R Peres, and A. K. Geim. Fine structure constant defines visual transparency of graphene. *Science*, 320(5881):1308, 2008.

[3] Jennifer Conroy, Navin K. Verma, Ronan J. Smith, Ehsan Rezvani, Georg S. Duesberg, Jonathan N. Coleman, and Yuri Volkov. Biocompatibility of Pristine Graphene Monolayers, Nanosheets and Thin Films. *arXiv*, -(1), 2014.

[4] Luca Banszerus, Michael Schmitz, Stephan Engels, Jan Dauber, Martin Oellers, Federica Haupt, Kenji Watanabe, Takashi Taniguchi, Bernd Beschoten, and Christoph Stampfer. Ultrahigh-mobility graphene devices from chemical vapor deposition on reusable copper. *Science Advances*, 1(6):1–7, 2015.

[5] Frank Schwierz. Graphene transistors. *Nature Publishing Group*, 5(May):4–5, 2010.

[6] Deji Akinwande, Cedric Huyghebaert, Ching Hua Wang, Martha I. Serna, Stijn Goossens, Lain Jong Li, H. S.Philip Wong, and Frank H.L. Koppens. Graphene and two-dimensional materials for silicon technology. *Nature*, 573(7775):507–518, 2019.

[7] F. H.L. Koppens, T. Mueller, P. Avouris, A. C. Ferrari, M. S. Vitiello, and M. Polini. Photodetectors based on graphene, other two-dimensional materials and hybrid systems. *Nature Nanotechnology*, 9(10):780–793, 2014.

[8] Ping Li, Libo Zhao, Zhuangde Jiang, Mingzhi Yu, Zhen Li, Xiangyang Zhou, and Yulong Zhao. A wearable and sensitive graphene-cotton based pressure sensor for human physiological signals monitoring. *Scientific Reports*, 9(1):1–8, 2019.

[9] Kostas Kostarelos, Melissa Vincent, Clement Hebert, and Jose A. Garrido. Graphene in the Design and Engineering of Next-Generation Neural Interfaces. *Advanced Materials*, 29(42):1–7, 2017.

[10] Dmitry Kireev and Andreas Offenhauser. Ac ce pte us cri pt us pt. *2D Materials*, 2018.

[11] Clement Hébert, Eduard Masvidal-Codina, Alejandro Suarez-Perez, Andrea Bonaccini Calia, Gaelle Piret, Ramon Garcia-Cortadella, Xavi Illa, Elena Del Corro Garcia, Jose M. De la Cruz Sanchez, Damia Viana Casals, Elisabet Prats-Alfonso, Jessica Bousquet, Philippe Godignon, Blaise Yvert, Rosa Villa, Maria V. Sanchez-Vives, Anton Guimerà-Brunet, and Jose A. Garrido. Flexible Graphene Solution-Gated Field-Effect Transistors: Efficient Transducers for Micro-Electrocorticography. *Advanced Functional Materials*, 28(12):1–15, 2018.

[12] Jonathan Viventi, Dae Hyeong Kim, Leif Vigeland, Eric S. Frechette, Justin A. Blanco, Yun Soung Kim, Andrew E. Avrin, Vineet R. Tiruvadi, Suk Won Hwang, Ann C. Vanleer, Drausin F. Wulsin, Kathryn Davis, Casey E. Gelber, Larry Palmer, Jan Van Der Spiegel, Jian Wu, Jianliang Xiao, Yonggang Huang, Diego Contreras, John A. Rogers, and Brian Litt. Flexible, foldable, actively multiplexed, high-density electrode array for mapping brain activity in vivo. *Nature Neuroscience*, 14(12):1599–1605, 2011.

[13] Rui Cheng, Shan Jiang, Yu Chen, Yuan Liu, Nathan Weiss, Hung Chieh Cheng, Hao Wu, Yu Huang, and Xiangfeng Duan. Few-layer molybdenum disulfide transistors and circuits for high-speed flexible electronics. *Nature Communications*, 5:1–9, 2014.

[14] Nathan Schaefer, Ramon Garcia-Cortadella, Andrea Bonaccini Calia, Nikolaos Mavredakis, Xavi Illa, Eduard Masvidal-Codina, Jose de la Cruz, Elena del Corro, Laura Rodríguez, Elisabet Prats-Alfonso, Jessica Bousquet, Javier Martínez-Aguilar, Antonio P. Pérez-Marín, Clement Hébert, Rosa Villa, David Jiménez, Anton Guimerà-Brunet, and Jose A. Garrido. Improved metal-graphene contacts for low-noise, high-density microtransistor arrays for neural sensing. *Carbon*, 161:647–655, 2020.

[15] Nathan Schaefer, Ramon Garcia-Cortadella, Javier Martínez-Aguilar, Gerrit Schwesig, Xavi Illa, Ana Moya Lara, Sara Santiago, Clement Hébert, Gonzalo Guirado, Rosa Villa, Anton Sirota, Anton Guimerà-Brunet, and Jose A Garrido. Multiplexed neural sensor array of graphene solution-gated field-effect transistors. *2D Materials*, 7(2):025046, 2020.

[16] Ramon Garcia-Cortadella, Nathan Schäfer, Jose Cisneros-Fernandez, Lucía Re, Xavi Illa, Gerrit Schwesig, Ana Moya, Sara Santiago, Gonzalo Guirado, Rosa Villa, Anton Sirota, Francesc Serra-Graells, Jose A. Garrido, and Antón Guimerà-Brunet. Switchless Multiplexing of Graphene Active Sensor Arrays for Brain Mapping. *Nano Letters*, pages 1–27, 2020.

[17] Jacques J. Vidal. Realtime Detection of Brain Events in EEG. *Proceedings of the IEEE*, 65(5):633–641, 1977.

[18] Stevo Bozinovski, Mihail Sestakov, and Liljana Bozinovska. Using EEG alpha rhythm to control a mobile robot. *IEEE/Engineering in Medicine and Biology Society Annual Conference*, 10 pt 3:1515–1516, 1988.

[19] Y. K. Song, D. A. Borton, S. Park, W. R. Patterson, C. W. Bull, F. Laiwalla, J. Mislow, J. D. Simeral, J. P. Donoghue, and A. V. Nurmikko. Active microelectronic neurosensor arrays for implantable brain communication interfaces. *IEEE Transactions on Neural Systems and Rehabilitation Engineering*, 17(4):339–345, 2009.

[20] Leigh R Hochberg, Daniel Bacher, Beata Jarosiewicz, Nicolas Y Masse, John D Simeral, and Joern Vogel. Reach and grasp by people with tetraplegia using a neurally controlled robotic arm. *Nature*, 2012.

[21] Gabriel A. Silva. A new frontier: The convergence of nanotechnology, brain machine interfaces, and artificial intelligence. *Frontiers in Neuroscience*, 12(NOV):1–8, 2018.

[22] Brian Lee, Daniel Kramer, Michelle Armenta Salas, Spencer Kellis, David Brown, Tatyana Dobreva, Christian Klaes, Christi Heck, Charles Liu, and Richard A. Andersen. Engineering artificial somatosensation through cortical stimulation in humans. *Frontiers in Systems Neuroscience*, 12(June):1–11, 2018.

[23] A. Bolu Ajiboye, Francis R. Willett, Daniel R. Young, William D. Memberg, Brian A. Murphy, Jonathan P. Miller, Benjamin L. Walter, Jennifer A. Sweet, Harry A. Hoyen, Michael W. Keith, P. Hunter Peckham, John D. Simeral, John P. Donoghue, Leigh R. Hochberg, and Robert F. Kirsch. Restoration of reaching and grasping movements through brain-controlled muscle stimulation in a person with tetraplegia: a proof-of-concept demonstration. *The Lancet*, 389(10081):1821–1830, 2017.

[24] Amy L. Orsborn and Bijan Pesaran. Parsing learning in networks using brain–machine interfaces. *Current Opinion in Neurobiology*, 46:76–83, 2017.

[25] Kelly B. Clancy, Aaron C. Koralek, Rui M. Costa, Daniel E. Feldman, and Jose M. Carmena. Volitional modulation of optically recorded calcium signals during neuroprosthetic learning. *Nature Neuroscience*, 17(6):807–809, 2014.

[26] Maryam M. Shanechi. Brain–machine interfaces from motor to mood. *Nature Neuroscience*, 22(10):1554–1564, 2019.

[27] Helen S Mayberg, Andres M Lozano, Valerie Voon, Heather E Mcneely, David Seminowicz, Clement Hamani, Jason M Schwalb, and Sidney H Kennedy. Deep Brain Stimulation for Treatment-Resistant Depression ing electrical stimulation of the subgenual cingulate. *Neuron*, 45:651–660, 2005.

[28] Paul E. Holtzheimer, Mustafa M. Husain, Sarah H. Lisanby, Stephan F. Taylor, Louis A. Whitworth, Shawn McClintock, Konstantin V. Slavin, Joshua

Berman, Guy M. McKhann, Parag G. Patil, Barry R. Rittberg, Aviva Abosch, Ananda K. Pandurangi, Kathryn L. Holloway, Raymond W. Lam, Christopher R. Honey, Joseph S. Neimat, Jaimie M. Henderson, Charles DeBattista, Anthony J. Rothschild, Julie G. Pilitsis, Randall T. Espinoza, Georgios Petrides, Alon Y. Mogilner, Keith Matthews, De Lea Peichel, Robert E. Gross, Clement Hamani, Andres M. Lozano, and Helen S. Mayberg. Subcallosal cingulate deep brain stimulation for treatment-resistant depression: a multisite, randomised, sham-controlled trial. *The Lancet Psychiatry*, 4(11):839–849, 2017.

[29] Gopala K. Anumanchipalli, Josh Chartier, and Edward F. Chang. Speech synthesis from neural decoding of spoken sentences. *Nature*, 568(7753):493–498, 2019.

[30] Karen A. Moxon and Guglielmo Foffani. Brain-machine interfaces beyond neuroprosthetics. *Neuron*, 86(1):55–67, 2015.

[31] Boris Rosin, Maya Slovik, Rea Mitelman, Michal Rivlin-etzion, Suzanne N Haber, Zvi Israel, and Eilon Vaadia. Article Closed-Loop Deep Brain Stimulation Is Superior in Ameliorating Parkinsonism. *Neuron*, 72(2):370–384, 2011.

[32] Antal Berényi, Belluscio Mariano, Mao Dun, and György Buzsáki. Closed-Loop Control of Epilepsy by Transcranial Electrical Stimulation. *Science*, 735, 2012.

[33] Hayriye Cagnan, David Pedrosa, Simon Little, Alek Pogosyan, Binith Cheeran, Tipu Aziz, Alexander Green, James Fitzgerald, Thomas Foltynie, Patricia Limousin, Ludvic Zrinzo, Marwan Hariz, Karl J Friston, Timothy Denison, and Peter Brown. Stimulating at the right time : phase-specific deep brain stimulation. *Brain - A journal of neurology*, 140(2016):132–145, 2017.

[34] Oliver Müller and Stefan Rotter. Neurotechnology : Current Developments and Ethical Issues. *Frontiers in Systems Neuroscience*, 11(December):1–5, 2017.

[35] Carolina G. Ferroni, Monica Maranesi, Alessandro Livi, Marco Lanzilotto, and Luca Bonini. Comparative performance of linear multielectrode probes and single-tip electrodes for intracortical microstimulation and single-neuron recording in macaque monkey. *Frontiers in Systems Neuroscience*, 11(November):1–8, 2017.

[36] Steven M. Wellman, Lehong Li, Yalikun Yaxiaer, Ingrid McNamara, and Takashi D.Y. Kozai. Revealing spatial and temporal patterns of cell death, glial proliferation, and blood-brain barrier dysfunction around implanted intracortical neural interfaces. *Frontiers in Neuroscience*, 13(MAY):1–17, 2019.

[37] A. Zátonyi, G. Orbán, R. Modi, G. Márton, D. Meszéna, I. Ulbert, A. Pongrácz, M. Ecker, W. E. Voit, A. Joshi-Imre, and Z. Fekete. A softening laminar electrode for recording single unit activity from the rat hippocampus. *Scientific Reports*, 9(1):1–13, 2019.

[38] Steven M. Wellman, James R. Eles, Kip A. Ludwig, John P. Seymour, Nicholas J. Michelson, William E. McFadden, Alberto L. Vazquez, and Takashi D.Y. Kozai. A Materials Roadmap to Functional Neural Interface Design. *Advanced Functional Materials*, 28(12):1–38, 2018.

[39] Abraham Kuruvilla and Roland Flink. Intraoperative electrocorticography in epilepsy surgery : useful or not ? *Seizure*, 1311(03):577–584, 2003.

[40] Gerwin Schalk, Christoph Kapeller, Christoph Guger, Hiroshi Ogawa, Satoru Hiroshima, and Rosa Lafer-sousa. Facephenes and rainbows : Causal evidence for functional and anatomical specificity of face and color processing in the human brain. *Proceedings of the National Academy of Sciences*, 114(46):12285–12290, 2017.

[41] Robert T Knight and Ming Hsu. HHS Public Access. *Current Biology*, 28(18):2889–2899, 2019.

[42] Stephanie Martin, Iñaki Iturrate, José R Millán, Robert T Knight, and Brian N Pasley. Decoding Inner Speech Using Electrocorticography : Progress and Challenges Toward a Speech Prosthesis. *Frontiers in Neuroscience*, 12(June):1–10, 2018.

[43] David Poeppel, Karen Emmorey, Gregory Hickok, and Liina Pylkkänen. Towards a new neurobiology of language. *Journal of Neuroscience*, 32(41):14125–14131, 2012.

[44] Xiaoqian J. Chai, Jonathan A. Berken, Elise B. Barbeau, Jennika Soles, Megan Callahan, Jen Kai Chen, and Denise Klein. Intrinsic functional connectivity in the adult brain and success in second-language learning. *Journal of Neuroscience*, 36(3):755–761, 2016.

[45] Antonio Benítez-Burraco and Elliot Murphy. Why Brain Oscillations Are Improving Our Understanding of Language. *Frontiers in Behavioral Neuroscience*, 13(August):1–10, 2019.

[46] Elliot Murphy. A pragmatic oscillome: Aligning visual attentional mechanisms with language comprehension. *Frontiers in Systems Neuroscience*, 10(AUG):1–3, 2016.

[47] Dion Khodagholy, Jennifer N Gelinas, Thomas Thesen, Werner Doyle, Orrin Devinsky, George G Malliaras, and György Buzsáki. t e c h n i c a l r e p o r t s NeuroGrid : recording action potentials from the surface of the brain. *Nature Neuroscience*, 18(2):310–316, 2015.

[48] James J. Jun, Nicholas A. Steinmetz, Joshua H. Siegle, Daniel J. Denman, Marius Bauza, Brian Barbarits, Albert K. Lee, Costas A. Anastassiou, Alexandru Andrei, Çağatay Aydin, Mladen Barbic, Timothy J. Blanche, Vincent Bonin, João Couto, Barundeb Dutta, Sergey L. Gratiy, Diego A. Gutnisky, Michael Häusser, Bill Karsh, Peter Ledochowitsch, Carolina Mora Lopez, Catalin Mitelut, Silke Musa, Michael Okun, Marius Pachitariu, Jan Putzeys, P. Dylan Rich, Cyrille Rossant, Wei Lung Sun, Karel Svoboda, Matteo Carandini, Kenneth D. Harris, Christof Koch, John O'Keefe, and Timothy D. Harris. Fully integrated silicon probes for high-density recording of neural activity. *Nature*, 551(7679):232–236, 2017.

[49] Jason E. Chung, Hannah R. Joo, Jiang Lan Fan, Daniel F. Liu, Alex H. Barnett, Supin Chen, Charlotte Geaghan-Breiner, Mattias P. Karlsson, Magnus Karlsson, Kye Y. Lee, Hexin Liang, Jeremy F. Magland, Jeanine A. Pebbles, Angela C. Tooker, Leslie F. Greengard, Vanessa M. Tolosa, and Loren M. Frank. High-Density, Long-Lasting, and Multi-region Electrophysiological Recordings Using Polymer Electrode Arrays. *Neuron*, 101(1):21–31.e5, 2019.

[50] Elon Musk. An integrated brain-machine interface platform with thousands of channels. *bioRxiv*, -(-):0–11, 2019.

[51] Stefan Eick, Jens Wallys, Boris Hofmann, André Van Ooyen, Uwe Schnakenberg, Sven Ingebrandt, and David J Anderson. Iridium oxide microelectrode arrays for in vitro stimulation of individual rat neurons from dissociated cultures. *Frontiers in Neuroengineering*, 2(November):1–12, 2009.

[52] Sharanya Arcot Desai, John D Rolston, Liang Guo, and Steve M Potter. Improving impedance of implantable microwire multi- electrode arrays by ultrasonic electroplating of durable platinum black. *frontiers in neuroengineering*, 3(May):1–11, 2010.

[53] Marie Engelene J Obien, Kosmas Deligkaris, Torsten Bullmann, and Douglas J Bakkum. Revealing neuronal function through microelectrode array recordings. *Frontiers in Neuroscience*, 8(January):1–30, 2015.

[54] Lulu Zhou, Henry Jay, Yi Ge, and Joseph Lunec. Toxicology in Vitro Multiwalled carbon nanotubes : A cytotoxicity study in relation to functionalization , dose and dispersion. *Toxicology in Vitro*, 42(February):292–298, 2017.

[55] Jean-paul Mazellier, Lionel Rousseau, Emmanuel Scorsone, Myline Cottance, Gaelle Lissorgues, Marc O Heuschkel, Serge Picaud, Philippe Bergonzo, and Blaise Yvert. Biomaterials 3D-nanostructured boron-doped diamond for microelectrode array neural interfacing ment H e Ga e. *Biomaterials*, 53:173–183, 2015.

[56] Lucas H. Hess, Michael Jansen, Vanessa Maybeck, Moritz V. Hauf, Max Seifert, Martin Stutzmann, Ian D. Sharp, Andreas Offenhäusser, and Jose A. Garrido. Graphene transistor arrays for recording action potentials from electrogenic cells. *Advanced Materials*, 23(43):5045–5049, 2011.

[57] Maurizio Gulino, Donghoon Kim, Salvador Pané, Sofia Duque Santos, and Ana Paula Pêgo. Tissue response to neural implants: The use of model systems toward new design solutions of implantable microelectrodes. *Frontiers in Neuroscience*, 13(JUL):1–24, 2019.

[58] Martin Lauritzen, Jens Peter Dreier, Martin Fabricius, Jed A Hartings, Rudolf Graf, and Anthony John Strong. Clinical relevance of cortical spreading depression in neurological disorders : migraine , malignant stroke , subarachnoid and intracranial hemorrhage , and traumatic brain injury. *Journal of Cerebral Blood Flow & Metabolism*, pages 17–35, 2011.

[59] Martin Fabricius, Susanne Fuhr, Lisette Willumsen, Jens P Dreier, Robin Bhatia, Martyn G Boutelle, Jed A Hartings, Ross Bullock, and Anthony J Strong. NIH Public Access. *Clinical Neurophysiology*, 119(9):1973–1984, 2009.

[60] Eduard Masvidal-Codina, Xavi Illa, Miguel Dasilva, Andrea Bonaccini Calia, Tanja Dragojević, Ernesto E. Vidal-Rosas, Elisabet Prats-Alfonso, Javier Martínez-Aguilar, Jose M. De la Cruz, Ramon Garcia-Cortadella, Philippe Godignon, Gemma Rius, Alessandra Camassa, Elena Del Corro, Jessica Bousquet, Clement Hébert, Turgut Durduran, Rosa Villa, Maria V. Sanchez-Vives, Jose A. Garrido, and Anton Guimerà-Brunet. High-resolution mapping of infraslow cortical brain activity enabled by graphene microtransistors. *Nature Materials*, 18(3):280–288, 2019.

[61] Bogdan C. Raducanu, Refet F. Yazicioglu, Carolina M. Lopez, Marco Ballini, Jan Putzeys, Shiwei Wang, Alexandru Andrei, Marleen Welkenhuysen, Nick Van Helleputte, Silke Musa, Robert Puers, Fabian Kloosterman, Chris Van Hoof, and Srinjoy Mitra. Time multiplexed active neural probe with 678 parallel recording sites. *European Solid-State Device Research Conference*, 2016-Octob:385–388, 2016.

[62] Gian Nicola Angotzi, Fabio Boi, Aziliz Lecomte, Ermanno Miele, Mario Malerba, Stefano Zucca, Antonino Casile, and Luca Berdondini. SiNAPS: An implantable active pixel sensor CMOS-probe for simultaneous large-scale neural recordings. *Biosensors and Bioelectronics*, 126(September 2018):355–364, 2019.

[63] M. A. Escabi, H. L. Read, J. Viventi, D.-H. Kim, N. C. Higgins, D. A. Storace, A. S. K. Liu, A. M. Gifford, J. F. Burke, M. Campisi, Y.-S. Kim, A. E. Avrin, V. d. Spiegel Jan, Y. Huang, M. Li, J. Wu, J. A. Rogers, B. Litt, and Y. E. Cohen. A high-density, high-channel count, multiplexed ECoG array for auditory-cortex recordings. *Journal of Neurophysiology*, 112(6):1566–1583, 2014.

[64] Chia-Han Chiang, Sang Min Won, Amy L. Orsborn, Ki Jun Yu, Michael Trumpis, Brinnae Bent, Charles Wang, Yeguang Xue, Seunghwan Min, Virginia Woods, Chunxiu Yu, Bong Hoon Kim, Sung Bong Kim, Rizwan Huq, Jinghua Li, Kyung Jin Seo, Flavia Vitale, Andrew Richardson, Hui Fang,

Yonggang Huang, Kenneth Shepard, Bijan Pesaran, John A. Rogers, and Jonathan Viventi. Development of a neural interface for high-definition, long-term recording in rodents and nonhuman primates. *Science Translational Medicine*, 12(538):eaay4682, 2020.

[65] Wonryung Lee, Dongmin Kim, Jonathan Rivnay, Naoji Matsuhisa, Thomas Lonjaret, Tomoyuki Yokota, Hiromu Yawo, Masaki Sekino, George G. Malliaras, and Takao Someya. Integration of Organic Electrochemical and Field-Effect Transistors for Ultraflexible, High Temporal Resolution Electrophysiology Arrays. *Advanced Materials*, 28(44):9722–9728, 2016.

[66] Wonryung Lee, Dongmin Kim, Naoji Matsuhisa, Masae Nagase, Masaki Sekino, George G. Malliaras, Tomoyuki Yokota, and Takao Someya. Transparent, conformable, active multielectrode array using organic electrochemical transistors. *Proceedings of the National Academy of Sciences*, 114(40):201703886, 2017.

[67] F. Bonaccorso, Z. Sun, T. Hasan, and A. C. Ferrari. Graphene photonics and optoelectronics. *Nature Photonics*, 4(9):611–622, 2010.

[68] Cyrill Bussy, Dhifaf Jasim, Neus Lozano, Daniel Terry, and Kostas Kostarelos. The current graphene safety landscape-a literature mining exercise. *Nanoscale*, 7(15):6432–6435, 2015.

[69] Tapas Kuila, Saswata Bose, Ananta Kumar Mishra, Partha Khanra, Nam Hoon Kim, and Joong Hee Lee. Chemical functionalization of graphene and its applications. *Progress in Materials Science*, 57(7):1061–1105, 2012.

[70] Yuan Huang, Eli Sutter, Norman N. Shi, Jiabao Zheng, Tianzhong Yang, Dirk Englund, Hong Jun Gao, and Peter Sutter. Reliable Exfoliation of Large-Area High-Quality Flakes of Graphene and Other Two-Dimensional Materials. *ACS Nano*, 9(11):10612–10620, 2015.

[71] Xuesong Li, Weiwei Cai, Jinho An, Seyoung Kim, Junghyo Nah, Dongxing Yang, Richard Piner, Aruna Velamakanni, Inhwa Jung, Emanuel Tutuc, Sanjay K. Banerjee, Luigi Colombo, and Rodney S. Ruoff. Large-area synthesis of high-quality and uniform graphene films on copper foils. *Science*, 324(5932):1312–1314, 2009.

[72] C. V. RAMAN and K. S. KRISHNAN. © 1928 Nature Publishing Group. *Nature*, 1928.

[73] Andrea C. Ferrari and Denis M. Basko. Raman spectroscopy as a versatile tool for studying the properties of graphene. *Nature Nanotechnology*, 8(4):235–246, 2013.

[74] S Gayathri, P Jayabal, M Kottaisamy, and V Ramakrishnan. Synthesis of few layer graphene by direct exfoliation of graphite and a Raman spectroscopic study. *AIP Advances*, 027116(January), 2014.

[75] Axel Eckmann, Alexandre Felten, Artem Mishchenko, Liam Britnell, Ralph Krupke, Kostya S. Novoselov, and Cinzia Casiraghi. Probing the nature of defects in graphene by Raman spectroscopy. *Nano Letters*, 12(8):3925–3930, 2012.

[76] Changgu Lee, Xiaoding Wei, Jeffrey W Kysar, and James Hone. of Monolayer Graphene. *Science*, 321(July):385–388, 2008.

[77] P R Wallace. The Band Theory of Graphite. *Physical Review*, 71(9):622–634, 1947.

[78] R. S. Shishir, D. K. Ferry, and S. M. Goodnick. Intrinsic mobility limit in graphene at room temperature. *2009 9th IEEE Conference on Nanotechnology, IEEE NANO 2009*, 8:21–24, 2009.

[79] Jian Hao Chen, Chaun Jang, Shudong Xiao, Masa Ishigami, and Michael S. Fuhrer. Intrinsic and extrinsic performance limits of graphene devices on SiO 2. *Nature Nanotechnology*, 3(4):206–209, 2008.

[80] A. K.M. Newaz, Yevgeniy S. Puzyrev, Bin Wang, Sokrates T. Pantelides, and Kirill I. Bolotin. Probing charge scattering mechanisms in suspended graphene by varying its dielectric environment. *Nature Communications*, 3:734–736, 2012.

[81] Deep Jariwala, Vinod K. Sangwan, Lincoln J. Lauhon, Tobin J. Marks, and Mark C. Hersam. Emerging device applications for semiconducting two-dimensional transition metal dichalcogenides. *ACS Nano*, 8(2):1102–1120, 2014.

[82] Qing Hua Wang, Kourosh Kalantar-zadeh, Andras Kis, Jonathan N Coleman, and Michael S Strano. transition metal dichalcogenides. *Nature Nanotechnology*, 7(November):699–712, 2012.

[83] Youngki Yoon, Kartik Ganapathi, and Sayeef Salahuddin. How good can monolayer MoS2 transistors be? *Nano Letters*, 11(9):3768–3773, 2011.

[84] Yi-hsien Lee, Xin-quan Zhang, Wenjing Zhang, Mu-tung Chang, Cheng-te Lin, Kai-di Chang, Ya-chu Yu, Jacob Tse-wei Wang, Chia-seng Chang, Lain-jong Li, and Tsung-wu Lin. Synthesis of Large-Area MoS 2 Atomic Layers with Chemical Vapor Deposition. *Advanced Materials*, 24:2320–2325, 2012.

[85] Arend M Van Der Zande, Pinshane Y Huang, Daniel A Chenet, Timothy C Berkelbach, Yumeng You, Gwan-hyoung Lee, Tony F Heinz, David R Reichman, David A Muller, and James C Hone. monolayer molybdenum disulphide. *Nature Materials*, 12(6):554–561, 2013.

[86] Nicola Marzari, Oriol Lopez Sanchez, Yen-cheng Kung, Daria Krasnozhon, Ming-wei Chen, Simone Bertolazzi, Philippe Gillet, Anna Fontcuberta, Aleksandra Radenovic, and Andras Kis. Large-Area Epitaxial Monolayer MoS 2. *ACS Nano*, 9(4):4611–4620, 2015.

[87] High-quality Monolayer Mos. Oxygen-Assisted Chemical Vapor Deposition Growth of Large Single-. *Journal of the american chemical society*, pages 8–11, 2015.

[88] Shisheng Li, Yung-chang Lin, Wen Zhao, Jing Wu, Zhuo Wang, Zehua Hu, Youde Shen, Dai-ming Tang, Junyong Wang, Qi Zhang, Hai Zhu, Leiqiang Chu, Weijie Zhao, Chang Liu, Zhipei Sun, Takaaki Taniguchi, Minoru Osada, Wei Chen, and Qing-hua Xu. Vapour–liquid–solid growth of monolayer MoS2 nanoribbons. *Nature Materials*, 17(June), 2018.

[89] V Kranthi Kumar, Sukanya Dhar, Tanushree H Choudhury, S A Shivashankar, and Srinivasan Raghavan. of TMDs : the case of MoS 2 †. *Nanoscale*, pages 7802–7810, 2015.

[90] Kibum Kang, Saien Xie, Lujie Huang, Yimo Han, Pinshane Y Huang, Kin Fai Mak, Cheol-joo Kim, and David Muller. High-mobility three-atom-thick semiconducting films with wafer-scale homogeneity. *Nature*, pages 3–7, 2015.

[91] Huanyao Cun, Michal Macha, Hokwon Kim, Ke Liu, Yanfei Zhao, Thomas Lagrange, Andras Kis, and Aleksandra Radenovic. Wafer-scale MOCVD growth of monolayer MoS 2 on sapphire and SiO 2. *Nano Research*, 12(10):2646–2652, 2019.

[92] Stefan Wachter, Dmitry K. Polyushkin, Ole Bethge, and Thomas Mueller. A microprocessor based on a two-dimensional semiconductor. *Nature Communications*, 8:1–6, 2017.

[93] Changgu Lee, Hugen Yan, Louis E. Brus, Tony F. Heinz, James Hone, and Sunmin Ryu. Anomalous lattice vibrations of single- and few-layer MoS2. *ACS Nano*, 4(5):2695–2700, 2010.

[94] Peng Luo, Fuwei Zhuge, Qingfu Zhang, Yuqian Chen, Liang Lv, Yu Huang, Huiqiao Li, and Tianyou Zhai. Doping engineering and functionalization of two-dimensional metal chalcogenides. *Nanoscale Horizons*, 4(1):26–51, 2019.

[95] Dattatray J. Late, Bin Liu, H. S.S.Ramakrishna Matte, Vinayak P. Dravid, and C. N.R. Rao. Hysteresis in single-layer MoS 2 field effect transistors. *ACS Nano*, 6(6):5635–5641, 2012.

[96] Jiyue Zou, Lisheng Wang, and Fengxiang Chen. Improved performance of top-gated multilayer MoS2 transistors with channel fully encapsulated by Al2O3 dielectric. *AIP Advances*, 9(9), 2019.

[97] Nengjie Huo, Yujue Yang, Yu Ning Wu, Xiao Guang Zhang, Sokrates T. Pantelides, and Gerasimos Konstantatos. High carrier mobility in monolayer CVD-grown MoS2 through phonon suppression. *Nanoscale*, 10(31):15071–15077, 2018.

[98] Filippo Giubileo and Antonio Di Bartolomeo. The role of contact resistance in graphene field-effect devices. *Progress in Surface Science*, 92(3):143–175, 2017.

[99] Yuanbo Zhang, Victor W. Brar, Caglar Girit, Alex Zettl, and Michael F. Crommie. Origin of spatial charge inhomogeneity in graphene. *Nature Physics*, 5(10):722–726, 2009.

[100] Alexander A. Balandin. Low-frequency 1/f noise in graphene devices. *Nature Nanotechnology*, 8(8):549–555, 2013.

[101] Markus Dankerl, Moritz V. Hauf, Andreas Lippert, Lucas H. Hess, Stefan Birner, Ian D. Sharp, Ather Mahmood, Pierre Mallet, Jean Yves Veuillen, Martin Stutzmann, and Jose A. Garrido. Graphene solution-gated field-effect transistor array for sensing applications. *Advanced Functional Materials*, 20(18):3117–3124, 2010.

[102] Xuesong Li, Weiwei Cai, Jinho An, Seyoung Kim, Junghyo Nah, Dongxing Yang, Richard Piner, Aruna Velamakanni, Inhwa Jung, Emanuel Tutuc, Sanjay K. Banerjee, Luigi Colombo, and Rodney S. Ruoff. Large-area synthesis of high-quality and uniform graphene films on copper foils. *Science*, 324(5932):1312–1314, 2009.

[103] L. H. Hess, M. V. Hauf, M. Seifert, F. Speck, T. Seyller, M. Stutzmann, I. D. Sharp, and J. A. Garrido. High-transconductance graphene solution-gated field effect transistors. *Applied Physics Letters*, 99(3):2009–2012, 2011.

[104] S. Christensson, I. Lundström, and C. Svensson. Low frequency noise in MOS transistors-I Theory. *Solid State Electronics*, 11(9):797–812, 1968.

[105] F. N. Hooge. 1/F Noise. *Physica B+C*, 83(1):14–23, 1976.

[106] Guanxiong Liu, Sergey Rumyantsev, Michael S. Shur, and Alexander A. Balandin. Origin of 1/f noise in graphene multilayers: Surface vs. volume. *Applied Physics Letters*, 102(9), 2013.

[107] Paritosh Karnatak, T Phanindra Sai, Srijit Goswami, Subhamoy Ghatak, and Sanjeev Kaushal. Current crowding mediated large contact noise in graphene field-effect transistors. *Nature Communications*, 7:1–8, 2016.

[108] Atindra Nath Pal and Arindam Ghosh. Ultralow noise field-effect transistor from multilayer graphene. *Applied Physics Letters*, 95(8), 2009.

[109] Tymoteusz Ciuk, Oleg Petruk, Andrzej Kowalik, Iwona Jozwik, Andrzej Rychter, Jan Szmidt, and Wlodzimierz Strupinski. Low-noise epitaxial graphene on SiC Hall effect element for commercial applications. *Applied Physics Letters*, 108(22):1–6, 2016.

[110] Sohail Chatoor, Iddo Heller, Jeroen B. Oostinga, Alberto F. Morpurgo, Serge G. Lemay, Cees Dekker, Jaan Männik, and Marcel A. G. Zevenbergen. Charge Noise in Graphene Transistors. *Nano Letters*, 10(5):1563–1567, 2010.

[111] Nikolaos Mavredakis, Ramon Garcia Cortadella, Andrea Bonaccini Calia, Jose A. Garrido, and David Jiménez. Understanding the bias dependence of low frequency noise in single layer graphene FETs. *Nanoscale*, 10(31):14947–14956, 2018.

[112] S Rumyantsev, G Liu, W Stillman, and M Shur. Electrical and noise characteristics of graphene field-effect transistors : ambient effects , noise sources and physical. *Journal of Physics: Condensed Matter*, 395302, 2010.

[113] Seung Min Song, Jong Kyung Park, One Jae Sul, and Byung Jin Cho. Determination of work function of graphene under a metal electrode and its role in contact resistance. *Nano Letters*, 12(8):3887–3892, 2012.

[114] Adrien Allain, Jiahao Kang, Kaustav Banerjee, and Andras Kis. Electrical contacts to two-dimensional semiconductors, nov 2015.

[115] Xiangyu Yan, Kunpeng Jia, Yajuan Su, Yuanjun Ma, Jun Luo, Huilong Zhu, and Yayi Wei. Edge-Contact Formed by Oxygen Plasma and Rapid Thermal Annealing to Improve Metal-Graphene Contact Resistance. *ECS Journal of Solid State Science and Technology*, 7(2):M11–M15, 2018.

[116] Li Wei, Yiran Liang, Dangmin Yu, Lianmao Peng, Kurt P. Pernstich, Tian Shen, A. R. Hight Walker, Guangjun Cheng, Christina A. Hacker, Curt A. Richter, Qiliang Li, David J. Gundlach, and Xuelei Liang. Ultraviolet/ozone treatment to reduce metal-graphene contact resistance. *Applied Physics Letters*, 102(18), 2013.

[117] Eiichiro Watanabe, Arolyn Conwill, Daiju Tsuya, and Yasuo Koide. Low contact resistance metals for graphene based devices. *Diamond and Related Materials*, 24:171–174, 2012.

[118] Wei Sun Leong, Chang Tai Nai, and John T.L. Thong. What does annealing do to metal-graphene contacts? *Nano Letters*, 14(7):3840–3847, 2014.

[119] A. Gahoi, V. Passi, S. Kataria, S. Wagner, A. Bablich, and M.C. Lemme. Systematic comparison of metal contacts on CVD graphene. In *2015 45th European Solid State Device Research Conference (ESSDERC)*, pages 184–187. IEEE, sep 2015.

[120] Wei Li, Christina A. Hacker, Guangjun Cheng, Yiran Liang, Boyuan Tian, A. R. Hight Walker, Curt A. Richter, David J. Gundlach, Xuelei Liang, and Lianmao Peng. Highly reproducible and reliable metal/graphene contact by ultraviolet-ozone treatment. *Journal of Applied Physics*, 115(11), 2014.

[121] Zengguang Cheng, Qiang Li, Zhongjun Li, Qiaoyu Zhou, and Ying Fang. Suspended graphene sensors with improved signal and reduced noise. *Nano Letters*, 10(5):1864–1868, 2010.

[122] Nicholas Petrone, Tarun Chari, Inanc Meric, Lei Wang, Kenneth L. Shepard, and James Hone. Flexible Graphene Field-Effect Transistors Encapsulated in Hexagonal Boron Nitride. *ACS Nano*, 9(9):8953–8959, 2015.

[123] Myrsini Lafkioti, Benjamin Krauss, Timm Lohmann, Ute Zschieschang, Hagen Klauk, Klaus V. Klitzing, and Jurgen H. Smet. Graphene on a hydrophobic substrate: Doping reduction and hysteresis suppression under ambient conditions. *Nano Letters*, 10(4):1149–1153, 2010.

[124] Wi Hyoung Lee, Jaesung Park, Youngsoo Kim, Kwang S. Kim, Byung Hee Hong, and Kilwon Cho. Control of graphene field-effect transistors by interfacial hydrophobic self-assembled monolayers. *Advanced Materials*, 23(30):3460–3464, 2011.

[125] Sk Fahad Chowdhury, Sushant Sonde, Somayyeh Rahimi, Li Tao, Sanjay Banerjee, and Deji Akinwande. Improvement of graphene field-effect transistors by hexamethyldisilazane surface treatment. *Applied Physics Letters*, 105(3), 2014.

[126] Dae Yool Jung, Sang Yoon Yang, Hamin Park, Woo Cheol Shin, Joong Gun Oh, and Byung Jin Cho. Interface engineering for high performance graphene electronic devices. *Nano Convergence*, 2015.

[127] Himadri Pandey, Mehrdad Shaygan, Simon Sawallich, Satender Kataria, Zhenxing Wang, Achim Noculak, Martin Otto, Michael Nagel, Renato Negra, Daniel Neumaier, and Max C. Lemme. All CVD Boron Nitride Encapsulated Graphene FETs with CMOS Compatible Metal Edge Contacts. *IEEE Transactions on Electron Devices*, 65(10):4129–4134, 2018.

[128] Morteza Kayyalha and Yong P. Chen. Observation of reduced 1/f noise in graphene field effect transistors on boron nitride substrates. *Applied Physics Letters*, 107(11):10–14, 2015.

[129] A. M.K. Dagamseh, R. J. Wiegerink, T. S.J. Lammerink, and G. J.M. Krijnen. Towards a high-resolution flow camera using artificial hair sensor arrays for flow pattern observations. *Bioinspiration and Biomimetics*, 7(4), 2012.

[130] B Eversmann, M Jenkner, F Hofmann, C Paulus, R Brederlow, B Holzapfl, P Fromherz, M Merz, M Brenner, M Schreiter, R Gabl, K Plehnert, M Steinhauser, G Eckstein, D Schmitt-Landsiedel, and R Thewes. A 128 x 128 CMOS Biosensor Array for Extracellular\rRecording of Neural Activity. *Ieee Journal of Solid-State Circuits,*, 38(12):2306–2317, 2003.

[131] Ramon Garcia-Cortadella, Eduard Masvidal-Codina, Jose M. De la Cruz, Nathan Schäfer, Gerrit Schwesig, Christoph Jeschke, Javier Martinez-Aguilar,

Maria V. Sanchez-Vives, Rosa Villa, Xavi Illa, Anton Sirota, Anton Guimerà, and Jose A. Garrido. Distortion-Free Sensing of Neural Activity Using Graphene Transistors. *Small*, 16(16):1–10, 2020.

[132] G Kim, C. Cao, K. Gharibdoust, A. Tajalli, and Y. Leblebici. A Time-Division Multiplexing Signaling Scheme for Inter-Symbol/Channel Interference Reduction in Low-Power Multi-Drop Memory Links. *IEEE Transactions on Circuits and Systems II: Express Briefs*, 64(12):1387–1391, 2017.

[133] Simon Drieschner, Anton Guimerà, Ramon G. Cortadella, Damià Viana, Evangelos Makrygiannis, Benno M. Blaschke, Josua Vieten, and Jose A. Garrido. Frequency response of electrolyte-gated graphene electrodes and transistors. *Journal of Physics D: Applied Physics*, 50(9), 2017.

[134] Marcelo S. Alencar and C. da Rocha Jr. Valdemar. *Communication Systems*. Springer US, 2005.

[135] D. C. Lee. Analysis of jitter in phase-locked loops. *IEEE Transactions on Circuits and Systems II: Analog and Digital Signal Processing*, 49(11):704–711, 2002.

[136] György Buzsáki, Costas A. Anastassiou, and Christof Koch. The origin of extracellular fields and currents-EEG, ECoG, LFP and spikes. *Nature Reviews Neuroscience*, 13(6):407–420, 2012.

[137] Bijan Pesaran, Martin Vinck, Gaute T. Einevoll, Anton Sirota, Pascal Fries, Markus Siegel, Wilson Truccolo, Charles E. Schroeder, and Ramesh Srinivasan. Investigating large-scale brain dynamics using field potential recordings: Analysis and interpretation. *Nature Neuroscience*, 21(7):903–919, 2018.

[138] Steffen Katzner, Ian Nauhaus, Andrea Benucci, Vincent Bonin, Dario L. Ringach, and Matteo Carandini. Local Origin of Field Potentials in Visual Cortex. *Neuron*, 61(1):35–41, 2009.

[139] Georgios Michalareas, Julien Vezoli, Stan van Pelt, Jan Mathijs Schoffelen, Henry Kennedy, and Pascal Fries. Alpha-Beta and Gamma Rhythms Subserve Feedback and Feedforward Influences among Human Visual Cortical Areas. *Neuron*, 89(2):384–397, 2016.

[140] Olga Cozzolino, Maria Marchese, Francesco Trovato, Enrico Pracucci, Gian Michele Ratto, Maria Gabriella Buzzi, Federico Sicca, and Filippo M. Santorelli. Understanding spreading depression from headache to sudden unexpected death. *Frontiers in Neurology*, 9(FEB):1–13, 2018.

[141] P Sawant-Pokam, P Suryavanshi, J M Mendez, F E Dudek, and K C Brennan. Mechanisms of Neuronal Silencing After Cortical Spreading Depression. *Cerebral Cortex*, pages 1–15, 2016.

[142] Anish Mitra, Andrew Kraft, Patrick Wright, Benjamin Acland, Abraham Z. Snyder, Zachary Rosenthal, Leah Czerniewski, Adam Bauer, Lawrence Snyder, Joseph Culver, Jin Moo Lee, and Marcus E. Raichle. Spontaneous Infra-slow Brain Activity Has Unique Spatiotemporal Dynamics and Laminar Structure. *Neuron*, 98(2):297–305.e6, 2018.

[143] Jonathan Posner, James A. Russell, and Bradley S. Peterson. Infraslow LFP correlates to resting-state fMRI BOLD signals. *Bone*, 23(1):1–7, 2008.

[144] Anish Mitra, Abraham Z Snyder, Enzo Tagliazucchi, Helmut Laufs, and St Louis. Propagated infra-slow intrinsic brain activity reorganizes across wake and slow wave sleep. *elife*, pages 1–19, 2015.

[145] Tuija Hiltunen, Jussi Kantola, Ahmed Abou Elseoud, Pasi Lepola, Kalervo Suominen, Tuomo Starck, Juha Nikkinen, Jukka Remes, Osmo Tervonen, Satu Palva, Vesa Kiviniemi, and J. Matias Palva. Infra-slow EEG fluctuations are correlated with resting-state network dynamics in fMRI. *Journal of Neuroscience*, 34(2):356–362, 2014.

[146] Joshua K. Grooms, Garth J. Thompson, Wen Ju Pan, Jacob Billings, Eric H. Schumacher, Charles M. Epstein, and Shella D. Keilholz. Infraslow Electroencephalographic and Dynamic Resting State Network Activity. *Brain Connectivity*, 7(5):265–280, 2017.

[147] A. M. Clare Kelly, Lucina Q. Uddin, Bharat B. Biswal, F. Xavier Castellanos, and Michael P. Milham. Competition between functional brain networks mediates behavioral variability. *NeuroImage*, 39(1):527–537, 2008.

[148] S. Vanhatalo, J. M. Palva, M. D. Holmes, J. W. Miller, J. Voipio, and K. Kaila. Infraslow oscillations modulate excitability and interictal epileptic activity in the human cortex during sleep. *Proceedings of the National Academy of Sciences of the United States of America*, 101(14):5053–5057, 2004.

[149] Giri P. Krishnan, Oscar C. González, and Maxim Bazhenov. Origin of slow spontaneous resting-state neuronal fluctuations in brain networks. *Proceedings of the National Academy of Sciences of the United States of America*, 115(26):6858–6863, 2018.

[150] Richard J. Radek, Peter Curzon, and Michael W. Decker. Characterization of high voltage spindles and spatial memory in young, mature and aged rats. *Brain Research Bulletin*, 33(2):183–188, 1994.

[151] Deji Akinwande, Nicholas Petrone, and James Hone. Two-dimensional flexible nanoelectronics. *Nature Communications*, 5, 2014.

[152] Wei Wu, Debtanu De, Su Chi Chang, Yanan Wang, Haibing Peng, Jiming Bao, and Shin Shem Pei. High mobility and high on/off ratio field-effect transistors based on chemical vapor deposited single-crystal MoS2 grains. *Applied Physics Letters*, 102(14), 2013.

[153] Pavel Bolshakov, Peng Zhao, Angelica Azcatl, Paul K. Hurley, Robert M. Wallace, and Chadwin D. Young. Electrical characterization of top-gated molybdenum disulfide field-effect-transistors with high-k dielectrics. *Microelectronic Engineering*, 178:190–193, 2017.

[154] Lanxia Cheng, Xiaoye Qin, Antonio T. Lucero, Angelica Azcatl, Jie Huang, Robert M. Wallace, Kyeongjae Cho, and Jiyoung Kim. Atomic layer deposition of a high-k dielectric on MoS2 using trimethylaluminum and ozone. *ACS Applied Materials and Interfaces*, 6(15):11834–11838, 2014.

[155] Igor Popov, Gotthard Seifert, and David Tománek. Designing electrical contacts to MoS2Monolayers: A computational study. *Physical Review Letters*, 108(15):1–5, 2012.

[156] Yan Wang, Jong Chan Kim, Ryan J Wu, Jenny Martinez, Xiuju Song, Jieun Yang, Fang Zhao, Andre Mkhoyan, Hu Young Jeong, and Manish Chhowalla. metals and two-dimensional semiconductors. *Nature*, 568:70–74, 2019.

[157] Graphene Electrodes. Low Resistance Metal Contacts to MoS 2 Devices with Nickel-Etched-. *ACS Nano*, 9(1):869–877, 2014.

[158] Dumitru Dumcenco, Dmitry Ovchinnikov, Kolyo Marinov, Predrag Lazić, Marco Gibertini, Nicola Marzari, Oriol Lopez Sanchez, Yen Cheng Kung, Daria Krasnozhon, Ming Wei Chen, Simone Bertolazzi, Philippe Gillet, Anna Fontcuberta I Morral, Aleksandra Radenovic, and Andras Kis. Large-area epitaxial monolayer moS$_2$. *ACS Nano*, 9(4):4611–4620, 2015.